REPORT DOCUMENTATION PAGE

AFRL-SR-BL-TR-01-

0507

1. REPORT DATE (DD-MM-YYYY)	2. REPORT TYPE	3. DATES COVERED (From - To)
08/24/2001	Final Technical Report	07/01/1997 – 12/31/2000

4. TITLE AND SUBTITLE
Control of Transition in Swept-Wing Boundary Layers using MEMS Devices as Distributed Roughness

5a. CONTRACT NUMBER

5b. GRANT NUMBER
F49620-97-1-0520

5c. PROGRAM ELEMENT NUMBER

6. AUTHOR(S)
William S. Saric

5d. PROJECT NUMBER

5e. TASK NUMBER

5f. WORK UNIT NUMBER

7. PERFORMING ORGANIZATION NAME(S) AND ADDRESS(ES)
Arizona Board of Regents for Arizona State University
Office of Research & Sponsored
Projects Administration
Box 873503
Tempe, AZ 85287-3503

8. PERFORMING ORGANIZATION REPORT NUMBER
XAA0034F

9. SPONSORING / MONITORING AGENCY NAME(S) AND ADDRESS(ES)
AFOSR
801 North Randolph Street
Room 732
Arlington VA 22203-1977

10. SPONSOR/MONITOR'S ACRONYM(S)

11. SPONSOR/MONITOR'S REPORT NUMBER(S)

12. DISTRIBUTION / AVAILABILITY STATEMENT
Approved for public release; distribution is unlimited

13. SUPPLEMENTARY NOTES

14. ABSTRACT
Active flow control using MEMS-based microactuators holds tremendous promise for achieving laminar flow control and drag reduction for a wide class of aircraft. In order to achieve effective control it is necessary to have a complete understanding of the fundamental instability processes that apply to a particular boundary layer and to develop a sensor and actuator system that is capable of providing an appropriate control input to that boundary layer. In the present work, crossflow-dominated swept-wing boundary layers are the primary interest. These boundary layers are known to undergo a highly nonlinear transition process that involves, in low-disturbance environments, stationary waves of longitudinal vorticity. These stationary waves have to potential to be controlled or suppressed by an appropriate surface roughness configurations that could be provided by MEMS-based actuators. The work performed here consists of a parallel experimental and hardware development efforts. The breakdown phase of the crossflow instability is investigated in the experiments in an effort to determine an appropriate control input. A MEMS-based roughness actuator system is developed to provide controlled roughness inputs. The results of the experimental phase conclusively demonstrate that the destabilization of a high-frequency secondary instability is responsible or breakdown. The MEMS development effort did not produce a useful control device because of certain shortcomings in the present state of MEMS fabrication quality control and overall system integration.

15. SUBJECT TERMS
transition control; MEMS; stability; secondary instabilities

16. SECURITY CLASSIFICATION OF: UNCLASSIFIED			17. LIMITATION OF ABSTRACT	18. NUMBER OF PAGES	19a. NAME OF RESPONSIBLE PERSON William S. Saric
a. REPORT UNCLASSIFIED	b. ABSTRACT UNCLASSIFIED	c. THIS PAGE UNCLASSIFIED	UNLIMITED	193	19b. TELEPHONE NUMBER (include area code) (480) 965-2822

Standard Form 298 (Rev. 8-98)
Prescribed by ANSI Std. Z39.18

ASU
ARIZONA STATE UNIVERSITY

August 24, 2001

The Air Force Office of Scientific Research (AFOSR)
AFOSR NA (Attention: Thomas J. Beutner)
801 North Randolph Street, Room 732
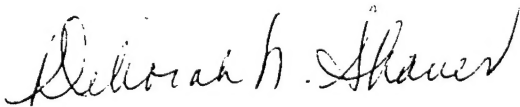Arlington VA 22203-1977

Subject: Final Technical Report

Reference: AFOSR Grant F49620-97-1-0520, "Control of Transition in Swept-Wing Boundary Layers using MEMS Devices as Distributed Roughness."

Arizona State University is pleased to provide an original and two copies of the final technical report for the referenced grant. This report covers the period 7/1/97- 12/31/00.

Your support of Dr. Saric's research is greatly appreciated. If you have questions or require any additional information, please contact me at (602) 965-1158.

Sincerely,

Deborah N. Shaver
Lead Sponsored Projects Officer

Enclosures

xc: Dr. William S. Saric
       ASU XAA 0034/TE
       AFOSR/PKA (letter only)

Abstract

Active flow control using MEMS-based microactuators holds tremendous promise for achieving laminar flow control and drag reduction for a wide class of aircraft. In order to achieve effective control it is necessary to have a complete understanding of the fundamental instability processes that apply to a particular boundary layer and to develop a sensor and actuator system that is capable of providing an appropriate control input to that boundary layer. In the present work, crossflow-dominated swept-wing boundary layers are the primary interest. These boundary layers are known to undergo a highly nonlinear transition process that involves, in low-disturbance environments, stationary waves of longitudinal vorticity. These stationary waves have to potential to be controlled or suppressed by an appropriate surface roughness configurations that could be provided by MEMS-based actuators. The work performed here consists of a parallel experimental and hardware development efforts. The breakdown phase of the crossflow instability is investigated in the experiments in an effort to determine an appropriate control input. A MEMS-based roughness actuator system is developed to provide controlled roughness inputs. The results of the experimental phase conclusively demonstrate that the destabilization of a high-frequency secondary instability is responsible for breakdown. The MEMS development effort did not produce a useful control device because of certain shortcomings in the present state of MEMS fabrication quality control and overall system integration.

List of Figures

vii

xi

boundary layers where the experience has been that although a MEMS element can reduce drag, it does so only in an area of the same order as the MEMS element itself. This implies that to achieve significant drag reduction of an already turbulent boundary layer, essentially all of a vehicle's skin would need to consist of MEMS actuators. This approach would clearly have enormous manufacturing and maintenance cost and also enormous power requirements. perhaps more than the power that could be saved through such an approach.

If practical control of an unstable laminar boundary layer is to be achieved using MEMS-based actuators. a significant question remains: What is the mechanism that triggers the final breakdown of the laminar flow? Until this stage of the process is understood. transition prediction based on a correct physical model will be impossible.

It is the intent of this work to provide a detailed experimental description of the mechanism or mechanisms that are responsible for the breakdown of laminar flow at the last stage of swept-wing boundary layer transition and, simultaneously, to design, construct, and implement a MEMS-based microactuator system that is capable of controlling the transition process on swept-wings. In the experimental phase, what will be of principal interest is the possibility that breakdown is caused either by a secondary instability or by an absolute instability that is present in the distorted velocity field resulting from the nonlinear primary instability. Both a secondary instability and an absolute instability have been shown to be present in rotating disk flow, the model problem for swept wings, and hence both are candidates for swept-wing breakdown mechanisms. The MEMS actuators will play a significant role in the experimental objectives because they will provide a critical experimental capability as variable roughness elements that will be needed to make this assessment.

1.2   Introduction to crossflow transition

The basic features of swept-wing boundary layers are as follows. In the inviscid region outside a swept-wing boundary layer. the combined influences of wing sweep and favorable pressure gradient produce curved streamlines at the boundary-layer edge. Inside the boundary layer the streamwise fluid velocity is reduced but the pressure gradient is unchanged. Thus. within the boundary layer, a balance between centripetal acceleration of the fluid elements and the external pressure gradient does not exist, and a secondary flow results. This secondary flow is directed perpendicular to the external streamline, toward the streamline's center of curvature. and it is therefore referred to as crossflow. Upstream of the pressure minimum. the crossflow is directed inboard (for standard swept-back configurations). Downstream of the pressure minimum, the crossflow is outboard. A schematic of a crossflow-producing streamline is shown in Figure 1. The associated streamwise, crossflow. and resolved boundary-layer velocity profiles are shown in Figure 2. Notice that the crossflow velocity is zero at the wall where the no-slip condition applies. and it approaches zero at the boundary-layer edge where pressure gradient and streamline curvature balance. Because of these boundary conditions. the crossflow velocity profile has an inflection point. It is well known that an inflection point in a boundary layer is a sufficient condition for an inviscid instability. This means that the transition behavior for swept wings is fundamentally different from that of unswept wings because the unswept configuration is subject to the viscous Tollmien–Schlichting (T–S) instability mechanism.

The fact that swept-wing boundary layers are subject to a different type of instability was first discovered by Gray (1952) during a flow-visualization flight test experiment. Soon thereafter. Gregory. Stuart & Walker (1955) produced their classic work that shows the same crossflow instability mechanism is also present for rotating disk boundary layers. In

The receptivity mechanism for the stationary vortices that are important for transition in low-disturbance environments is surface roughness. This was conclusively established by Müller & Bippes (1989), who translated a swept flat-plate model relative to the test section and found that the recurring stationary transition pattern translated with the model. Therefore the instability features had to be related to model roughness rather than to fixed features of the freestream flow generated by nonuniformities of the screens or other effects. Juillen & Arnal (1990) find that for isolated roughness elements the von Doenhoff & Braslow (1961) correlation that describes the limit for bypass transition is correct.

Roughness studies by Radeztsky, Reibert & Saric (1999) show that the characteristics of isolated 3-D roughness play a very important role in transition behavior. Roughness is most effective at generating crossflow disturbances at or just upstream of the neutral point. $x/c = 0.02$ in Radeztsky et $al.$'s experiment. The roughness diameter must be greater than 10% of the most amplified stationary wavelength to be effective, and the transition location is quite sensitive to roughness height even for roughness Reynolds numbers as low as $Re_k = 0.1$. Natural surface-roughness amplitude can also play a significant role in transition location. Radeztsky et $al.$ (1999) find that a decrease in surface-roughness amplitude from 9.0 μm rms to 0.5 μm rms delays transition from $x/c = 0.40$ to 0.61 for $Re_c = 2.7 \times 10^6$. Another decrease to 0.25 μm rms delays transition even further to $x/c = 0.68$. Radeztsky et $al.$ (1999) also determine that transition behavior is insensitive to sound even at amplitudes as high as 95 dB.

A number of theoretical and computational approaches to swept-wing boundary-layer receptivity have been applied. Some of the more recent include an adjoint equation approach by Fedorov (1989), a PSE approach by Herbert & Lin (1993), and a DNS approach by Spalart (1993). Crouch (1994) and Choudhari (1994) both consider the receptivity of Falkner–Skan–Cooke (FSC) boundary layers as perturbations of a parallel boundary layer. The framework of their approaches allowed both the surface roughness and acoustic freestream disturbances to be considered as receptivity sources. Choudhari (1994) extends his work to consider acoustic-wave-angle effects and a variety of different roughness configurations including isolated roughness, roughness arrays and lattices, and distributed random roughness. Crouch (1994) emphasizes a framework equally applicable to T–S and crossflow disturbances. Both authors note that because traveling-wave receptivity scales with two small parameters, the freestream velocity-fluctuation amplitude and surface-roughness amplitude, whereas the stationary-wave receptivity scales with only one, the surface roughness, it can be expected that stationary waves will dominate for low-disturbance environments and that traveling waves will only appear for large freestream acoustic variations. The experiments of Radeztsky et $al.$ (1999) confirm this expectation.

A more recent approach by Collis & Lele (1999) begins by solving the steady Navier–Stokes equations in the leading-edge region of a swept parabolic body and then using that solution as a basic state for a linearized steady disturbance system that includes surface roughness. Comparing the results of this approach to those obtained by Choudhari (1994) and Crouch (1994) shows that receptivity to surface roughness is enhanced by convex surface curvature and suppressed by nonparallelism. Neglecting nonparallelism causes the local approach to overpredict receptivity by as much as 77% for the most amplified stationary crossflow wavenumber. The error introduced by neglecting nonparallelism is most severe for wavelengths in the range most amplified by the crossflow instability and for roughness close to the first neutral point. The implication is that amplitude-based transition-prediction methods need to employ a receptivity model that includes nonparallelism because the crossflow modes that dominate transition are most strongly affected by this influence.

4

What has proven to be the most effective means of modeling the crossflow instability is an approach using nonlinear parabolized stability equations (NPSE). Nonlinear parabolized stability codes incorporate mean-flow modification produced by the stationary vortices and include surface curvature and nonparallel effects. Recently, both Malik, Li, Choudhari & Chang (1999) and Haynes & Reed (2000) have used the NPSE approach to produce excellent computational agreement with the experiments of Reibert *et al.* (1996) that demonstrate the nonlinear growth and saturation of stationary crossflow vortices. The computational results confirm that saturation amplitudes are independent of the initial crossflow amplitude if it is sufficiently high to cause saturation. The NPSE codes further demonstrate that the disturbance growth is sensitive to very weak surface curvature.

An alternative DNS approach to the late transition stages was undertaken by Wintergerste & Kleiser (1996). These computations are an FSC approximation of the DLR swept flat-plate experiment. The emphasis of these calculations was to examine the vortex structure with a more highly resolved grid than the earlier DNS crossflow calculations by Meyer & Kleiser (1989). The approach by Wintergerste & Kleiser (1996) is local, temporal stability with local parameters to match 80% chord: $R = 826$, sweep angle $\varphi_e = 46.9°$, and Hartree parameter $\beta_H = 0.63$. These calculations identified the weak vortex that rotates counter to the main stationary crossflow vortex predicted by Malik *et al.* (1994), and they demonstrated breakdown to turbulence soon after, but the results do not appear to produce the secondary instability described below.

1.2.3 Implications for N-factor transition prediction

The strategy most often employed for transition prediction is known as the e^N method, proposed independently by van Ingen (1956) and Smith & Gamberoni (1956). This method consists of finding the envelope of the growth curves of all possible instability modes using linear stability theory. Transition is expected to occur at the first point for which the ratio of any single mode's amplitude to its initial amplitude exceeds a threshold value. The threshold for transition is determined experimentally and is expressed in exponential form, hence e^N. Typically, $N \approx 9$ leads to transition, although the N-factor can vary widely depending on a number of factors. Using this approach, transition experiments are performed either in a wind tunnel or in flight to produce an N-factor for transition. This N-factor is then applied to similar configurations in the hope that the value will be accurate enough for design purposes. Typically, wind-tunnel tests at low Reynolds numbers are used to produce N-factors that are then applied to flight conditions.

Successful implementation of the e^N method relies on a number of assumptions. The first and most fundamental requirement is that the process by which transition occurs in the baseline experiment must be the same process as that occurring in practice. Second, the method assumes that there is a uniform distribution of initial disturbance amplitudes across all of the relevant instability modes and that the amplitudes in the experiment are equivalent to those in practice. The last assumption is that the growth of the instability modes is accurately described by linear stability theory throughout most of the transition region, although this is the weakest requirement because some degree of nonlinearity may be lumped into the particular N-factor. However, each of these assumptions is strongly violated in swept-wing transition.

Perhaps the most serious flaw is that the character of the transition process—whether it is dominated by stationary or traveling waves—depends on the magnitude of freestream disturbances. This means that while the transition mechanism in flight is always stationary

Given these two possible breakdown mechanisms, the objectives of the current work are as follows. The first is to establish a swept-wing model that provides a crossflow boundary layer with a very well controlled primary instability. The second is to determine if a secondary instability does exist, and if so, to determine under what conditions it becomes unstable, its growth characteristics, and ultimately where it triggers breakdown. The data presented will be suitable for comparison with numerical simulations. The third objective is to determine whether the swept-wing boundary layer shows any evidence of supporting an absolute instability. Although this has been observed in a rotating disk boundary layer, no evidence has been observed for swept wings. However, the absolute instability experiment poses special challenges for maintaining a good basic state, even beyond those of the secondary instability, so it may simply be that the absolute instability experiment could not be performed before now. In parallel with these three experimental objectives, the fourth objective is to design, install and test MEMS-based roughness actuators for use as laminar-flow-control devices on a swept-wing model.

The layout of this document is structured around these four objectives. This introductory chapter has presented a review of the receptivity and primary instability aspects of crossflow stability—features that are important both for the secondary instability and absolute instability experiments. In Chapter 2, a description of the experimental facility, hardware, and techniques that are common to both the secondary instability and absolute instability experiments is presented. That chapter includes a description of the design philosophy of the swept-wing experiment. The philosophy is not restricted to just the present work but encompasses the experience of the last decade of swept-wing experiments. This section also includes a detailed description of the MEMS development efforts. Chapter 3 consists of the investigation of the secondary instability as a crossflow breakdown mechanism. The chapter begins with a review of the literature specific to the secondary instability, then progresses to specific experimental techniques, results, and discussion. Chapter 4 presents the absolute instability in the same manner: a self-contained literature review, experiment description, and results and discussion. Overall conclusions that compare the two instabilities are presented in Chapter 5.

tion. Without an indication that this could occur, and if so, for what parameter range, there is no reason to make the experiment more complicated than necessary.

The next idea is to provide a model with boundary layers that are sufficiently thick to allow for relatively easy and well-resolved boundary-layer velocity measurements and to simultaneously provide sufficient crossflow to cause transition. These requirements conflict because thick boundary layers can be achieved by restricting the experiment to low Reynolds numbers, but at too low a Reynolds number the instability would not be strong enough to produce transition. One of the first means of improving the prospect for strong crossflow and a thick boundary layer is to select a pressure gradient that locates the pressure minimum as far back as possible. This means that the boundary layer can develop over the longest possible distance without the boundary layer becoming unstable to T–S waves and without the crossflow direction changing. The pressure gradient can also be used to enhance the crossflow by making the pressure gradient as strong as possible. Although this means that strong negative lift is preferable, experience at the Unsteady Wind Tunnel has shown that the wall liners used to maintain spanwise-uniform flow are difficult to construct and maintain when there is strong lift. Therefore a pressure contour that provides a strong pressure gradient with a late pressure minimum at zero lift is the optimum configuration. Enhanced crossflow can also be produced by increasing the sweep angle of the wing. However, exceeding $\Lambda = 45°$ becomes impractical for the hotwire traverse system.

Starting with Dagenhart (1992), all of the previous Unsteady Wind Tunnel crossflow stability experiments employed a swept-wing model with an NLF(2)-0415 profile (Somers & Horstmann, 1985) and 45° sweep. The NLF profile places the suction-side pressure minimum at 71% chord. Transition on this model is always observed upstream of 71% chord, so the T–S instability does not contribute to transition, nor does the Görtler instability, because the concave region also occurs downstream of 71%. The nose radius and sweep are such that leading-edge contamination is not present. The wing used in the current work, designated the ASU(67)-0315, was designed by Reibert around the same principles with the additional feature of generating significant crossflow at zero lift. The unswept chord length of the new model is 1.829 m, the sweep angle is 45°, and the angle of attack is set at $-3°$, the zero-lift angle. The theoretical inviscid pressure contour for this configuration, including the influence of the wind-tunnel walls, is computed using the MCARF code of Stevens et al. (1971) and is shown with the wing contour in Figure 3. The code does not account for displacement thickness growth on either the model or the walls.

2.2 Swept-wing model

The ASU(67)-0315 wing was constructed to provide a flexible test platform on which a variety of boundary-layer transition-control experiments can be conducted. To this end, the leading edge of the wing is not continuous, but includes a leading-edge slot in the middle third of the span that extends to approximately 20% chord. This slot accepts modular leading-edge inserts that can provide any sort of boundary-layer treatment, in particular the MEMS roughness actuators. The leading 10% chord of the main body of the model is a solid aluminum piece, hand polished to a 0.2-μm-rms surface finish. The remainder of the main body consists of an aluminum frame and foam core covered by fiberglass. The fiberglass construction means that the wing weighs approximately 350 kg, allowing it to be much more easily handled than the all-aluminum NLF wing. (The NLF wing weighs approximately 725 kg.) The model includes two lines of 29 suction-side pressure taps at various chord locations. The lines of taps are oriented in the X direction as indicated in Figure 4.

may be worse than if no control had been attempted, a much-more-robust actuator design must be developed for use in practice.

The work performed by the ASU group implementing the few defect-free MEMS actuators raised other serious questions about the applicability of MEMS actuators to *external* flow control given the current level of MEMS technology. Some of the key difficulties encountered were (1) implementing a flat silicon surface into a curved wing surface, (2) bonding the silicon wafer slices permanently to the aluminum wing, (3) maintaining a flush, no-roughness surface at·the wing/wafer surface, and (4) maintaining the elements and replacing failed elements without damaging nearby operative elements. The first and third problems, implementing a flat silicon surface into a curved wing surface and maintaining a good-quality, no-roughness junction are particularly important for control of the crossflow instability because of its sensitivity to leading-edge roughness. The MEMS devices, as designed, essentially required hand installation, and because this could not be accomplished while maintaining sub-micron-level surface quality at the silicon/aluminum or silicon/silicon junctions, the application of the MEMS wafers actually led to larger levels of *uncontrolled* surface roughness than the actuators themselves were capable of providing. The fact that the actuator strips were much longer (on the order of 100 mm) than the most unstable crossflow waves (10–16 mm) does not prevent difficulties, because even isolated roughness sites can be detrimental, as demonstrated by the experiments of Radeztsky *et al.* (1999).

Because the experiments require roughness with better quality control than the MEMS-based elements provide, a decision was made to manufacture at ASU a pneumatically activated roughness insert. This insert provides uniform activation of an entire array of elements on a slow time scale. This action is sufficient to perform the experiments of interest, but does not extend into the unsteady or non-uniform roughness forcing the MEMS-based actuators might provide. The pneumatically driven insert has the capability to vary the roughness height, a necessary component of the absolute-instability experiments. It has an interior chamber that is pressurized from a supply outside the wind tunnel, and a 12-mm-spaced spanwise array of 3-mm-diameter holes is drilled from the contoured upper surface of the insert into the interior pressure chamber. The array of holes is covered with a 25-mm-wide, 40-μm-thick strip of polyester tape, and when the interior of the insert is pressurized, the tape deforms into a periodic array of artificial roughness. The variable-amplitude roughness system provides a means of producing transient roughness forcing that is used to search for an absolute instability. A schematic of the small variable-roughness device is shown in Figure 6. In the future, such an insert could be manufactured with a MEMS-based valve controlling each element in the roughness array with the MEMS valves located inside the wing.

The chief difficulty associated with the new model is the quality of the surface that results from the installation of the modular pieces. It is known from the earlier work of Radeztsky *et al.* (1999) that micron-scale isolated roughness features of a surface are sources of crossflow receptivity. This means that even the smallest imperfections at the junctions between the small and large inserts and the large insert and the wing can produce deformations of the mean flow that could overwhelm any boundary-layer features generated by the roughness arrays that are intended to provide a uniform disturbance field. Fortunately, while crossflow boundary layers are extremely sensitive to 3-D roughness, they are not sensitive to 2-D (spanwise-constant) roughness. Crossflow requires a source of streamwise vorticity that 3-D roughness provides, but 2-D roughness does not. So, while the corners of the junctions pose a problem, the long sides of the variable-roughness insert and the large leading-edge insert that run in the span direction do not adversely affect the flow. Because of the large

this tank at 0.15 atm to a computer-controlled valve that regulates the pressure inside the variable-roughness insert. The system includes a pressure transducer, the test-section static pressure sensor, and the pressure coefficient data that give the pressure difference across the tape membrane. With no air flow in the tunnel, the relationship between the pressure difference and the displacement is measured using a confocal laser displacement sensor that is described below. A family of pressure-versus-displacement curves is shown in Figure 9. While precise control of the roughness height could not be achieved using the system, the general trend is acceptable for the purposes of the absolute instability experiment where simply high and low roughness amplitudes are needed. The shapes of the activated roughness elements for two pressure levels are shown in Figures 10 and 11.

2.4 Wind tunnel, test section, and traverse

The experiments are conducted in the Arizona State University Unsteady Wind Tunnel. The Unsteady Wind Tunnel is a closed-loop, low-speed, atmospheric-pressure facility originally built and operated by Dr. Philip Klebanoff at the National Bureau of Standards. Following Dr. Klebanoff's retirement, the tunnel was moved to Arizona State University and reconstructed between 1984 and 1988 with numerous flow-quality improvements. The design and operation of the wind tunnel are intended to provide the best possible conditions for conducting transition-to-turbulence experiments. With this in mind, quite a significant investment has been made in high-quality screens, honeycomb, a settling chamber, a contraction cone, turning vanes, and vibration-isolation strategies. The fan consists of a 1.8-m-diameter, 9-rotor, 11-stator axial stage, powered by a 150-hp DC motor. The motor is computer controlled and can maintain speed to within 0.01% of the set point. Further details of the facility's design and capabilities are given by Saric (1992), and details of the computer-control capabilities are described by Reibert (1996). An schematic layout of the Unsteady Wind Tunnel is shown in Figure 12.

The key features of the tunnel that bear directly on the present experiment are the freestream conditions in the test section. The maximum freestream speed that can be achieved in the test section is 35 m/s, and as noted above, any fan speed can be held to within 0.01% (although this level of precision is beyond the accuracy to which the freestream speed can be reliably measured). The maximum speed corresponds to a chord Reynolds number of approximately 3.8×10^6 for the swept-wing model. The baseline operating point for the current experiment is $Re_c = 2.4 \times 10^6$, and for the temperatures at which the tunnel operates, this corresponds to freestream speeds between 22 and 23 m/s. The baseline Reynolds number provides the best combination of experimental parameters. Breakdown occurs near 50% chord, in the middle of the traverse's range, and the boundary layer is reasonably thick (3 mm) in the transition region, so well-resolved boundary-layer profiles are easy to obtain. Wind-tunnel heating is a concern at this speed but it is not so severe as to be unmanageable. The freestream turbulence level that is achieved in the test section is exceptionally low due to the very careful attention that is paid to turbulence-control devices upstream and vibration control. At 20 m/s, the turbulence level u'/U_∞ is less than 0.02% (using a 2-Hz high-pass filter). Both the v' and w' fluctuation levels are less than half that of u'. The sound level in the test section at the same conditions is below 85 dB. Recall that Deyhle & Bippes (1996) found that stationary waves dominate crossflow boundary layers only below $Tu = 0.15\%$ (where Tu includes contributions of all three fluctuating-velocity components), so the low turbulence level of the Unsteady Wind Tunnel is essential for conducting a stationary-wave-dominated experiment. Perhaps the most significant limitation

14

Direction	X, axial	Y, wall normal	Z, vertical
Travel	1250 mm	100 mm	175 mm
Step Size	12 μm	0.7 μm	1.3 μm

Table 2.1: Traverse Capabilities.

Reynolds number range. A schematic of a 45° swept wing and liners for the zero-lift condition is shown in Figure 16. The liner design and construction techniques are thoroughly documented by Dagenhart & Saric (1999) and Radeztsky (1994), but the basic idea is as follows. First the pressure distribution predicted by the MCARF code is used to determine the surface of all streamlines passing through an arbitrary horizontal (X, Z constant) line upstream of the model. The two sides of the surface are constructed in full scale using styrofoam, and these two pieces are attached to the ceiling and floor of the test section to provide the root and tip boundary conditions, respectively. The suction-side and pressure-side walls of the test section are not treated with liners because these surfaces do not adversely affect the difficulty of stability calculations. The pressure field about the wing is slightly different from what it would be in free flight, but computations can use the pressure field calculated with these walls in place. From an experimental standpoint, suction-side and pressure-side wall liners would be significantly more challenging to implement, so not including these is a significant advantage in terms of experimental simplicity.

The extent to which the model and liners produce the conditions predicted by the inviscid code can be assessed by comparing the pressure measured using the surface pressure taps to the pressure distribution that is shown in Figure 3. The pressure at each tap is measured relative to the freestream static pressure and the difference is normalized by the freestream dynamic pressure, $\rho U_\infty^2 / 2$. This gives 3-D pressure coefficients $C_{p,3}$. (The data are acquired using a 10-torr differential pressure transducer described below.) The $C_{p,3}$ measurements differ from $C_{p,2}$ predictions shown in the figure only in terms of the normalizing pressure. The $C_{p,2}$ values are normalized using the component of velocity perpendicular to the leading edge, whereas the $C_{p,3}$ data use the total freestream velocity. The relationship is $C_{p,3} = C_{p,2} \cos^2 \Lambda$. Because $\Lambda = 45°$ for this experiment, $C_{p,3}$ is simply one-half of $C_{p,2}$.

Figures 17–19 give the 3-D pressure coefficient distribution at $Re_c = 2.0 \times 10^6$, 2.4×10^6, and 2.8×10^6, respectively. The measurements are for the actual $-3.4°$ angle of attack, but the computed curve reflects the design angle, $-3°$, for which the liners were constructed. The results at the three Reynolds numbers are nearly indistinguishable. In each case the actual pressure is higher than the predicted value at all points upstream of 90% chord. However, the pressure gradient—the feature that affects boundary-layer stability—is approximately what is predicted by MCARF throughout the region of interest for the experiments, $0.30 < x/c < 0.60$. Furthermore, there is not an appreciable pressure difference across the span in this region. Such a difference would clearly render crossflow velocity predictions inaccurate. These results are quite similar to those obtained by Reibert et al. (1996) for the NLF wing. The exceptionally good agreement between those experimental results and the computations of Haynes & Reed (2000) indicates that the experiment can proceed with these pressure contours.

effectively measured. With any other system (e.g., LDV or PIV) no such filtering technique is available, so measurements of small velocity fluctuations are impossible. There is always some concern that introduction of a flow-intrusive device such as a hotwire can change the behavior of a system being studied. This is especially true for stability experiments where very small influences can become quite significant. For the present experiment this need not be a concern for several reasons. First, extensive naphthalene flow-visualization experiments of the previous investigators (in particular Dagenhart & Saric, 1999; Radeztsky et al., 1999; Reibert et al., 1996) show that hotwire measurements correspond exactly to behavior indicated by the flow visualization, for which no intrusive devices exist. Second, there is excellent correspondence between the experimental results of Reibert et al. (1996) and the computational results of Haynes & Reed (2000), so there is additional reason to believe that the boundary-layer behavior is unchanged by the presence of a boundary-layer hotwire. Finally, in the breakdown region the instability mechanism is driven by an inviscid Kelvin–Helmholtz-type instability that does not depend on the pressure gradient (the feature of the flow that would be modified by the presence of the hotwire and sting), but instead depends on the shear layer that is established by the stationary crossflow waves well upstream of the transition location.

Although in large part the fluctuating components are the most interesting features of these experiments, the correlation of the fluctuating components to the underlying mean flow is also of interest. This means that a very careful mean-flow calibration procedure is required that must include an accurate temperature compensation. The calibration procedure is performed daily to minimize long-term variations in the hotwire response. The calibration approach is somewhat different from other recent projects at the Unsteady Wind Tunnel (Reibert, 1996; Carrillo, 1996), so it will be described here in detail.

The basic idea is that the voltage output of the hotwires must be calibrated with respect to the upstream pitot tube and that this calibration must be valid for any temperature encountered during the experiment. To perform the calibration, the wind tunnel is run through a range of speeds at two temperature levels, and from this the output of the hotwires is related to the velocity/temperature state measured by the upstream pitot tube and thermometer. The pitot tube is an excellent velocity-calibration standard for steady flows because the instruments used to measure the static and dynamic pressures and the temperature all have good accuracy, precision, and long-term stability. Additionally, because the pressure transducers include independent heaters, they are immune to environmental temperature variations.

The calibration approach consists of three elements: a one-time position calibration, velocity calibration, and temperature compensation. The first, position calibration, is necessary because the entire region of the test section that is accessible by the traverse is within the zone affected by the pressure field of the wing, so the velocity measured by the pitot tube is not the velocity measured by the hotwires. To account for this, arbitrary calibration positions for the hotwires are chosen and the velocities at those points are measured using a temporary pitot tube. Then these velocities are related to the freestream velocities measured by the fixed pitot probe. For the current work, the calibration position is defined as 60% chord, midspan, with full retraction of the sting. Full retraction places the boundary-layer probe approximately 55 mm from the wall and the freestream probe approximately 180 mm from the wall. This position is selected because it minimizes the V and W components of velocity and thus offers the best velocity measurement using the temporary pitot probe. At the calibration position, the pitot probe measurements show that the velocity ratio between the boundary-layer calibration position and the upstream

The actual procedure used to find the constants in equations (2.3) and (2.5) is as follows. First, the tunnel speed is varied from 1 m/s to 27 m/s (as measured by the pitot probe) in increments of 1–3 m/s while the pitot velocity, temperature, and hotwire voltages are recorded at each speed. Then the tunnel is run at high speed (typically 31 m/s) until the temperature has increased by some increment, typically 5 °C. Once the higher temperature is reached, the tunnel velocity is decreased and again the pitot velocity, temperature, and voltages are recorded. During the ramp-down phase, the velocity targets are changed to the actual values observed during the ramp-up phase. This eliminates the need for a strict velocity tolerance for the ramp-up phase (thus reducing calibration time) but increases the overall calibration quality by reducing the velocity differences of the hot/cold data pairs. Using the data obtained in these two series of measurements, the temperature-compensation coefficient is calculated for each of the velocities using equation (2.3). Using these compensation coefficients, the ramp-down voltages are adjusted to yield the velocity as a function of temperature-compensated voltage, and these data are fit to equation (2.5).

The velocity target adjustment mentioned above is one improvement to the hotwire techniques employed during this experiment. Two other significant improvements over previous experiments are made as well. First, the voltages obtained during the ramp-down phase are modified via linear interpolation to the exact speed measured during the ramp-up phase. This greatly improves the temperature-compensation coefficient calculation because errors in E^2 due to small velocity errors (~ 0.1 m/s) can be on the order of those due to 5 °C temperature variations, especially at low speeds. Second, instead of using second- and fourth-order polynomial fits to model equations (2.3) and (2.5), respectively, the fully nonlinear models are used. To perform the nonlinear[2] least-squares fit, the Levenberg–Marquardt method described by Press *et al.* (1992) is employed. The principal advantage is that the nonlinear equations provide a model that describes the heat transfer more accurately than the polynomial basis functions, resulting in reduced deviations of the data from the computed curve. Bevington (1969) shows that expected variance of data points relative to a fit is the reduced chi squared, χ^2/ν. This term is the sum of the squared deviations, normalized by the number of degrees of freedom of the fit (i.e., the number of data points minus the number of model parameters). The nonlinear models improve the reduced chi squared relative to the polynomial models not only by reducing the squared deviations but also by reducing the number of model parameters from eight (five for the calibration and three for the temperature compensation) to six (three each for the calibration and compensation). The effect of the various improvements on the temperature-compensation curve is shown in Figures 20 and 21. Figure 20 shows a polynomial and nonlinear fit without interpolation. Figure 21 shows the nonlinear fit using interpolated data. The reduced chi squared is 2.6×10^{-5} for the polynomial fit without interpolation, 2.1×10^{-5} for the nonlinear fit without interpolation, and 1.8×10^{-6} for the nonlinear fit with interpolation. Clearly the nonlinear model with interpolation produces the best result. Beyond simply reducing experimental uncertainty, the benefits of this approach are that the time and heating level required each day during calibration are reduced. Sufficiently good results can be obtained with a relatively small temperature rise.

---

[2]In this context, nonlinear refers to the form of the model parameters. For linear fits, the model parameters must appear linearly, but the basis functions may be nonlinear.

sting and boundary-layer hotwire are manually adjusted for the upcoming experiment and every experiment is restricted to a particular chord location. Prior to any adjustments, the boundary-layer wire is vertical and the probe support extends in the negative X direction. First, the boundary-layer probe support is pivoted (about the Z axis) so that it swings toward the wing in the (X, Y) plane. This rotation is required so that when the sting is moved in the $-Y$ direction (toward the wing) during the experiment, the boundary-layer wire itself, and not the sensor's tines, the probe holder, or the sting, contacts the wing first. This orientation allows the boundary-layer measurements to be taken as close as possible to the wing. Next, the probe support is rotated about its axis so that the hotwire sensor is parallel to the surface of the wing. The rotation angle of the probe support depends on the chord location, but not on span. This is why measurements always proceed in the span direction. Because the hotwire's orientation changes depending on the measurement location, it is particularly important that comparisons between computations and the experiments described here be performed with special attention to the velocity-field projection. Because of the nature of the experiment (i.e., the hotwire senses only a projection of the local velocity), it is impossible for the full velocity vector to be reconstructed from single hotwire measurements. However, because all components of velocity are available from a computation, a projection of the computational data that mimics the physical transformation introduced by the hotwire orientation can be performed to yield a valid comparison between the experiment and computational models. In the experimental results presented in this document, velocities are referred to as U, U_{edge}, and u'. These represent the projection of the mean-flow, boundary-layer-edge, and fluctuating-velocity components, respectively, onto the hotwire's orientation.

2.6.2 Boundary-layer velocity profiles

Boundary-layer velocity-profile measurements serve to acquire the projection of the mean-flow velocity onto the hotwire as the wire is traversed in the Y direction from outside the boundary layer to very close to the wing. The purpose of the scans in the present experiment is typically not to find the profiles themselves, but to locate the surface of the wing very accurately in the traverse's coordinate system. When performing an experiment, the position of the traverse can be controlled very precisely in the global frame of reference. However, in this frame the hotwire sensor's position relative to the surface is not known. This is because the hotwire is adjusted manually prior to measurements at each new chord location, so its position in the absolute traverse frame changes. Moreover, the surface of the swept-wing model is not in perfect alignment with the traverse-oriented coordinate system, nor is the surface of the model flat along the chord lines over which the measurements are obtained. The misalignment of the model and traverse is quite small, less than 1 mm over the 175-mm Z range of the traverse. Irregularities that are a result of the curing process of the fiberglass surface and subsequent hand finishing produce variations on the order of 100–200 μm along constant chord lines. These irregularities cannot be accounted for in an overall way and must be taken into account locally. Because of these issues, the position of the wall is determined using boundary-layer profiles for every series of measurements in the boundary layer.

Using boundary-layer profiles to locate the surface utilizes the fact that the velocity at the surface is zero because of the no-slip condition. Approaching the wing while taking a series of velocity measurements and fitting these velocity data to a velocity-profile model produce a surface-position estimate via extrapolation to zero velocity. The operation must

2.6.3 Spanwise-line and full-field scans

Once the boundary-layer profiles have been used to find accurate surface-position estimates, the measurements of interest can begin. There are two principal types used: spanwise-line velocity scans for the absolute instability experiments and full-field velocity scans for the secondary instability experiments. The line scans proceed along the z direction at constant chord, x/c, and distance from the surface, Y. The mean flows measured by these scans are useful for producing stationary-mode amplitudes. These are obtained by taking the Fourier transform of the velocity data along the span direction. This technique is similar to that used by Reibert *et al.* (1996) and Saric *et al.* (1998). To begin such a scan, the following parameters are supplied: the starting and ending span locations, the span step size, the offset in the Y direction at which the measurements are to be performed, the sampling duration, and the sampling rate. The first task performed is surface-position estimation using the boundary-layer-profile approach described above. The wall location is found at the starting, middle, and ending span positions, and the resulting data are fit to a polynomial that provides a surface estimate at all points along the span. With this estimate, the hotwire is moved to the position at the starting span location and the correct surface offset, and the first point is acquired. After this point, the traverse is moved one step in z and the Y position is adjusted to maintain the correct offset. After a number of acquisitions, the tunnel parameters are checked and the speed is adjusted if necessary to account for any heating that would increase the boundary-layer thickness. For the absolute instability measurements, multiple scans at the same x/c location are desired, so after each scan in z, the hotwire is returned to the starting position and the operator is given the option of changing parameters or ending the experiment.

Whereas the line scans are designed to be performed very rapidly, the full-field scans used for the secondary instability measurements are designed to provide very detailed velocity data for all points in the boundary layer. These scans provide mean- and fluctuating-velocity data on a 2-D grid of points at a particular x/c location. Typically the spacing in Y is 200–300 µm and the spacing in z is 1.0 or 1.2 mm. This provides 15–20 points in the Y direction from the surface to outside the boundary layer and 12–15 points in the z direction, enough to span somewhat more than one crossflow wavelength. Full-field scans begin with a boundary-layer-profile measurement to locate the surface at the starting z position. Once the surface is located, the hotwire is moved to the starting Y position that is specified in the control program, and the mean and fluctuating data are acquired. Then the wire is moved out to the next Y location. After the desired points at the first z station are acquired, the hotwire is moved to the next span location and a new boundary-layer profile is obtained. The second and subsequent profiles are obtained more quickly than the first because a fairly good surface-location estimate exists from the previous profile, so these scans need not start outside the boundary layer. Instead they are begun well inside using the previous point's surface-location estimate and boundary-layer-edge velocity as parameters. The process is repeated until the entire domain is mapped.

2.6.4 Fluctuating-velocity spectra

When the line and full-field scans are performed, both mean-flow and fluctuating-velocity data are obtained. Because the interest here is in the process by which the instabilities grow and turbulence appears, the fluctuations are of particular interest. At each measurement position the mean output of the hotwire anemometer is obtained in the usual way, and the fluctuating output is obtained by high-pass filtering (typically at 20 Hz) to remove the

Chapter 3

Secondary Instability

The review of the crossflow instability on swept wings presented in Chapter 1 concentrated on two aspects: receptivity and the primary instability. Work of the past decade has shown the primary instability to be subject to nonlinear growth, stationary-wave interactions, and amplitude saturation. This aspect of the flow is now well understood both experimentally and computationally. Excellent agreement between these approaches has been demonstrated by the experiments of Reibert *et al.* (1996) and the computations of Haynes & Reed (2000) and Malik *et al.* (1999). Receptivity is not as well understood, but progress continues, and the recent computational results of Collis & Lele (1999) have provided a renewed impetus for experimental work. Despite achievements on these fronts, the actual mechanism responsible for the breakdown of laminar flow remains unclear.

Most of the important data regarding breakdown have come from observations of transition location. These observations give only general information and do not yield any specific clues about breakdown mechanisms. What transition location data have shown is that in some cases, the transition location is insensitive to roughness amplitude, while for other conditions, transition location is very sensitive to roughness. Specifically, recall that the early randomly distributed roughness studies by Radeztsky *et al.* (1999) showed that for $Re_c = 2.7 \times 10^6$, a decrease of the roughness amplitude from 0.5 μm rms to 0.25 μm rms delayed transition from $x/c = 0.61$ to $x/c = 0.68$. Contrast this with the results of Reibert *et al.* (1996) for $Re_c = 2.4 \times 10^6$ that show a change in transition location from $x/c = 0.49$ to only $x/c = 0.52$ when 12-mm-spaced, 6-μm-high artificial roughness is replaced with 12-mm-spaced, 48-μm-high roughness. Although the Radeztsky *et al.* (1999) experiment is for naturally occurring roughness and the Reibert *et al.* (1996) experiment uses artificial arrays of periodic roughness, the wide variety of transition behavior observed indicates that transition of crossflow boundary layers can be quite complicated. In order to better understand—and eventually predict—this behavior, one must be capable of understanding breakdown. In particular it is important to understand what triggers breakdown at the specific location at which it is observed.

There are at least two explanations for why the transition behavior is insensitive to roughness amplitude for a sufficiently large initial condition. The first of these is that a secondary instability grows in the saturated mean-flow region produced by sufficiently large amplitude leading-edge roughness, and it is this secondary instability that leads to transition. There have been a few experimental observations that suggest that this is the mechanism, and these will be discussed below. Another possibility is that at some point in the boundary layer, the flow becomes absolutely unstable. This would mean that disturbances could grow in time to large amplitudes at a fixed spatial location. If this is the

mode. The reason for the difference in the observed secondary instability modes is unclear. In a later computational work on the secondary instability of Görtler boundary layers, Li & Malik (1995) were able to determine different growth rates for both of the modes observed by Swearingen & Blackwelder (1987), and it appears as if the appearance of a particular mode depends strongly on the parameters of the Görtler boundary layer and on the receptivity of the individual modes.

The maps of velocity-fluctuation intensity produced by Swearingen & Blackwelder (1987) are 2-D sections in the spanwise/wall-normal plane. These maps show that the fluctuations are confined to a stationary multilobed structure. Two lobes exist high in the boundary layer at maxima of $\partial U/\partial z$ and a single mode exists close to the wall near the center of the low-momentum upwelling region. The maximum amplitude of the fluctuations was found to grow exponentially at a rate two to five times more rapidly than the primary instability. The conclusions are that it is the secondary instability that is responsible for transition, and that the secondary instability is the result of inflection points of the streamwise flow when the second derivative is taken in the spanwise, not the wall-normal, direction.

With the investigations described above as a background, a high-frequency secondary instability was specifically investigated as a source of breakdown by Kohama, Saric & Hoos (1991). This experiment combined hotwire measurements and flow visualizations and was intended first to determine the location and behavior of the secondary instability mode relative to breakdown patterns that had been observed in naphthalene flow-visualization experiments conducted by Dagenhart & Saric (1999), and second to test the conjecture of Kohama (1987) that swept-wing breakdown is due to a secondary instability of the same type that affects rotating disk flow. The hotwire experiments consisted of two phases: single-point velocity-fluctuation spectrum measurements for various Reynolds numbers and single-line spanwise scans at constant chord and boundary-layer height. The flow-visualization tests were intended to correlate specific features of the hotwire measurements with surface shear-stress patterns.

A velocity spectrum result is given for $x/c = 0.4$, $y/\delta = 0.5$ (δ is not explicitly defined), and $U_\infty = 25$ m/s or $Re_c = 2.66 \times 10^6$. The spectrum (figure 8 in Kohama et al., 1991) shows traveling crossflow wave activity at 350 Hz and a very broad high-frequency peak centered near 3 kHz. The claim is that the high-frequency activity is a secondary instability caused by a Rayleigh instability of the inflection points in the wall-normal profiles of the streamwise mean flow, $U(y)$. The authors report that increasing the Reynolds number increases the amplitude of the high-frequency peak until the signal (as determined by the hotwire time trace) becomes turbulent, although no quantitative data are given characterizing this development.

Using a characteristic secondary instability frequency of 3.5 kHz and a 350-Hz traveling primary-wave frequency, Kohama et al. (1991) undertake a series of spanwise line scans meant to demonstrate the spatial correlation between secondary instability and mean-flow deformation features. The scans are obtained between $x/c = 0.40$ and 0.45 with the transition location at $x/c = 0.50$. The data reveal that both the low- and high-frequency disturbance amplitudes vary significantly over each wavelength of the stationary structure and that each mode has an amplitude peak close to the low-momentum upwelling location. The authors claim that the instability is located on opposite sides of this region, but this is difficult to observe in the data that are presented. In any case, the claim is that the streamwise velocity inflection points near the low-momentum region drive the flow to turbulence. The mechanism is an energy-production term involving v', and this activity is located near the boundary-layer edge at the location of the multiply inflected wall-normal

the FSC basic state and stability characteristics of this field were calculated. The mode shape of the stationary wave was taken from the earlier calculation and the amplitude was adjusted to match the experiment. Both the primary and secondary stability calculations were performed using local, temporal stability analysis.

The primary instability calculations successfully identified the most amplified stationary wavenumber, $\beta_0 = 0.4788$, where the nondimensionalizing length is the boundary-layer scale, $\delta = (\nu x / U_c^{\text{ext}})^{1/2}$. The orientation of this mode was also in good qualitative agreement with experimental observations, $4.73°$ from the inviscid streamline. Amplitude saturation was not captured because these were linear calculations.

The secondary instability calculations were performed at the same chord location using the saturated stationary-mode amplitude from the experimental measurements, $\epsilon_0 = 7.89\%$, where ϵ_0 is the maximum spanwise mean-flow velocity difference for all heights. The secondary-mode behavior was calculated using Floquet theory. In Fischer & Dallmann's approach, the perturbations of the spanwise-periodic mean flow, q', are written as $q' = \epsilon_1 q_1$, where

$$q_1 = \text{real}\left[\hat{q}_1(y, z) e^{i(\alpha_1 x - \omega_1 t)}\right], \tag{3.1}$$

$$\hat{q}_1(y, z) = e^{-i\sigma\beta_0 y} \sum_{k=-K_1}^{K_2} \hat{q}_{1,k}(y) e^{ik\beta_0 z}. \tag{3.2}$$

(Fischer & Dallmann, 1991, use y to indicate the spanwise coordinate and z to indicate the wall-normal coordinate. For consistency with the rest of this document, y is the wall-normal coordinate and z is the spanwise coordinate in equations 3.1 and 3.2.) The variable σ is a detuning parameter used to specify a harmonic, subharmonic, or mixed response.

The secondary instability calculations show that maximum temporal amplification occurred at $\alpha = 0.03$ for $\sigma = 0$ (harmonic resonance) and $\alpha = 0.08$ for $\sigma = 0.35$ (combination resonance). The dimensional frequencies of these modes are 73 and 145 Hz, respectively. These frequencies are in the range of the most amplified traveling disturbances obtained by the primary stability analysis. Similarly, the growth rates of the secondary modes ($\omega_i = 0.0063$ and 0.0068, respectively) are commensurate with the primary instability traveling-wave growth rates (although the growth rates computed using the linear code are not valid at 80% chord due to amplitude saturation). The conclusion that can be drawn from these results is that the strong mean-flow distortion produces a spanwise modulation of the traveling-wave intensity. It seems that this effect should not be considered a secondary instability, because the amplified modes exist without mean-flow deformation, and because progressively larger values of the stationary-mode amplitude simply modify the growth rate and frequency of the existing traveling-wave mode. No stable modes are rendered unstable to produce entirely new behavior. What is demonstrated, however, is that the stationary vortices produce strong spanwise modulation of the traveling waves.

An interesting feature of the computations of Fischer & Dallmann (1991) was that they did not identify the high-frequency fluctuations observed by Kohama et al. (1991) in the ASU swept-wing experiment. To resolve this inconsistency, Fischer, Hein & Dallmann (1993) impose a stationary disturbance amplitude larger than that observed in the DLR experiment. They point out that such large amplitudes would clearly be subject to nonlinear interactions, but those interactions could not be considered. Instead, the focus was on determining if the high-frequency instability could be produced under the same linear framework as the previous Fischer & Dallmann (1991) calculations. The new analysis by Fischer et al. (1993) also uses parameters that match the basic state of the Müller

direction and the mode-II instability is generated by inflection points in the *wall-normal* direction. Although one or the other production mechanism may dominate for a particular mode. it is too simplistic to assume that *only* the spanwise or wall-normal inflection points are responsible for the appearance of a particular mode; with such a highly distorted 3-D boundary layer. all possible instabilities must be evaluated.

Malik *et al.* (1996) also compute the secondary instability behavior observed by Poll (1985). The computations for a stationary-wave-dominated boundary layer predict a 17.2-kHz mode; Poll's high-frequency signal occurred at 17.5 kHz. Based on the shape of this disturbance. Malik *et al.* (1996) claim that this is a type-II mode. Calculations were also performed for a traveling-wave-dominated boundary layer. These yielded three high-frequency secondary modes at 15.7, 14.8, and 12.8 kHz.

As part of the ongoing crossflow stability experiment at DLR, Lerche & Bippes (1996) and Lerche (1996) obtain measurements of the high-frequency secondary instability while examining the effect of forcing traveling and stationary crossflow waves. Forcing the most amplified traveling wave is denoted a (1,1) case; forcing the most amplified stationary wave is denoted a (0.1) case. For (1,1) and (0,1) forcing, the distortion of the mean flow alone is not sufficient to render the boundary layer unstable to the secondary instability. The saturation levels of these cases are 2% and 10%, respectively. However, superposition of the stationary and traveling waves can produce sufficient distortion to destabilize the secondary instability. Using phase-locked hotwire measurements, Lerche (1996) observes that the high-frequency secondary instability appears to be linked to a particular phase range of the traveling . wave. Bippes (1999) states that in these cases, the secondary instability is located near the *instantaneous* wall-normal inflection point, $\partial^2 U/\partial y^2$, with the larger velocity gradient $\partial U/\partial y$.[1] where U now represents the basic state plus the primary instability (stationary and traveling) disturbances. Bippes claims that the region of secondary instability activity is not tied to a particular inflection point of the steady flow (either wall-normal or spanwise), but rather is moving in the span direction with the traveling waves induced by the upstream forcing. This is likely the case when traveling waves dominate, but in low-disturbance environments for which stationary waves dominate, the secondary instability does seem to be located at particular span locations.

The fact that for some configurations the superposition of a certain phase range of the traveling crossflow mode with the stationary mode is required to trigger the secondary instability may reveal why some earlier observers (e.g., Poll, 1985) believed the high-frequency hotwire signals to be intermittent turbulence. The result obtained by Lerche (1996) shows this is not the case. The occurrence of the secondary instability is deterministic if one is careful to control both the traveling and stationary waves. It appears that to destabilize the secondary instability. there is a critical amplitude of the streamwise-flow deformation that is necessary. but this deformation need only occur instantaneously. This result should not be surprising if one considers that secondary instability frequencies are much higher than the primary traveling-wave frequencies. What could be considered "instantaneous" with respect to the slow primary-wave time scale is quite long on the secondary instability time scale.

The velocity fluctuation data obtained by Lerche (1996) for the case of (0,1)+(1,1) forcing have the same type of spectral structure as seen by Kohama *et al.* (1991). The secondary instability appears as a broad high-frequency peak an order of magnitude higher (in frequency) than the most amplified mode of the primary instability. For Lerche's case,

---

[1] The DLR group uses z as the wall-normal coordinate. y is used here for consistency with the definition used throughout this document.

becomes unstable and grows slightly less rapidly than the 600-Hz–2.5-kHz mode. Kawakami *et al.* (1999) also use a small speaker embedded in the plate to force the secondary instability. Using various forcing frequencies, the authors find that the maximum growth rate is about three times that of the most amplified primary instability and occurs at 1.5 kHz.

3.2 Experimental approach

What is lacking from the experiments described above is a careful, thorough approach to the secondary instability that can be used to validate the computational models. There are numerous spatial and spectral details that have not been explored that could significantly improve our understanding of the secondary instability, including the beginnings of a predictive understanding into where it will appear and how it causes breakdown. One detail that is particularly interesting is the issue of what secondary instability modes appear and under what conditions. Much of the past work has been hindered by rather broad generalizations of the secondary instability features, the best example of which is the fact that none of the experiments has distinctly demonstrated either the type-I or type-II modes predicted by Malik *et al.* (1996). It is a goal of the present experiment to provide a detailed catalog of secondary instability features that is capable of validating computational models.

The secondary instability experiment is quite simple. The approach is to first establish a spanwise-uniform primary disturbance field and then track the evolution of the fluctuating velocities associated with all of the instability modes that exist in a particular stationary structure. Because Reibert *et al.* (1996) demonstrated that the spanwise uniformity of the primary instability is quite good when periodic leading-edge roughness is used, periodic roughness is applied here at $x/c = 0.0025$, near the crossflow neutral point. Because of the uniformity, only a single stationary structure need be interrogated for each case and its behavior is taken to be representative of the behavior of the entire boundary layer. Following the notation used by Reibert *et al.* (1996) and Saric *et al.* (1998), the artificial roughness arrays will be designated with the notation $[k|\lambda]$, where k is the amplitude of the roughness in micrometers and λ is the spanwise wavelength in millimeters.

Measurements are taken by performing the full-field scans that were described previously to obtain the mean and fluctuating velocities at all points in a 2-D grid in the (Y, z) plane at various chord locations, x/c. The mean-flow data are used to determine the stationary-mode amplitude growth. This is done by considering the spanwise rms of the stationary disturbance, $\text{rms}[(U - U_{\text{mean}})/U_{\text{edge}}]$. The amplitude of the stationary-disturbance mode is represented by the integral of the mode-amplitude curve taken from the surface, $Y = 0$, to the edge of the boundary layer. This measure is convenient and robust for experimental data both because it includes the contribution of all the data and thus is resistant to errors at individual points and because there is no ambiguity that results from arbitrary definitions such as a point in the flow at which to evaluate the amplitude. The fluctuating data are processed using a fast Fourier transform to yield fluctuation spectra, and a narrow band-pass filter is applied to these spectra to yield rms velocity-fluctuation amplitudes for individual modes. To obtain the instability growth rates, an integration over the whole field is required rather than an amplitude maximum or the amplitude at a particular location. Without considering changes in the spatial extent of an instability mode, much of the growth in its energy content could be lost as more of the area participates. As will be apparent below, the spatial distributions of the modes vary through the boundary layer, so to obtain an accurate picture of the instability growth rates, the velocity-fluctuation amplitudes are integrated over the entire field to give the total mode amplitudes. Because the stationary

accompanies the advent of nonlinearities. Reibert *et al.* (1996) explain that the upper lobe is due to the rollover phenomenon that brings low-momentum fluid into the upper part of the boundary layer above the high-momentum fluid that is drawn close to the surface. Using the mean-flow velocity profiles from Figure 23, a velocity contour plot is constructed. This plot is shown in Figure 24. This layout reveals the structure of the stationary vortex better than the collection of profiles. In this figure the streamwise flow is into the page and the crossflow velocity is from right to left. The stationary vortex rotates in the clockwise direction. The dark shades are low-momentum regions and the light shades are high-momentum regions. The low-momentum upwelling region falls between $z = 121$ and $123\,\mathrm{mm}$. What is particularly important for understanding the breakdown of the boundary layer is the distribution of velocity fluctuations within this structure. Figures 25–27 show the velocity-fluctuation spectra at points on three vertical (constant z) lines. The first of these, Figure 25, is at $z = 119\,\mathrm{mm}$, to the left of the low-momentum upwelling. The spectra here show extremely low fluctuation levels. However, several features are detected. First, the most amplified disturbances are between 150 and 200 Hz. These fluctuations are the most amplified traveling crossflow waves. Second, there are fluctuations near 800 Hz. These may be T–S fluctuations that exist in spite of the favorable pressure gradient, since 800 Hz corresponds to about $F = 140$. All of the fluctuations die off quickly as the distance from the wall increases. For $z = 122\,\mathrm{mm}$ (Figure 26), the center of the low-momentum upwelling region, the spectra are about the same as at $z = 119\,\mathrm{mm}$, except now the disturbances exist much farther from the wall where the boundary layer is thicker. The final span location, $z = 125\,\mathrm{mm}$, with spectra shown in Figure 27, is what is referred to as the overturning region. This is where the low-momentum fluid that has been lifted away from the wall moves over the high-momentum fluid that is drawn in toward the wall. For this chord station, the spectra are very similar to those in the upwelling region of the previous figure.

The best means of understanding the stability behavior in the distorted boundary layer is to plot the spatial distribution of the amplitudes of the various fluctuating modes and compare these to the underlying structure of the mean flow at the same location. To do this, all of the velocity-fluctuation spectra for a particular chord location are integrated over the frequency band of interest, and the result is plotted against Y and z in a manner similar to the mean-flow contours. In the velocity-fluctuation amplitude-distribution figures, the intensity is given as the rms velocity fluctuation in the frequency band, the square root of the integral of the spectrum. Figure 28 is the rms velocity-fluctuation distribution for the frequency band centered at 200 Hz, the frequency band corresponding to the traveling crossflow mode. Before the boundary layer undergoes mean-flow modification because of the stationary crossflow vortices, the traveling crossflow waves are uniform in span. Here, the mean-flow modification has produced some deformation of the traveling crossflow amplitude distribution. This is the effect termed a secondary instability by Fischer & Dallmann (1991), who predicted that just such a modification should exist. As was argued above, this should not be considered an absolute instability because it is only a modification of existing unstable modes and not a destabilization of a new mode.

It is not obvious that this experiment should be capable of detecting the traveling crossflow fluctuations as well as we see them here. The primary disturbance consists of streamwise vorticity and the velocity fluctuations associated with this are v', w'. The hotwire is situated to detect u', v' fluctuations. Furthermore, because the streamwise U component is large relative to the fluctuations, the hotwire is more capable of detecting the u' fluctuations that are aligned with U than the v' fluctuations that simply change the velocity vector's direction, but don't significantly change its amplitude. The fluctuating velocity detected by

that lie in the (Y, z) plane and convect in the stream direction. If this is the case, a visualization of the secondary instability would consist of rolls that wrap along the left side of and extend above the stationary structure. This is exactly what is observed in the rotating disk flow-visualization experiments of Kohama (1984). In the secondary instability phase of the Görtler experiment carried out by Swearingen & Blackwelder (1987), two types of secondary instability modes were observed. One is termed a horseshoe mode and resembles the crossflow rolls observed by Kohama (1984). The other mode is termed a sinuous mode and consists of an oscillation of the structure in the span direction. The difference between the crossflow and Görtler boundary layers is the fact that while crossflow boundary layers appear to have only a single secondary instability location, the Görtler structure has symmetric instability lobes that can operate either in or out of phase to produce one or the other type of secondary instability. Because there is no such symmetry in crossflow boundary layers, only the horseshoe-type mode can exist. This is exactly what is observed by Kohama (1984) and is what is thought to exist here.

The distribution of 200-Hz fluctuations continues to diverge from what is expected for traveling crossflow waves. Now there is almost no significant activity in this band in the high-velocity regions that are being drawn into the surface by the stationary vortex, and the fluctuations that were once distributed along the surface as the traveling crossflow waves are being lifted by the vortex in the low-momentum upwelling region. It is very surprising that a mode whose origin is in spanwise-traveling waves could reach a stationary state that is so highly modulated in span. The behavior of this mode is certainly worthy of much more detailed attention. However, to do it justice would require a different technique than is used here. Because it is (or at least starts as) a v', w' disturbance, if one wishes to understand its evolution unambiguously, a multi-element hotwire probe should be used to obtain the projection of the velocity field onto the plane parallel to the wing instead of simply the projection onto the single-element wire used here. With the data that are available now, nothing more conclusive can be said about this mode. This does not prevent us from moving forward with the high-frequency mode that appears here at $x/c = 0.40$. Because this mode lies along a streamwise shear layer, the disturbances are u', w' (or u', v', depending on the particular location being considered), so the single hotwire is sufficient to obtain good data on this mode.

Moving downstream, the next position considered is $x/c = 0.41$. The mean-flow contours, velocity-fluctuation spectra, and the rms velocity distributions are nearly identical to those at $x/c = 0.40$, except of course for growth of the fluctuation amplitudes. Figures 43–47 are the mean-flow profiles; mean-flow contours; and fluctuation spectra at $z = 87, 90$, and 93 mm, respectively.

At $x/c = 0.42$, the mean flow (profiles and contours are given in Figures 48 and 49) is again about the same, but here a subtle difference in some of the fluctuation spectra (Figures 50–52) exists. Close examination of the $Y = 0.80$ mm spectrum at $z = 84$ mm (Figure 50) and the $Y = 1.60$ mm spectrum at $z = 87$ mm (Figure 51) reveals that a second peak in the fluctuation spectra exists at about 1.8 kHz. It is easy to miss the existence of this peak because of the proximity of the mode-I peak at 3.0 kHz. Plotting the rms velocity from 1.7–1.9 kHz (Figure 53) reveals an amplitude distribution that is almost identical to that seen previously for the mode-I instability. It is easy to imagine that much of this similarity is due to spillover from the 3.0-kHz mode. Consider, for instance, the $Y = 2.4$ mm spectrum at $z = 87$ mm (the highest amplitude secondary instability peak in Figure 51). That feature of the spectrum is quite strong at 1.8 kHz, and yet it appears to have only a single mode centered near 3 kHz. If there is 1.8-kHz activity here it is swamped

are not markedly different. but the contour map constructed from them (Figure 74) shows that much of the fine structure of the mean flow has been eliminated. The low-momentum upwelling no longer has a narrow apex: instead this region is wider and flatter. The region of low-momentum fluid high in the boundary layer still extends over nearly the whole stationary structure's length, but now the lowest velocities in this feature, $U < 0.7\,U_{edge}$, are gone. What is most important in Figure 74, however, is the velocity gradient near the wall to the left of the low-momentum upwelling. Notice that this region looks quite different from previous cases: in particular the contour lines are now very close together. indicating that the wall shear here is quite high.

What are responsible for these changes in the mean flow are of course the much-increased velocity fluctuations brought on by breakdown to turbulence. At $z = 72$ mm, the high wall-shear region to the left of the low-momentum upwelling, the fluctuation spectra in Figure 75 show a flat. very high amplitude, fully turbulent spectrum at $Y = 0.8$ mm. the position in the figure closest to the wall. The spectra higher in the boundary layer are nearly fully turbulent. but in these curves some evidence of the 3.0-kHz mode remains. The situation is much the same for $z = 75$ mm (Figure 76), the low-momentum upwelling position, except the spectrum of the point closest to the wall shows a somewhat lower fluctuation level. especially beyond 2 kHz. This position is below the zone affected by the secondary instabilities at the upstream stations and below the traveling crossflow fluctuations that persist throughout the preceding development. just as they appeared in Figure 41. The spectra for $z = 78$ mm that are shown in Figure 77 are not turbulent; they maintain distinct spectral features associated with traveling crossflow fluctuations near 200 Hz and the 3.0-kHz mode-I secondary instability despite their very high amplitude.

In Figure 78 the distribution of the *total* velocity-fluctuation rms amplitude is plotted. It is evident from this figure that the overall energy distribution is exactly coincident with the 3.0-kHz and 6.1-kHz modes. Their rapid growth just prior to breakdown and the spatial location of the subsequent turbulent fluctuation maximum make it quite obvious that the secondary instability is the route to breakdown for this flow. Notice that the total rms velocity-fluctuation distribution shows somewhat more activity close to the wall between $z = 71$ and 73 mm than do the 3.0-kHz distributions upstream. This has an important consequence in that it helps to explain the high wall shear in this region: the turbulent fluctuations promote enhanced mixing of the high-momentum fluid with the low-momentum fluid near the wall. resulting in increased shear. As a result, the behavior of the turbulent wedges that indicate breakdown in naphthalene flow-visualization experiments is now clear. The upstream tips of the wedges appear at the points where the mode-I instability makes its closest approach to the wall on the left side of the low-momentum upwelling location. The reason the wedges appear as they do. with the breakdown tip on the left edge of the low-shear part of the naphthalene streaks, has been a subject of some interest since the first systematic swept-wing flow-visualization experiments were undertaken by Dagenhart (1992). Understanding the location and amplitude of boundary-layer features relative to the associated wall shear in this manner is essential if one is to conduct an experiment using only wall measurements with hot films or some other technique as would be required in a flight experiment. In particular. consider the quantitative transition-detection technique developed by Chapman *et al.* (1998) using hot films. In this approach the hot films are aligned in an array along a particular stationary structure and must be positioned within the structure to detect the secondary instability fluctuations and the high shear of the turbulent wedge. With the data presented here it is now possible to correctly place the sensors to achieve optimum performance with this technique.

40

a weaker early mode and the strongly amplified mode that becomes unstable at $x/c = 0.42$. This may indeed be the case, but if so it would be difficult or impossible to detect experimentally because the 3.0-kHz fluctuations are always observed at exactly the same spatial location, regardless of the chord location. The 6.1-kHz mode is first detected at $x/c = 0.43$ and it undergoes even more rapid growth than the 3.0-kHz mode. What is interesting about the growth rates of the two high-frequency modes is that the 6.1-kHz mode *is not* twice that of the 3.0-kHz mode, meaning that the 6.1-kHz mode is not simply a harmonic of the 3.0-kHz mode, despite the fact that they are spatially coincident. Rather, it appears that the 3.0-kHz and 6.1-kHz modes are distinct.

3.3.2 Increased roughness amplitude case

With a fairly complete description of the secondary instability for the baseline case of $Re_c = 2.4 \times 10^6$ with [18|12] roughness, we wish to understand the effect of the roughness-array amplitude on the appearance of the secondary instability. The results of Reibert *et al.* (1996) show that if the stationary crossflow waves saturate, then the transition location is nearly independent of the roughness amplitude. Those authors observed that changing from [6|12] to [48|12] roughness moved the transition location from $x/c = 0.49$ to only $x/c = 0.52$ at $Re_c = 2.4 \times 10^6$. This result suggests that because the stationary crossflow disturbances were saturated by $x/c = 0.40$ in the previous section, an increase in the roughness amplitude will not change the stationary-mode amplitude in the transition region. Essentially, one could expect that if the gross transition behavior is unchanged, the secondary instability is unchanged as well.

One aspect of the higher amplitude roughness case that will be different from the baseline is the amplitude of the stationary-mode harmonics. Nonlinearities in the development of the mean-flow field are not just responsible for saturation, they also generate harmonics of the stationary mode. So if 12-mm input waves are applied, 12-mm waves are observed to dominate the flow field, but sufficiently far downstream, 6-mm, 4-mm, etc. waves are observed to grow as well, and these grow even after the principal wave has saturated.

For this second case with [54|12] roughness, the boundary-layer velocity profiles will not be shown; instead only the contour plots will give mean-flow information because the contours are better at describing the mean-flow modification. The stationary-mode amplitudes are calculated in the same manner as before using the integration of the rms stationary profile. The stationary boundary-layer structure that is followed for the [54|12] case saturates somewhat earlier than the structure that is followed for the [18|12] case, so the measurements begin at $x/c = 0.25$. Here the mean flow shown in Figure 88 is distorted but has not yet developed a distinct overturning feature. Spectra at $z = 118.6$, 122.2, and 125.8 mm (Figures 89–91) are very similar to what was seen in the upstream stations for the previous case. They indicate low disturbance amplitudes with activity confined to the traveling crossflow frequency band. The stationary structure has developed the overlap feature at $x/c = 0.30$ (Figure 92), and the spectra show much higher amplitude fluctuations near 200 Hz (Figures 93–95). The spatial distribution of the 200-Hz fluctuations shown in Figure 96 is very similar to the type of distribution seen earlier.

At $x/c = 0.33$, there is still no secondary instability activity in the spectra, so the mean flow and spectra are not shown. At $x/c = 0.34$, there is the first indication of secondary instability activity near 3.0 kHz. The mean-flow velocity contours for this location are shown in Figure 97 and representative spectra are given in Figures 98–100. The distributions of 200-Hz and 3.0-kHz fluctuations are shown in Figures 101 and 102, respectively. Despite

the mean-flow velocity has already lost much of its structure high in the boundary layer and the shear is increased to the left of the low-momentum upwelling as it was in the baseline case. The velocity-fluctuation spectra given in Figures 118–120 are not as dramatic as the spectra that indicated breakdown for the baseline [18|12] case, but the mode-I and the mode-II secondary instabilities have actually decreased, and lacking a more clear indication, we take this as the breakdown criteria in this case. What is new here is that following breakdown, the total rms velocity fluctuations that are shown in Figure 121 are coincident with the location of 200-Hz activity and not with either of the secondary instability modes. This suggests that although the secondary instability growth is obviously a major factor in triggering breakdown, for the increased roughness amplitude case, we cannot ignore the contribution of the lower frequency fluctuations.

The growth rates of the stationary crossflow vortex, the 200-Hz mode, and the 3.0-kHz mode are shown in Figure 122. The 6.1-kHz mode is not shown both because it never appears as a distinct mode and also because its amplitude is so low that the amplitude integration would include a significant contribution from the background. The 200-Hz mode grows throughout the entire boundary layer, with a growth rate that does not change nearly as much as one might expect given the dramatic variations that occur in the underlying mean flow. The 3.0-kHz mode-I instability has a lower growth rate here than was observed in the baseline case. It is not known whether this is a consequence of the growth being observed upstream of the baseline case or whether it is a purely local effect that only depends on the details of the stationary structure. The overall growth from where the mode can be detected until breakdown is much lower than for the baseline case, but here we believe that the lower frequency fluctuations are jointly responsible for breakdown, and this would mean that the secondary instability need not reach as high an amplitude before transition occurs.

The stationary-mode growth curve displays a notched appearance, that is, growth and saturation followed by a slight decrease in amplitude, then slightly more growth before breakdown. Although it is more obvious here, the same phenomenon occurs for the baseline case (Figure 87). This behavior was observed by Reibert *et al.* (1996), who performed similar mean-flow measurements over many wavelengths on another model. It would appear that this is a real effect and cannot be dismissed as experimental error. In Reibert *et al.*'s experiments, this phenomenon was observed for [18|12] and [48|12] roughness but not for [6|12] roughness. Here we observe the same phenomenon; higher-amplitude leading-edge roughness leads to a more pronounced two-stage saturation. Although the mechanism is not clear, the effect of roughness amplitude suggests that larger-amplitude harmonics of the dominant stationary wave, increased low-frequency fluctuation amplitudes, or a combination of both of these is responsible. One possible scenario is that downstream of saturation of the dominant wave, its harmonics continue to grow, but at too low an amplitude to be detected immediately. Saturation of the largest-amplitude harmonic gives the second saturation plateau observed in the overall mode amplitude curve. The effect would clearly be more pronounced for large roughness amplitudes that provide earlier saturation and higher-amplitude harmonics.

3.3.3 Decreased Reynolds number case

We now move to the case of [48|12] roughness with $Re_c = 2.0 \times 10^6$. This will demonstrate what effect slightly subcritical forcing has on the secondary instability and breakdown, because the lower Reynolds number means that the most amplified stationary wavelength is shorter than 12 mm. The lower Reynolds number will produce transition at a larger

secondary instability is first detected. What is immediately apparent from the mean-flow contour plot (Figure 155) is that short wavelength harmonics of the 12-mm mode are quite important here. To the left of the low-momentum upwelling that is centered at $z = 85\,\mathrm{mm}$, there is a distinct plateau where there is not a strong $\partial U/\partial z$ gradient. The mean-flow contours immediately suggest that the mode-I instability will not be as important in this case as in the previous cases because the region in which it is most strongly amplified has been reduced. Instead the type-II mode may play a more important role.

Velocity-fluctuation spectra for $x/c = 0.30$ are given in Figures 156–159 for $z = 80.2$, 82.6, 85.0, and $87.4\,\mathrm{mm}$. Four stations are used here instead of the three that are used above because of the more complex stationary structure. In all of these, a broad, high-amplitude band centered at 300 Hz is amplified. The very low amplitude secondary instability is just visible at $z = 85.0\,\mathrm{mm}$, directly above the low-momentum upwelling center. For this $Re_c = 2.8 \times 10^6$ case, 300 Hz is representative of the most amplified traveling crossflow wave and 3.6 kHz is representative of the mode-I instability. Distributions of these two modes are given in Figures 160 and 161, respectively. The 300-Hz mode is somewhat different from the shapes that occur for critical- and subcritical-wavelength forcing; here there are distinct maxima within the structure. The highest fluctuation amplitudes occur just to the right of the low-momentum upwelling region as in the previous cases, but the region near the wall to the left of the upwelling also contains significant low-frequency fluctuations, as does the upper part of the overturning region. Although the highest amplitude part of the structure occurs in roughly the same span position as in previous cases, it is somewhat lower in the boundary layer and elongated in span. The 3.6-kHz mode is barely detectable over the background fluctuations, but it can be identified as a type-I mode based on its location within the stationary structure.

Several stations downstream at $x/c = 0.35$, the mean flow (Figure 162) has a character similar to the mean flow at $x/c = 0.30$. The representative spectra at $z = 66$, 68, 70, and 72 mm (Figures 163–166) indicate that while the secondary instability has grown significantly, it does not exist as close to the wing on the left side of the stationary structure as it does in other cases that do not feature supercritical roughness forcing. The minor lobes of the 300-Hz mode (Figure 167) have disappeared by this station, but the mode retains the elongated shape it demonstrated at $x/c = 0.30$. Figure 168 confirms that the 3.6-kHz mode is not close to the wall and is in fact creeping along the stationary structure into the region occupied by the type-II instability. Previously, the behavior was the opposite. A type-II mode might be observed early, but it would tend to shift down into the mode-I region. The type-II mode is apparent in Figure 169.

Moving to $x/c = 0.37$, the mean-flow contours are given in Figure 170. The most interesting feature of this location is that the spectra (Figures 171–174) show that above the overturning region, the center of mode-II activity, the 6.5-kHz type-II mode is of nearly equal amplitude to the 3.6-kHz type-I mode, despite having started growing farther downstream. Mode II is more highly amplified, so this case appears to conform to the expectation that supercritical forcing can suppress the mode-I instability in favor of the mode-II instability. The 3.6-kHz and 6.5-kHz fluctuation distributions are given in Figures 175 and 176, respectively.

Breakdown is observed at $x/c = 0.385$. The mean-flow contours shown in Figure 177 do not appear markedly different; only the spectra above the low-momentum upwelling appear to have undergone breakdown. Figures 178–181 show that there is mode-I activity to the far left of the center of the vortex at $z = 58\,\mathrm{mm}$, that breakdown has occurred in the overlap region between the type-I and low-frequency modes, and that mode-I and mode-II activity

46

imum amplitude available in the facility. 125 dB. At frequencies above 2.8 kHz, the sound amplitude decreased significantly due to the capability of the speakers (woofers designed for frequencies in the hundreds of Hertz). For the entire range of secondary instability frequencies, no change in the boundary-layer velocity-fluctuation spectrum was observed at any position within the stationary-vortex structure at the 39% chord position. The second test is conducted at $Re_c = 2.0 \times 10^6$, $x/c = 0.55$, $z = 88$ mm (see Figures 141 and 146). These conditions are better than in the previous case because the mode-I secondary instability is centered near 2.4 kHz, within the capability of the speakers, and because the maximum amplitude of the secondary instability is much greater than the surrounding frequency band, so the spectral signal is unambiguous. However, as with the higher Reynolds number case, maximum-amplitude acoustic input from 1.5–3.0 kHz had no discernible effect on the boundary layer.

To assess the effect of freestream turbulence on the secondary instability, a small turbulence-generating grid is positioned in the contraction cone upstream of the test section. The grid produces u'_{rms}/U_∞ as high as 0.0029, high enough that traveling-wave-dominated flow might result. Spectra of the u' are flat up to about 800 Hz and roll off thereafter, reaching a minimum by 4 kHz. Tests at all three chord Reynolds numbers are performed with the turbulence grid in place. In all cases the traveling waves are enhanced, but in no case does the transition behavior change, and no changes are detected in the behavior of the secondary instability. The fundamental problem with this approach is the problem of applying high-frequency turbulence without also inducing the low-frequency content that will produce overwhelmingly large traveling primary crossflow waves.

These tests underscore a fundamental difficulty associated with boundary-layer stability experiments. One must always consider the mode of receptivity when attempting a controlled means of forcing an instability. For secondary instabilities, the problem is even more pronounced. Here, the receptivity encompasses both the initial entrainment of the freestream disturbance of the desired frequency and the subsequent evolution of that mode until the secondary instability becomes amplified.

quires choosing contours in the complex ω- and k-planes that maintain causality (i.e.. no response for $t < 0$) and properly treat singularities introduced by the dispersion relation.

specifically to investigate absolute instability behavior, Lingwood (1996) traced the evolution of transiently forced disturbances and showed that the radial group velocity does indeed go to zero with positive temporal growth and cause transition.

The rotating disk result is quite convincing, but the extension to swept wings is not as direct as might be imagined. Although each geometry is a 3-D crossflow boundary layer, the axial symmetry of the rotating disk means that one need only consider whether the *radial* group velocity goes to zero, because any disturbance that exists at a fixed radius will spread in the circumferential direction and contaminate an entire radial band. On swept wings, there is no such symmetry, so if the disturbance velocity goes to zero in only one direction the disturbance will still convect in the other direction, leaving the initial position disturbance free. Thus what could be thought of as an absolute instability of one direction is not sufficient for a true absolute instability. An extension of Briggs' method to the swept-wing boundary layer requires *simultaneous* pinching of the contours in both the streamwise- and crossflow-wavenumber planes.

The difficulty of achieving such simultaneous pinching is acknowledged by Lingwood (1997). She applies the generalized approach to an FSC boundary layer to determine whether swept-wing-type flows can support an absolute instability despite the more stringent criteria. The FSC geometry is a closer approximation to the swept wing than the rotating disk because it provides for pressure gradient and sweep and because it does not possess the symmetry inherent to the rotating disk. However, the FSC configuration retains an advantageous feature of the rotating disk: a similarity solution for the mean flow exists, making parametric studies relatively easy. Lingwood finds that a pinch point does exist for the chordwise wavenumber plane for very strong favorable pressure gradients ($\beta_H = 1.0$, i.e. near the attachment line) and high sweep angles (greater than 80°), but no simultaneous spanwise pinching is observed. Thus a true linear absolute instability does not exist for FSC boundary layers, and furthermore, the parameter range for which a single direction becomes nonconvective is quite restricted.

Lingwood's approach was extended by Taylor & Peake (1998), who consider both FSC and true swept-wing configurations. These authors determine that the parameter range that supports single-direction pinch points is larger than the region identified by Lingwood (1997), but despite this, the flow still does not support an absolute instability. Taylor & Peake (1999) make yet another extension to compressible FSC and swept-wing flows and still find no absolute instabilities. For these more realistic configurations, even the attachment-line region identified by Lingwood (1997) is not absolutely unstable.

A critical feature that is not considered by any of these computations is that stationary crossflow waves on the swept wing render the disturbance evolution highly nonlinear. The modification of the mean-flow basic state means that the velocity profiles considered by Lingwood (1997) and Taylor & Peake (1998, 1999) do not represent what actually exists in the boundary layer near the transition location. In light of the saturation data of Reibert *et al.* (1996), it is conceivable that although the nondeformed linear basic state does not support an absolute instability, the highly modified nonlinear boundary layer does. It is with this possibility in mind that a transient forcing experiment is performed as part of the current swept-wing transition program.

4.3 Experimental approach

The most robust experimental means of determining whether an absolute instability exists is to apply a transient initial disturbance and observe the spatial and temporal evolution of

be expected and for which the hotwire will be far enough from the surface that it can be moved without danger of hitting the surface. The hotwire is stationary at each point while the velocity data are obtained, and following each point the traverse is moved in the positive span direction, z, and adjusted in Y to maintain the correct offset from the local wing surface. Following a complete run along the span, the hotwire is returned to the starting position, the pressure input to the variable-roughness insert is adjusted, and the next run is begun.

Several aspects of the experimental data are most revealing. The basic output of the experiment is the mean flow, U/U_{edge}, as a function of the span, z. For each Reynolds number and chord station considered, these curves are presented for an initial inactive-roughness case, an active-roughness case, and a second inactive-roughness case. The three states are acquired sequentially during a single, continuous wind-tunnel run. If the second inactive case is the same as the first, the boundary layer does not support an absolute instability. If the second inactive case is somehow fundamentally different from the first, then there is reason to believe that an absolute instability *may* be present in the boundary layer.[1] It is useful to observe the behavior of the stationary crossflow modes by calculating the spatial (spanwise) mean-flow power spectra. For each Reynolds number, at least two chord locations are considered and the behavior of the stationary modes (i.e., growing, saturated, or dissipating due to turbulent fluctuations) helps to demonstrate the laminar or turbulent state of the particular cases. Another means of understanding the flow is gained by examining the spanwise distribution of the fluctuating-velocity power at the most amplified frequency of the secondary instability. In the previous chapter it was observed that this amplitude grows by many orders of magnitude through transition, so the high-frequency fluctuations provide a more sensitive indication of the state of transition than the mean flow. Moreover, the results of the previous chapter provide a means of evaluating what is represented by the various high-frequency fluctuations. Finally, velocity-fluctuation spectra at particular locations are provided as another means of indicating the laminar, transitional, or turbulent state of the boundary layer.

4.4   Results and discussion

4.4.1   Baseline case

For the baseline case of $Re_c = 2.4 \times 10^6$, the two most revealing measurement stations are at $x/c = 0.43$ and $x/c = 0.45$. However, to place the results at those locations in context, it is useful to first examine results from $x/c = 0.40$, a (nearly) purely laminar case for both active and inactive leading-edge roughness. Figure 184 shows the mean flow at $x/c = 0.40$ and $Y = 1.5\,\mathrm{mm}$. It is evident in this figure that although the active-roughness case has larger-amplitude mean-flow deformation, the inactive-roughness case shows significant deformation as well. The spatial power spectra of these spanwise mean-flow data (Figure 185) reveal that in the active-roughness case nearly all the stationary disturbance power is concentrated in the 12-mm mode, with some growth of the 6- and 4-mm harmonics. These spectra are generated from 128 span locations as shown in Figure 184. The original data are spaced at 1-mm increments of z. For the inactive roughness, there is a broader but much lower amplitude distribution of stationary-disturbance power centered about the most amplified

---

[1] If an absolute instability is suspected based on the initial experiments, a more convincing set of experiments is required. These would consist of point-by-point phase-locked averaging over many forcing cycles to reconstruct the disturbance velocities throughout the boundary layer.

secondary instability activity just prior to the end of breakdown. The inactive-roughness case appears fully laminar without any signs of secondary instability growth. At $z = 46\,\text{mm}$ (Figure 191), the onset of breakdown in the active case is farther upstream than it is for the structure at $z = 31\,\text{mm}$, because at $z = 46\,\text{mm}$, active roughness produces fully turbulent flow. At $z = 66\,\text{mm}$, the center of the turbulent wedge (Figure 192), the active-roughness case is indeed turbulent, but the inactive case is still in the midst of secondary instability growth as evident from the distinct bands of mode-I and mode-II activity in the velocity-fluctuation spectrum. It is somewhat surprising that the behavior produced by the two roughness configurations is different here. One might expect that whatever feature inherent to the roughness device that produces the wedge would be sufficient to cause earlier transition regardless of the amplitude of the periodic disturbances on which it is superposed. However, the breakdown of the feature generated by the isolated roughness does depend on the background periodic disturbance. The details of the primary instability interaction between a large amplitude isolated feature and a lower-amplitude periodic field have not been investigated, and this may represent an important topic for further study. It is easy to imagine that on an actual aircraft employing subcritically spaced roughness arrays to suppress crossflow transition, such isolated features would be plentiful, and it is unclear what the resulting behavior would be and whether isolated roughness elements could prevent such a system from working.

Moving finally to $z = 108\,\text{mm}$ (Figure 193), the spectra associated with the inactive-roughness amplitude peak contain the early stages of the mode-I secondary instability growth and the active-roughness case is fully turbulent. Taken together, the spanwise mean flow (Figures 186 and 187), the 3-kHz fluctuation curves (Figure 188), and the individual point spectra (Figures 189–193) show that the instabilities present can be fully understood in terms of secondary instability growth, and that there is no indication of an absolute instability.

At the third chord location for $Re_c = 2.4 \times 10^6$, $x/c = 0.45$, the now fully turbulent active-roughness case exhibits significantly lower spanwise mean-flow variations because of the continuing turbulent dissipation of the crossflow vortices. The amplitude of the variations in Figure 194 is visibly reduced relative to the upstream locations, and the spatial spectra in Figure 195 confirm this. Even the minimum in the mean-flow velocity associated with the turbulent wedge has disappeared. The data that are obtained prior to and following the turbulent active-roughness case are again nearly identical. There is no hysteresis and no absolute instability. The distributions of 3.0-kHz velocity-fluctuation power in Figure 196 show that the active-roughness case consists of fully turbulent flow. The inactive cases remain almost entirely laminar, except for the turbulent wedge that has grown to cover approximately 24 mm of the span.

For this chord station, the most interesting fluctuation spectra are obtained at $z = 60\,\text{mm}$ and $z = 102\,\text{mm}$. At $z = 60\,\text{mm}$ (Figure 197), the wedge is now turbulent for the inactive case, with some remnant of the mode-I secondary instability still visible. The active case is turbulent as it was at the upstream station. At $z = 102\,\text{mm}$ (Figure 198), the active-roughness case remains turbulent but here the secondary instability is strongly amplified in the inactive case. So overall, the $x/c = 0.45$ data confirm that the instabilities driving transition are convective.

the spatial spectra of the mean-flow curves are given in Figure 209, and the distributions of 2.0-kHz mode-I fluctuations are given in Figure 210. No hysteresis is detected in any of these curves. The spatial spectra show that the dominant crossflow wavelength with zero-amplitude artificial roughness is about 13.5 mm. This station exhibits the widest band of amplified wavelengths of any examined thus far. The band of amplified fundamental wavelengths extends from 19.5 mm to 8.8 mm and both its first and second harmonics are visible. The active-roughness case is much more regular in span, and it has lower-amplitude mean-flow variations.

One consequence of the irregularity of the disturbance field is that the individual point spectra in Figures 211–214 exhibit a variety of behaviors. Even though the active-roughness case has a much higher fluctuation level across the span, the inactive cases actually break down near $z = 16$ mm (Figure 211) where the active-roughness case does not. Furthermore, the active-roughness fluctuations at $z = 16$ mm are centered at 3.0 kHz, not 2.0 kHz, as are the highest-amplitude inactive-roughness fluctuations. This may represent behavior nearly along the lines of that observed by Saric et al. (1998), who used subcritically spaced roughness arrays to suppress transition. The active case is not sufficient to prevent transition in general, however. At $z = 53$ mm (Figure 212), the active-roughness case is fully turbulent while the inactive-roughness case has almost zero disturbance amplitude, as it does over most of the span.

Because peaks at both 2.0 kHz and 3.0 kHz are observed for $x/c = 0.58$, the distributions of 3.0-kHz fluctuations are given in Figure 215 to supplement the 2.0-kHz fluctuation distribution plots given in Figure 210. The 3.0-kHz mode is nearly identical to the 2.0-kHz mode. Both are active across the span for the active-roughness case, but they only appear at high amplitudes near $z = 16$ mm for the inactive-roughness case.

The final absolute instability test is performed at $x/c = 0.60$. The mean flow for this case is given in Figure 216. There is no change in behavior of the inactive-roughness cases, so there is no absolute instability. In Figure 217, the spanwise spectra of the inactive-roughness cases indicate that the flow there has undergone amplitude saturation: the peak of the most amplified mode is unchanged from $x/c = 0.58$. The active-case spectrum indicates that the forced stationary wave is dissipating due to the higher fluctuation levels. Figures 218 and 219 show that the fluctuations are still growing for the active case and the high-amplitude peak in the inactive cases, but that across most of the span, the inactive case remains free of high-frequency disturbances.

So for three cases on the ASU(67)-0315 wing, $Re_c = 2.4 \times 10^6$, $Re_c = 2.8 \times 10^6$, and $Re_c = 2.0 \times 10^6$, the data show that there is no evidence of an absolute instability prior to breakdown of the crossflow boundary layer. Moreover, in every case, the behavior of both the stationary mode and the high-frequency fluctuations may be understood in terms of secondary instability growth. Breakdown appears to be driven by that mechanism.

wall at the farthest point from the stationary vortex center to above the low-momentum upwelling center. The secondary instability can be imagined as wrapping around the outside of this portion of the stationary vortex. This is the behavior shown very clearly in the rotating disk flow visualizations of Kohama (1984, 1985). In nearly all circumstances, the lowest-frequency secondary instability is type I and is the largest amplitude secondary instability mode that is detected. In many instances, one or more higher-frequency type-I modes coexist in the same location. These are observed at close to integer multiples of the lowest-frequency type-I mode.

Although instability modes at integer multiples at the same spatial location strongly suggest harmonics of the dominant mode, the growth rates do not always support this. In the baseline case, the growth rates of the fundamental 3.0-kHz type-I mode and the 6.1-kHz type-I mode have nearly equal growth rates. The 6.1-kHz mode would be expected to have twice the growth rate of the fundamental were it a harmonic. However, growth rates are more easily obtained for the $Re_c = 2.0 \times 10^6$, [54|12] roughness case, and here the growth rate of the 4.9-kHz multiple of the 2.4-kHz fundamental type-I mode is about twice as large. For the same case, a 7.5-kHz type-I mode was observed as well, and the spectra show that even higher multiples exist. The other cases do not provide sufficiently good data to obtain reliable higher-frequency-mode growth-rate comparisons. In light of the limited and conflicting data, it is unclear whether these are harmonics that we cannot measure accurately, or whether they are distinct modes. In any case, these results show that to properly understand the breakdown region in as much detail as possible, narrow frequency bands should be investigated separately. As many as five or more instability modes exist in some cases, so tracking the behavior of bands as wide as a kilohertz or more can lump the behavior of many modes into a single result.

In one instance, $Re_c = 2.4 \times 10^6$ with [18|12] roughness, a high-frequency mode of lower frequency than the most amplified type-I mode was identified. This mode existed closer to the wall than the typical type-I shape, and it may play a role in triggering breakdown where the type-I mode makes its closest approach to the wall. This mode was not identified in any other case and was difficult to separate from the higher-amplitude 3.0-kHz mode.

The second type of secondary instability mode, termed a type-II mode, was observed much less frequently than the type-I modes. This mode exists high in the boundary layer above and somewhat outboard of the low-momentum upwelling center. This instability is of the Kelvin–Helmholtz class, as is the type-I mode, but the type-II mode exists in the *wall-normal* shear layer of the streamwise flow. The type-II mode occurs at about twice the frequency of the highest-amplitude type-I mode. It is often overwhelmed by the growth of the (possible) harmonic of the type-I mode and is therefore extremely difficult to track experimentally. One exception is the supercritical forcing case, $Re_c = 2.8 \times 10^6$ with [54|12] roughness. For this configuration, the spanwise shear region is reduced and the type-I modes do not reach the amplitude they do under more favorable conditions. In this environment, the type-II mode is detected more easily and plays an important part in triggering transition.

Although the low-frequency fluctuations that correspond to the most amplified primary disturbance are not the focus here, their behavior is quite interesting and could represent a useful topic of further study. These fluctuations start as a spanwise-uniform mode at chord locations where mean flow is not deformed by the stationary vortices. However, these fluctuations appear to be acted upon by the stationary vortices in the same manner as the mean flow, and they become highly localized within the stationary structure even before the stationary mode saturates. Despite the modification of the mean flow and the spatial

Bibliography

ARNAL. D. 1997 Laminar-turbulent transition: Research and applications in France. *AIAA Paper* 97-1905.

BEARMAN. P. W. 1971 Corrections for the effect of ambient temperature drift on hot-wire measurements in incompressible flow. *DISA Information* **11**.

BEVINGTON. P. R. 1969 *Data Reduction and Error Analysis for the Physical Sciences*. New York: McGraw-Hill.

BIPPES. H. 1999 Basic experiments on transition in three-dimensional boundary layers dominated by crossflow instability. *Prog. Aero. Sci.* **35** (4), 363–412.

BRIGGS, R. J. 1964 *Electron-Stream Interaction with Plasmas*. Cambridge: MIT Press.

CARRILLO. JR.. R. B. 1996 Distributed-roughness effects on stability and transition in swept-wing boundary layers. Master's thesis. Arizona State University.

CHAPMAN. K. L. 1996 Structure identification within a transitioning swept-wing boundary layer. PhD thesis. Clarkson University.

CHAPMAN. K. L.. REIBERT. M. S., SARIC, W. S. & GLAUSER. M. N. 1998 Boundary-layer transition detection and structure identification through surface shear-stress measurements. *AIAA Paper* 98-0782.

CHOUDHARI. M. 1994 Roughness-induced generation of crossflow vortices in three-dimensional boundary layers. *Theor. Comput. Fluid Dyn.* **6**. 1–30.

COLLIS. S. S. & LELE. S. K. 1999 Receptivity to surface roughness near a swept leading edge. *J. Fluid Mech.* **380**. 141–168.

CROUCH. J. 1997 Transition prediction and control for airplane applications. *AIAA Paper* 97-1907.

CROUCH. J. D. 1994 Theoretical studies on receptivity of boundary layers. *AIAA Paper* 94-2224.

DAGENHART. J. R. 1992 Crossflow stability and transition experiments in swept-wing flow. PhD thesis. Virginia Polytechnic Institute and State University, also available as NASA-TP 1999-209344 by J. R. Dagenhart & W. S. Saric.

DAGENHART. J. R. & SARIC. W. S. 1999 Crossflow stability and transition experiments in swept-wing flow. *NASA TP* 1999-209344. Originally appeared as a Virginia Polytechnic Institute PhD thesis by Dagenhart. 1992.

KOHAMA. Y. 1985 Turbulent transition process of the spiral vortices appearing in the laminar boundary layer of a rotating cone. *PhysicoChemical Hydrodynamics* **6** (5), 659–669.

KOHAMA. Y. 1987 Some expectations on the mechanism of cross-flow instability in a swept-wing flow. *Acta Mechanica* **66**, 21–38.

KOHAMA, Y., SARIC, W. S. & HOOS, J. A. 1991 A high-frequency, secondary instability of crossflow vortices that leads to transition. In *Proc. of the Royal Aero. Soc. Conf. on Boundary-Layer Trans. and Control*.

KOHAMA. Y., UKAKU, M. & OHTA. F. 1987 Boundary-layer transition on a swept cylinder. In *Proceedings of the International Conference on Fluid Mechanics*. Beijing: Peking University Press.

LERCHE. T. 1996 Experimental investigation of nonlinear wave interactions and secondary instability in three-dimensional boundary-layer flow. In *6th European Turbulence Conference. Lausanne* (ed. S. Gavrilakis, L. Machiels & P. A. Monkewitz), pp. 357–360.

LERCHE. T. & BIPPES, H. 1996 Experimental investigation of cross-flow instability under the influence of controlled disturbance excitation. In *Trans. boundary layers in aeronautics* (ed. R. Henkes & J. van Ingen).

LI. F. & MALIK. M. R. 1995 Fundamental and subharmonic secondary instabilities of Görtler vortices. *J. Fluid Mech.* **297**, 77–100.

LINGWOOD. R. J. 1995 Absolute instability of the boundary layer on a rotating disk. *J. Fluid Mech.* **299**, 17–33.

LINGWOOD, R. J. 1996 An experimental study of absolute instability of the rotating-disk boundary layer flow. *J. Fluid Mech.* **314**, 373–405.

LINGWOOD. R. J 1997 On the impulse response for swept boundary-layer flows. *J. Fluid Mech.* **344**, 317–334.

MALIK. M. R.. LI. F. & CHANG. C.-L. 1994 Crossflow disturbances in three-dimensional boundary layers: Nonlinear development, wave interaction and secondary instability. *J. Fluid Mech.* **268**, 1–36.

MALIK. M. R.. LI. F. & CHANG. C.-L. 1996 Nonlinear crossflow disturbances and secondary instabilities in swept-wing boundary layers. In *IUTAM Symposium on Nonlinear Instability and Transition in Three-Dimensional Boundary Layers* (ed. P. W. Duck & P. Hall). pp. 257–266. Kluwer.

MALIK. M. R., LI. F., CHOUDHARI, M. M. & CHANG. C.-L. 1999 Secondary instability of crossflow vortices and swept-wing boundary layer transition. *J. Fluid Mech.* **399**, 85–115.

MEYER. F. & KLEISER. L. 1989 Numerical investigation of transition in 3D boundary layers. In *Fluid Dynamics of Three-Dimensional Turbulent Shear Flows and Transition, AGARD CP* 438.

MÜLLER. B. 1990 Experimental study of the travelling waves in a three-dimensional boundary layer. In *IUTAM Symposium on Laminar-Turbulent Transition, Toulouse* (ed. D. Arnal & R. Michel), pp. 489–499. Springer.

SWEARINGEN, J. D. & BLACKWELDER, R. F. 1987 The growth and breakdown of stream-wise vortices in the presence of a wall. *J. Fluid Mech.* **182**, 255–290.

TAYLOR, M. J. & PEAKE, N. 1998 The long-time behaviour of incompressible swept-wing boundary layers subject to impulsive forcing. *J. Fluid Mech* **355**, 359–381.

TAYLOR, M. J. & PEAKE, N. 1999 The long-time impulse response of compressible swept-wing boundary layers. *J. Fluid Mech* **379**, 333–350.

WINTERGERSTE, T. & KLEISER, L. 1996 Direct numerical simulation of transition in a three-dimensional boundary layer. In *Transitional Boundary Layers in Aeronautics* (ed. R. A. W. M. Henkes & J. L. van Ingen).
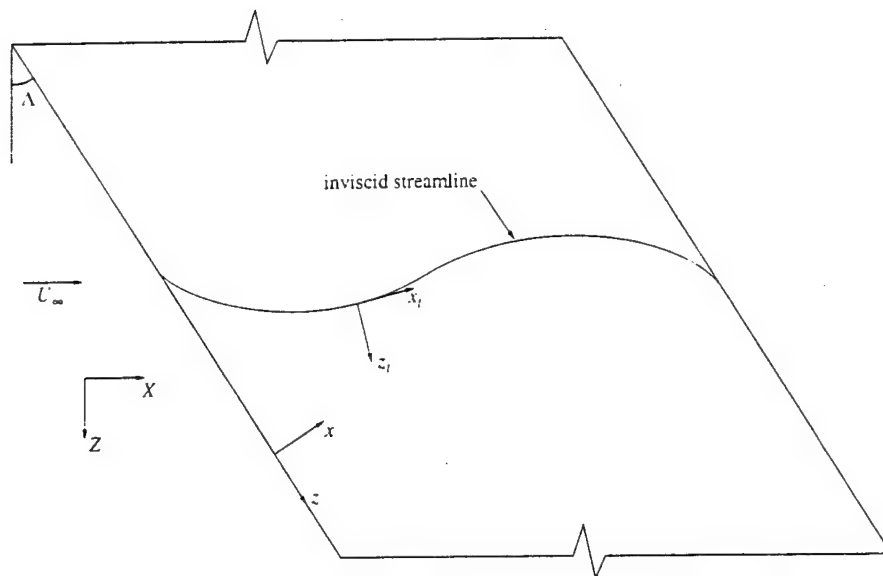
Figure 1: Swept-wing streamline and coordinate systems.
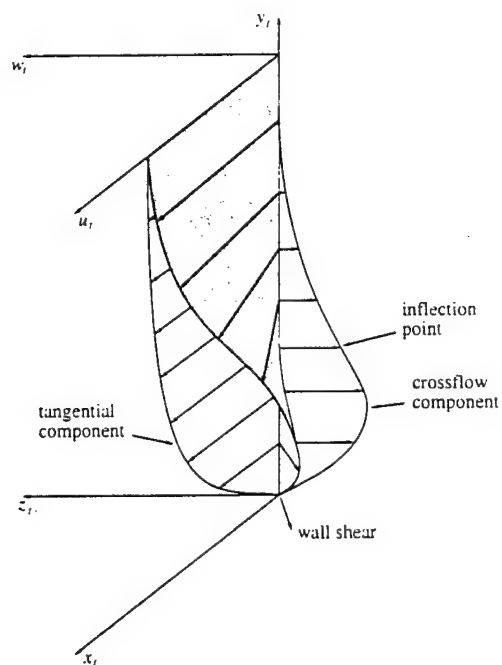
Figure 2: Crossflow boundary-layer profiles.

68
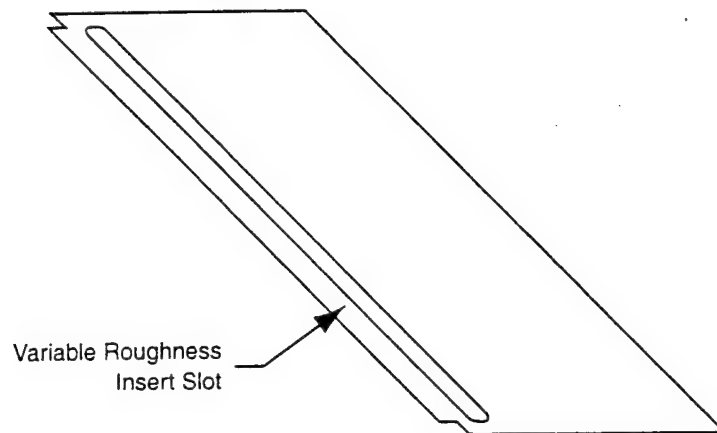
Figure 5: Modular leading-edge insert for the ASU(67)-0315.
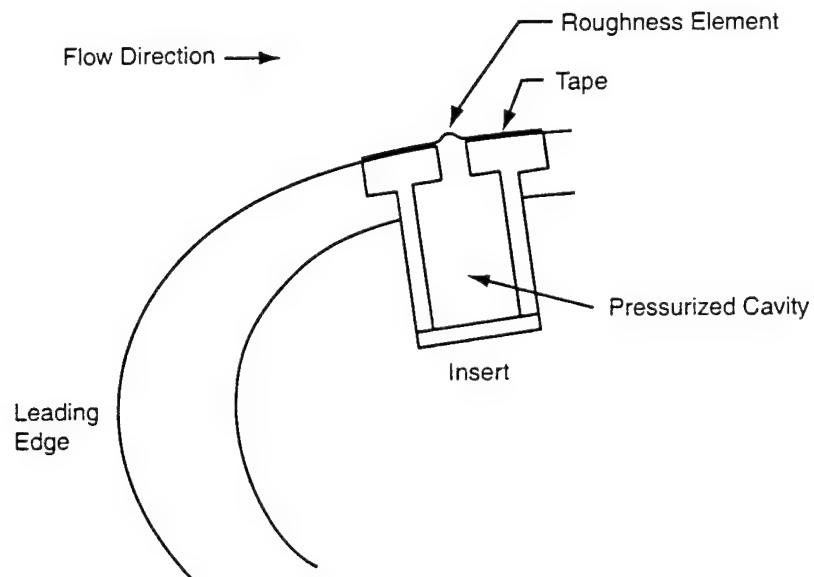
Figure 6: Schematic cross section of the variable leading-edge roughness device.
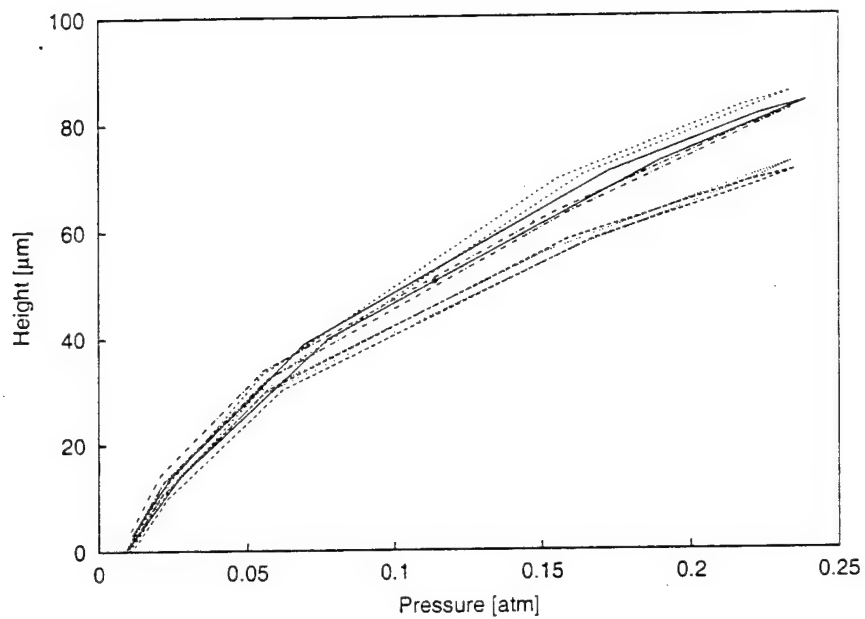
Figure 9: Center-displacement height versus pressure difference, Δp, across 3-mm-diameter roughness elements. Different line styles indicate different elements.
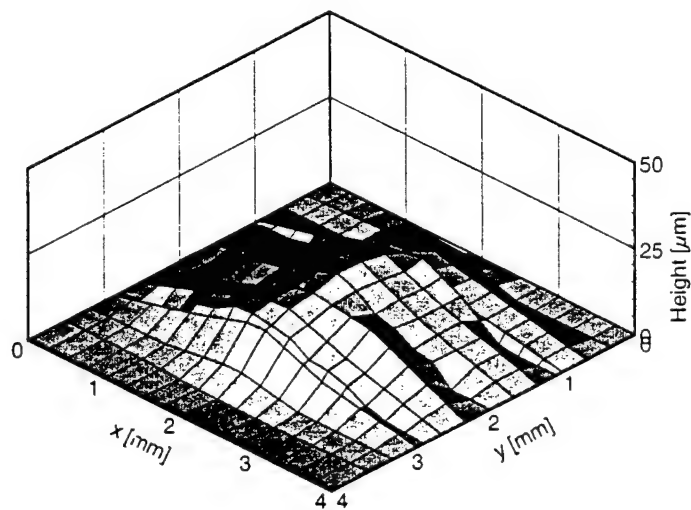
Figure 10: Activated 3-mm-diameter roughness shape of a 10-μm-high element.
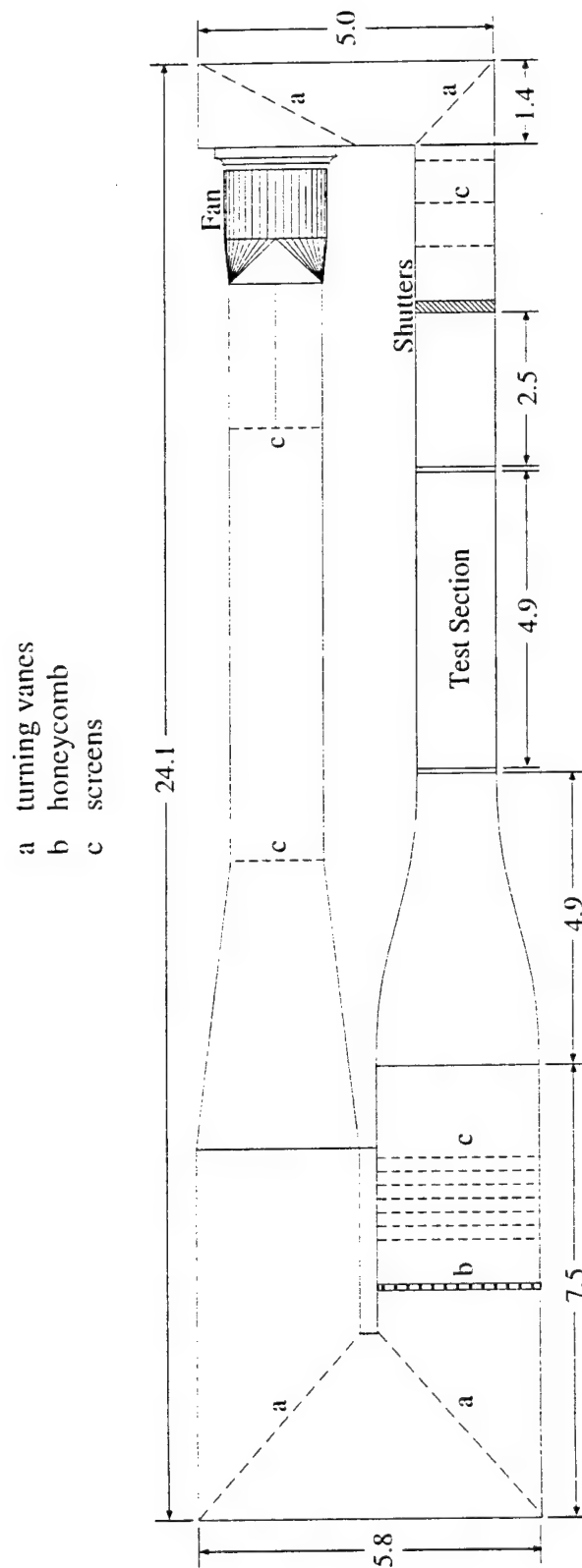
Figure 12: Schematic view of the Unsteady Wind Tunnel. All dimensions in meters.
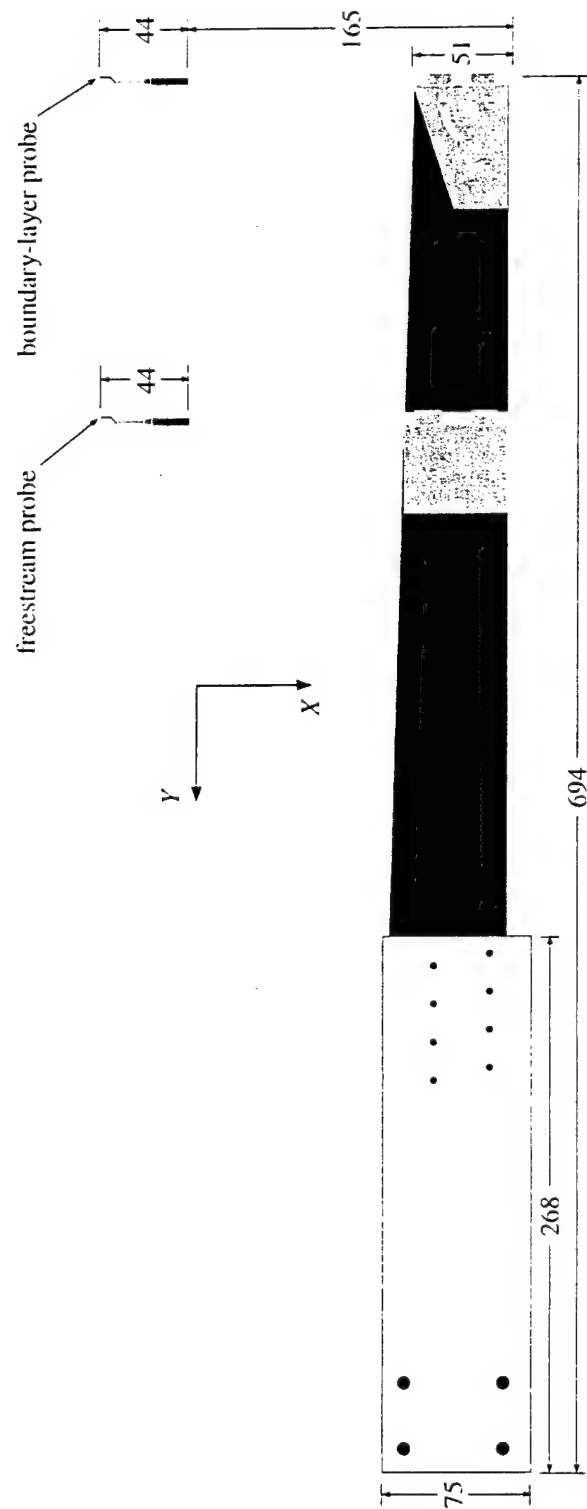
Figure 15: Top view of the hotwire sting. All dimensions in millimeters.
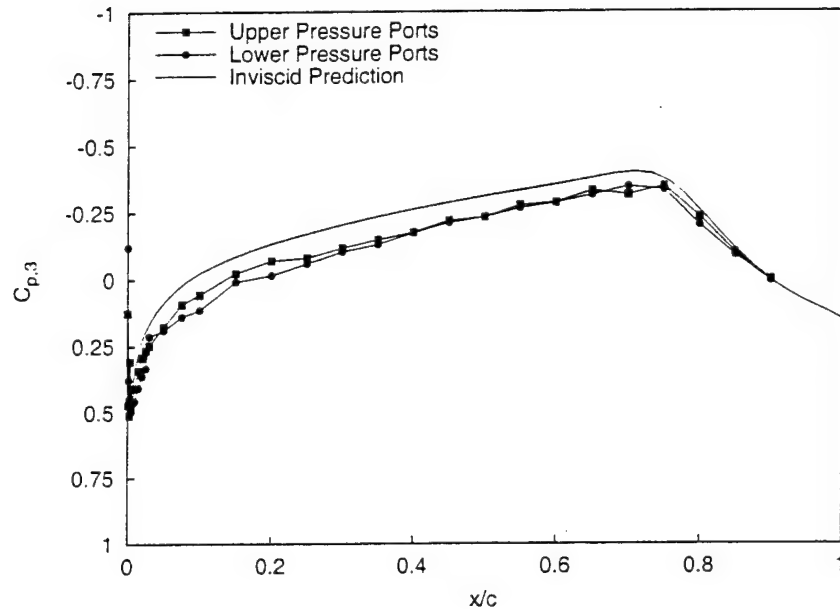
Figure 18: Upper and lower span suction-side $C_{p,3}$ distributions at $Re_c = 2.4 \times 10^6$.
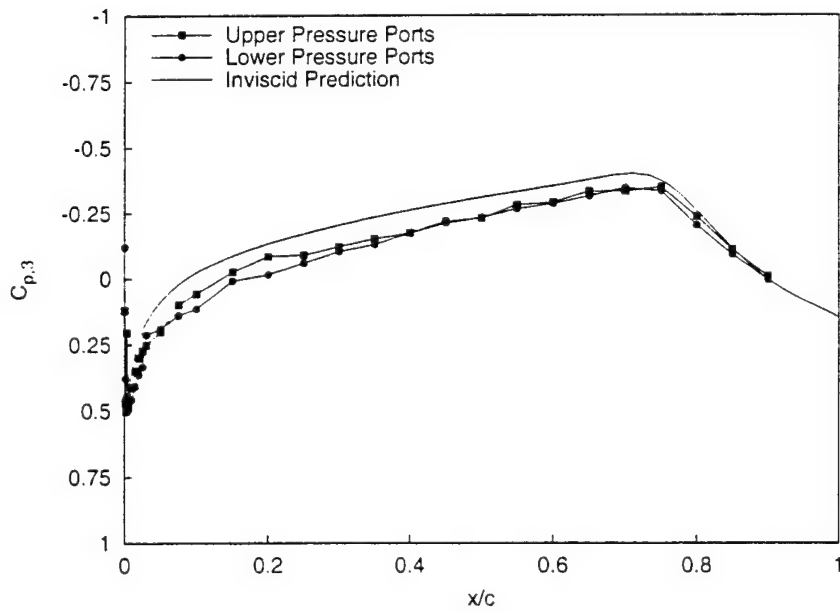
Figure 19: Upper and lower span suction-side $C_{p,3}$ distributions at $Re_c = 2.8 \times 10^6$.
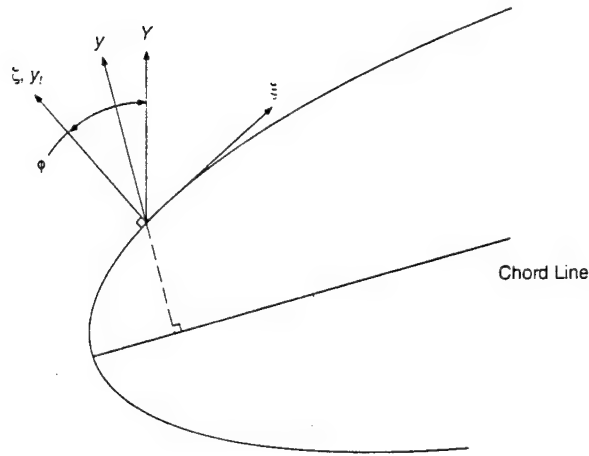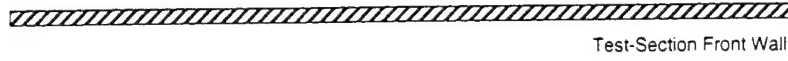
Figure 22: Coordinate systems, X, Y plane.
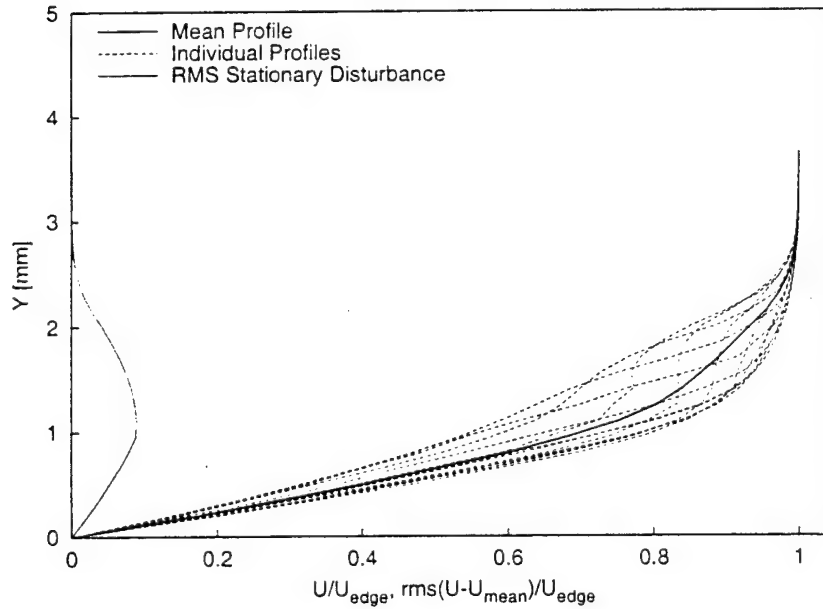
Figure 23: Mean-flow velocity profiles. $Re_c = 2.4 \times 10^6$, [18|12] roughness, $x/c = 0.30$, $z = 117$–128 mm.
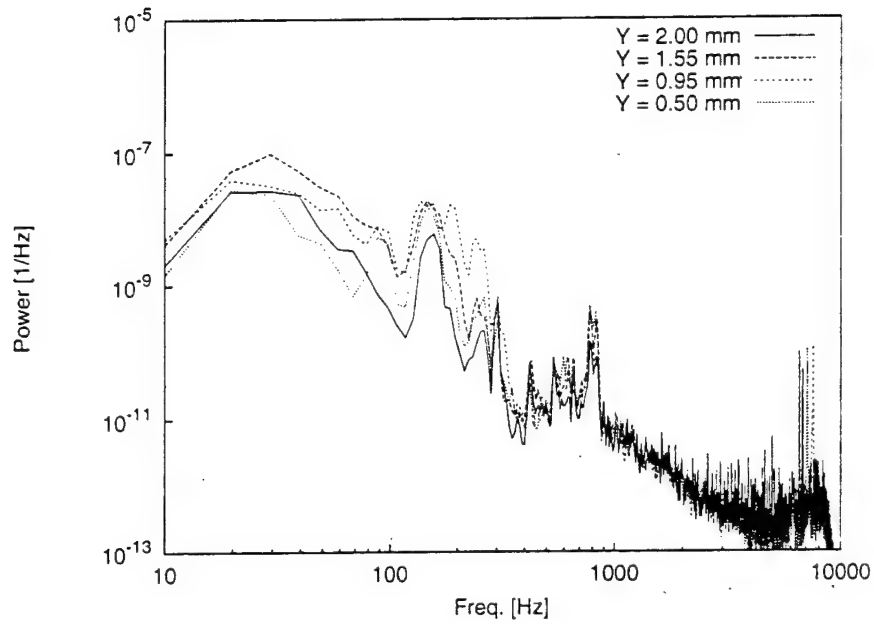
Figure 26: Fluctuating-velocity spectra, $Re_c = 2.4 \times 10^6$, [18|12] roughness, $x/c = 0.30$, $z = 122$ mm.
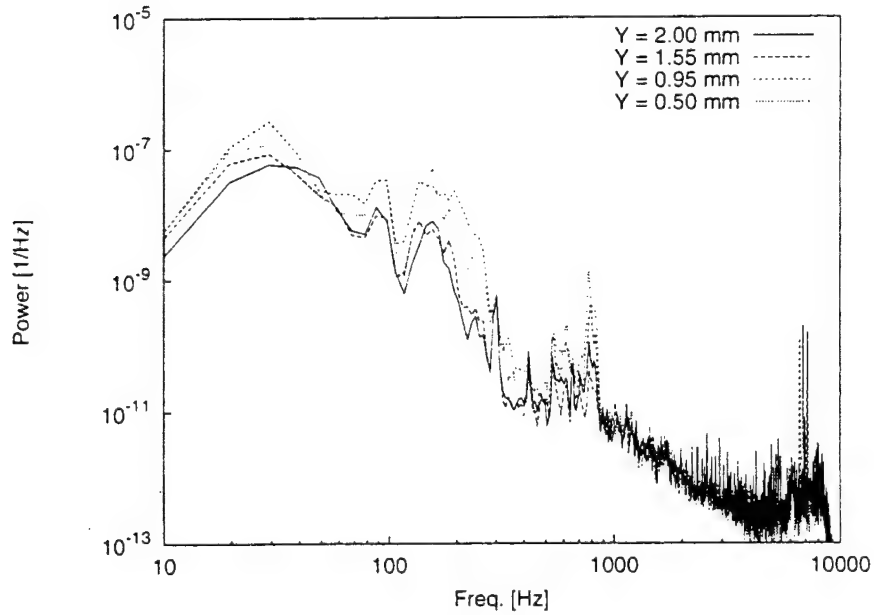
Figure 27: Fluctuating-velocity spectra, $Re_c = 2.4 \times 10^6$, [18|12] roughness, $x/c = 0.30$, $z = 125$ mm.
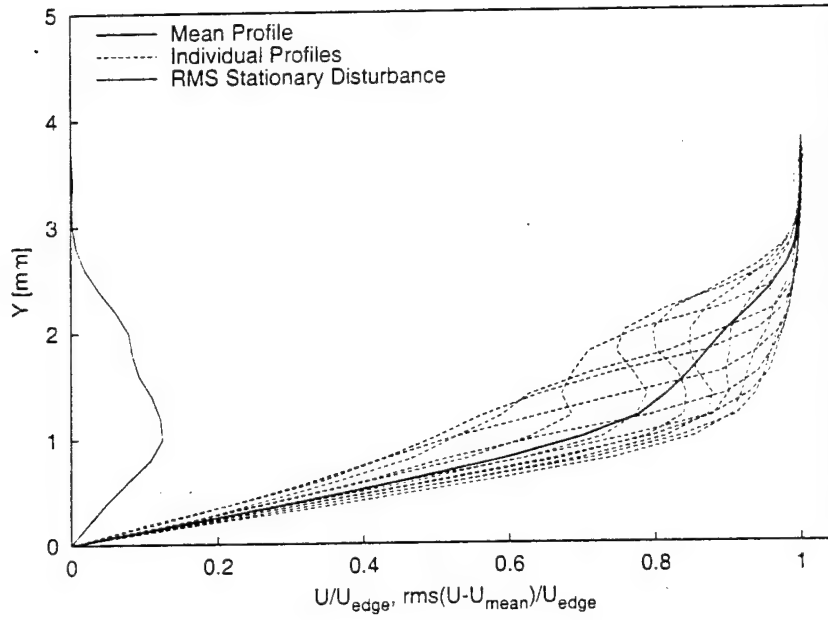
Figure 30: Mean-flow velocity profiles. $Re_c = 2.4 \times 10^6$, [18|12] roughness. $x/c = 0.35$, $z = 103\text{--}114\,\text{mm}$.
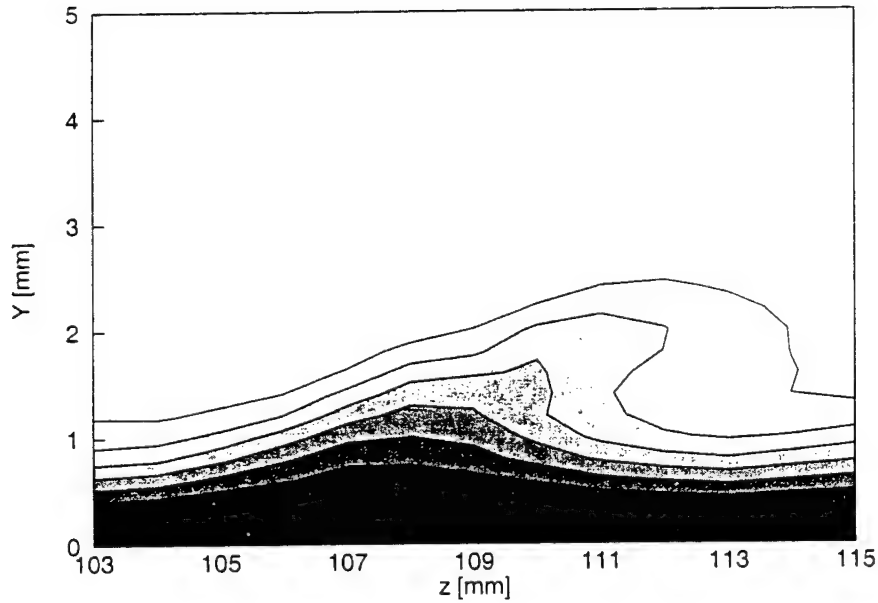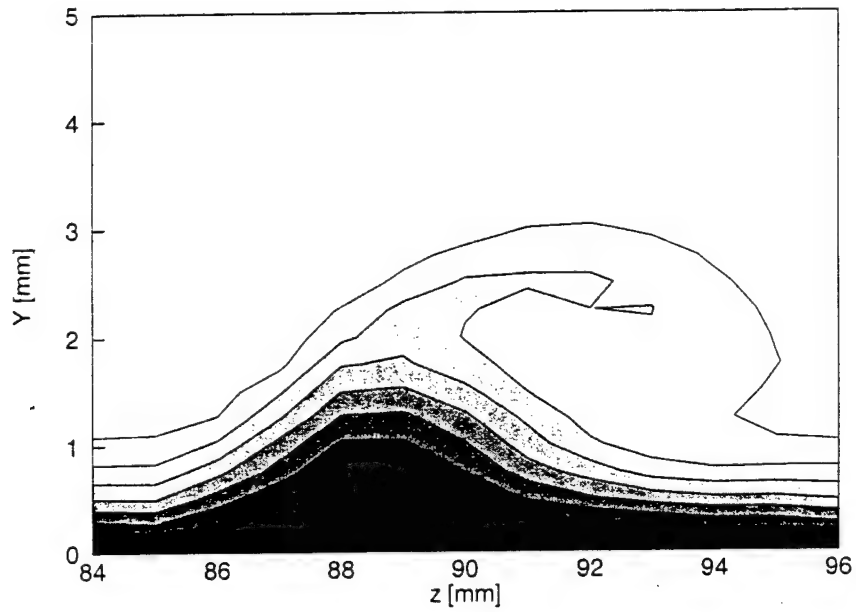

Figure 31: Mean-flow velocity contours, $Re_c = 2.4 \times 10^6$, [18|12] roughness. $x/c = 0.35$, contour lines at $U/U_{\text{edge}} = 0.10$, 0.20, ..., 0.90.
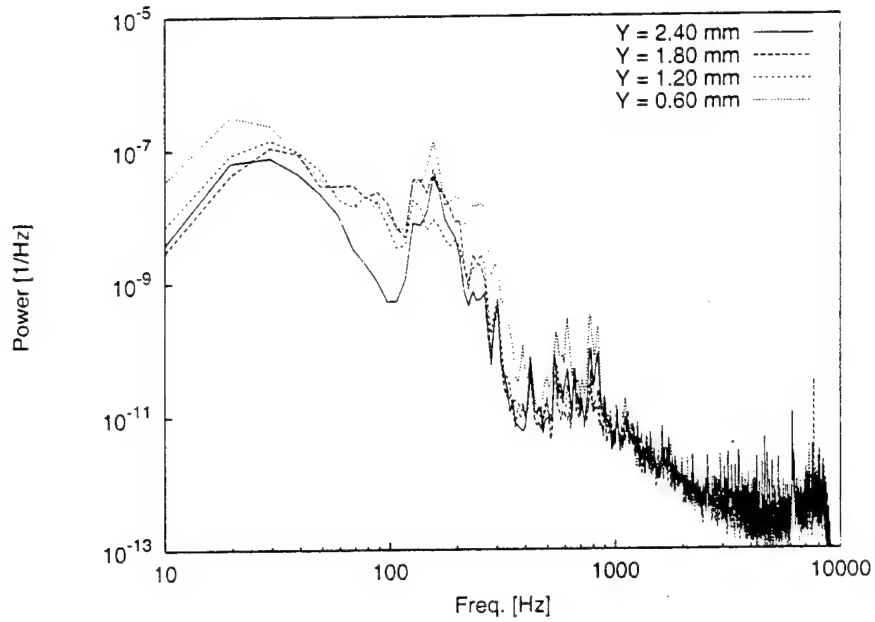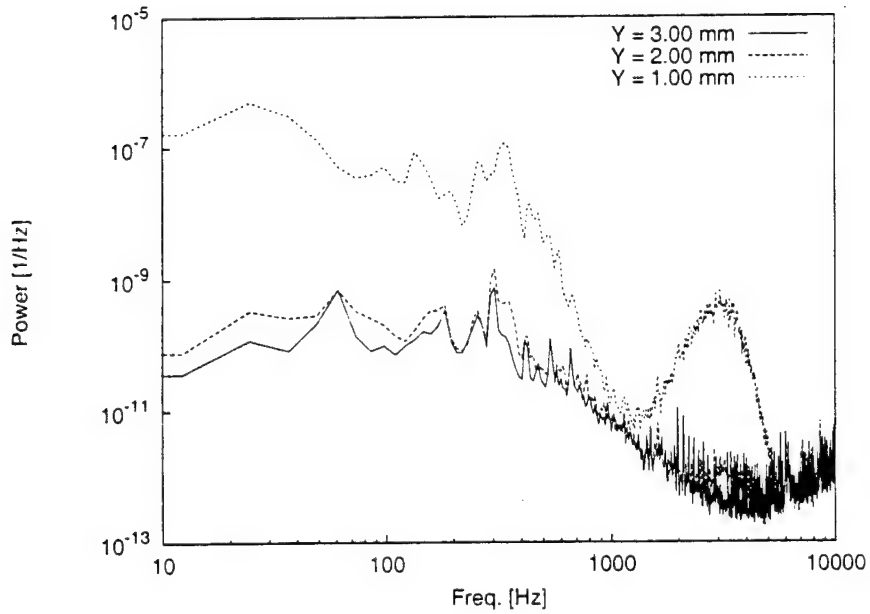
Figure 34: Fluctuating-velocity spectra. $Re_c = 2.4 \times 10^6$, [18|12] roughness, $x/c = 0.35$. $z = 111$ mm.
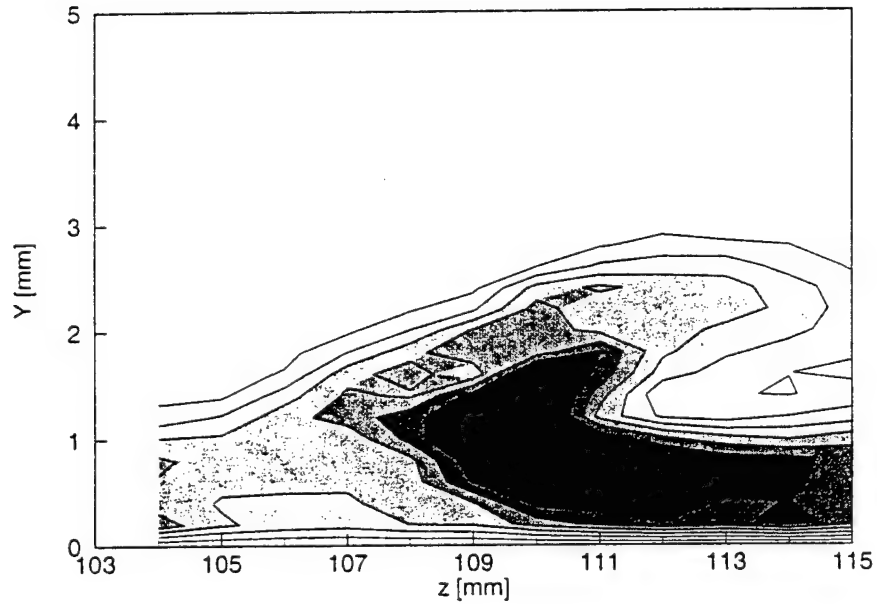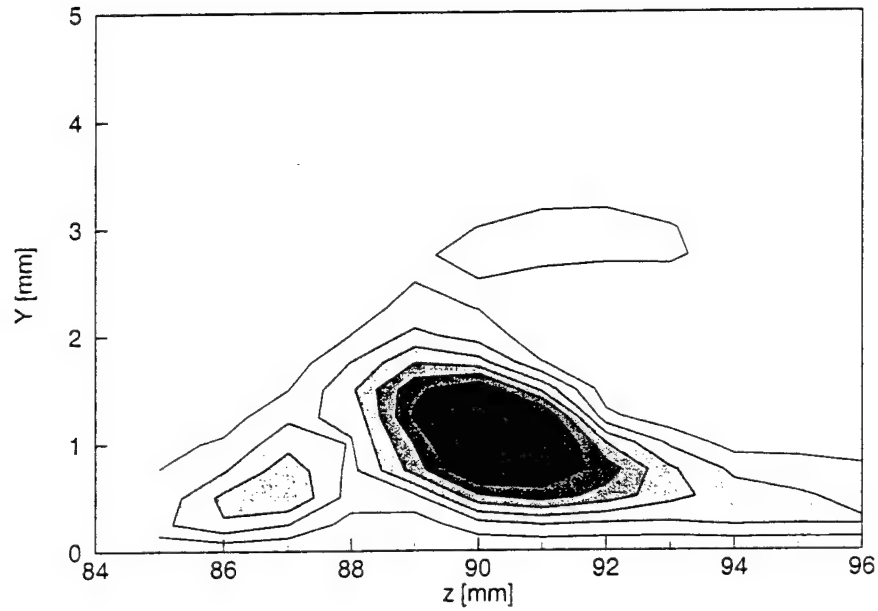

Figure 35: 200-Hz velocity-fluctuation rms distribution, $Re_c = 2.4 \times 10^6$, [18|12] roughness, $x/c = 0.35$, 100–300-Hz bandpass. Lines are 10% contours of the maximum in this band.
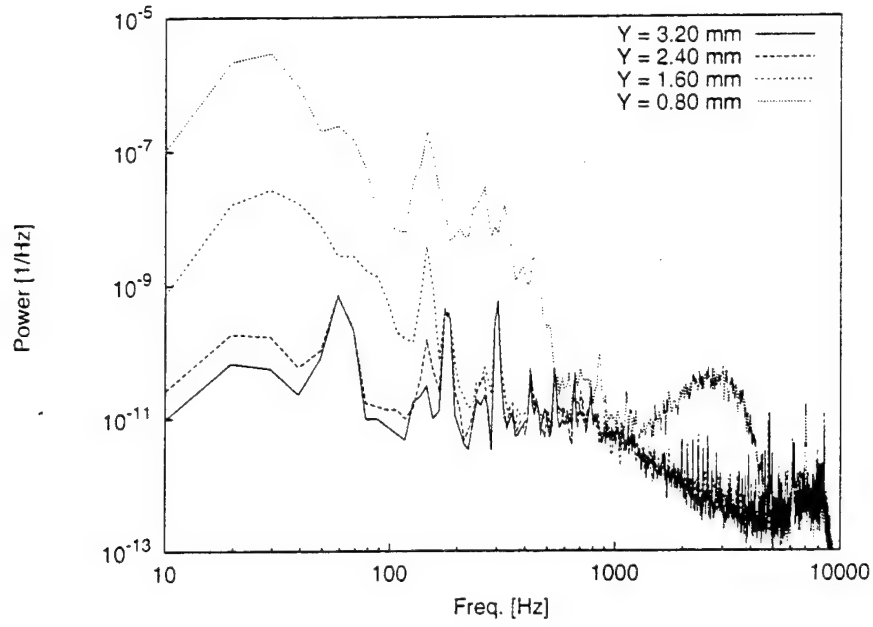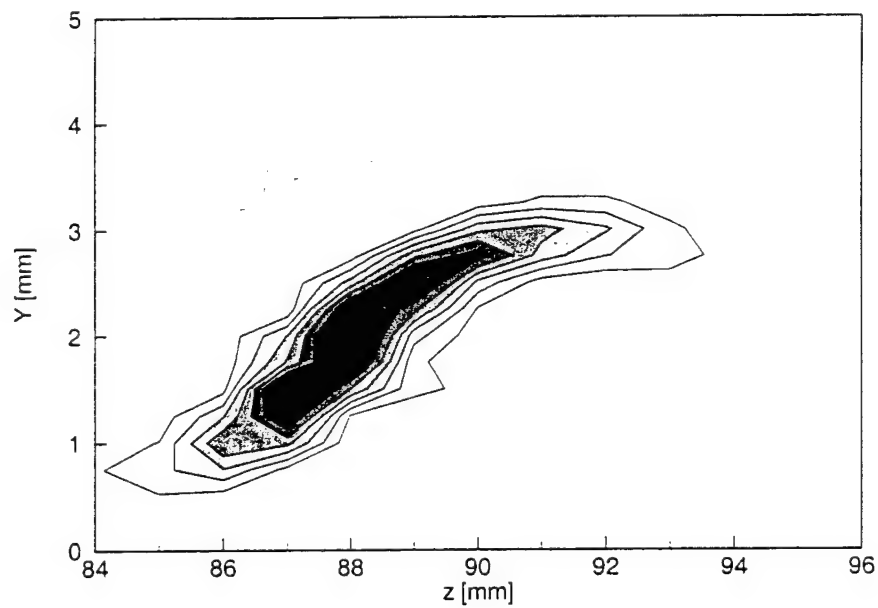
Figure 38: Fluctuating-velocity spectra, $Re_c = 2.4 \times 10^6$, [18|12] roughness, $x/c = 0.40$, $z = 91$ mm.
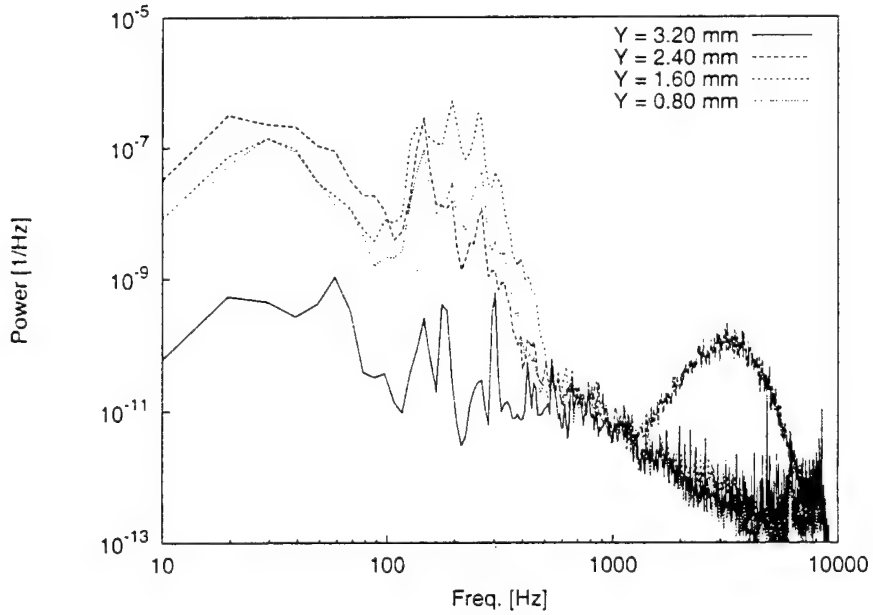
Figure 39: Fluctuating-velocity spectra, $Re_c = 2.4 \times 10^6$, [18|12] roughness, $x/c = 0.40$, $z = 94$ mm.
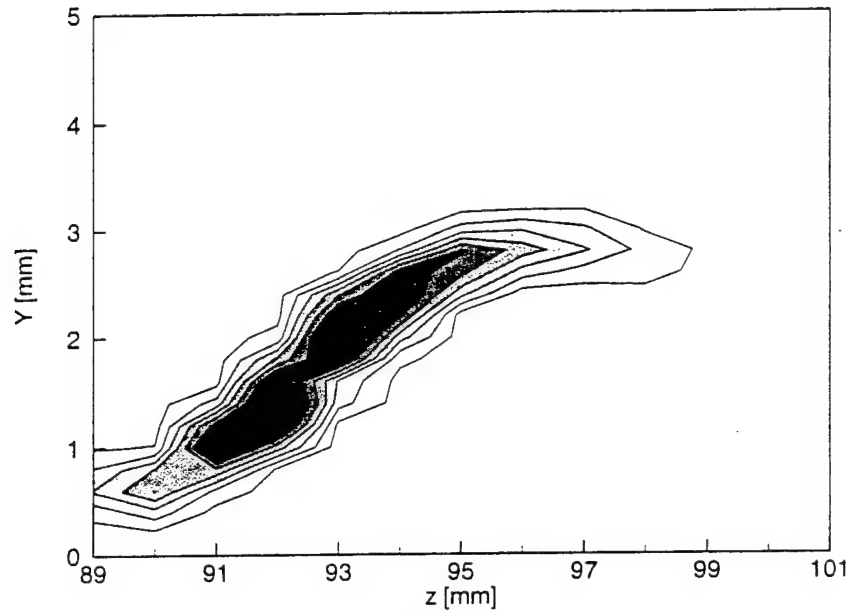
Figure 42: 3.0-kHz velocity-fluctuation rms distribution, $Re_c = 2.4 \times 10^6$, [18|12] roughness, $x/c = 0.40$. 2.9–3.1-Hz bandpass. Lines are 10% contours of the maximum in this band.
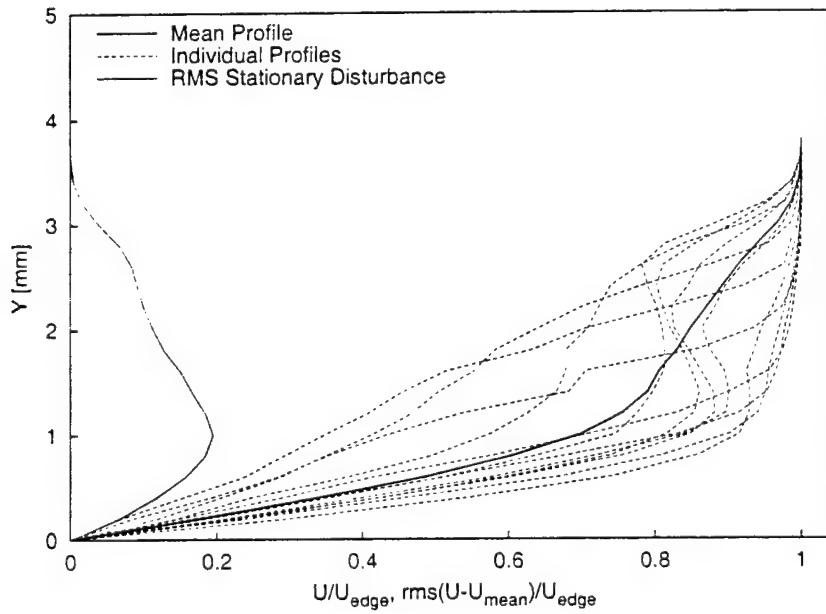

Figure 43: Mean-flow velocity profiles, $Re_c = 2.4 \times 10^6$, [18|12] roughness, $x/c = 0.41$, $z = 85$–96 mm.
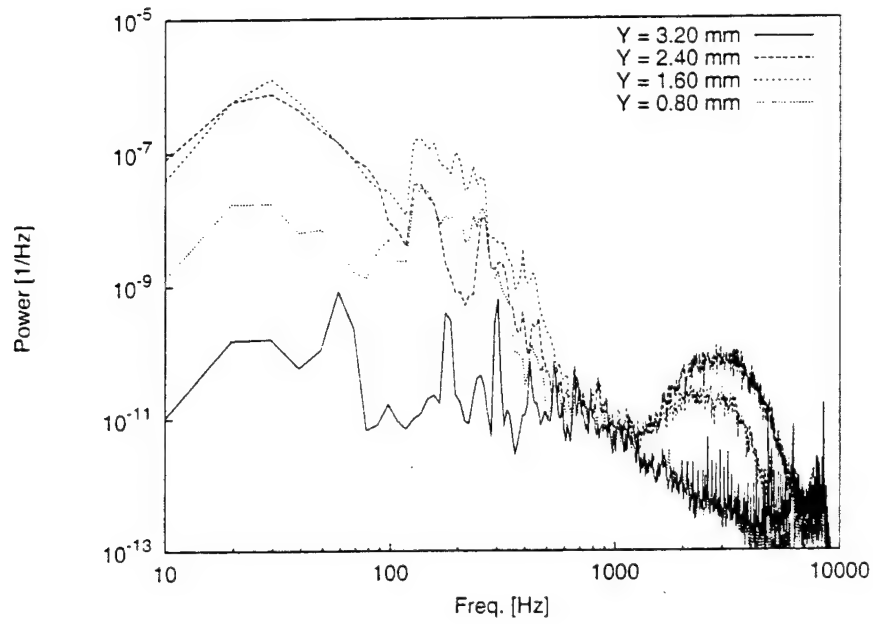
Figure 46: Fluctuating-velocity spectra. $Re_c = 2.4 \times 10^6$, [18|12] roughness, $x/c = 0.41$, $z = 90$ mm.
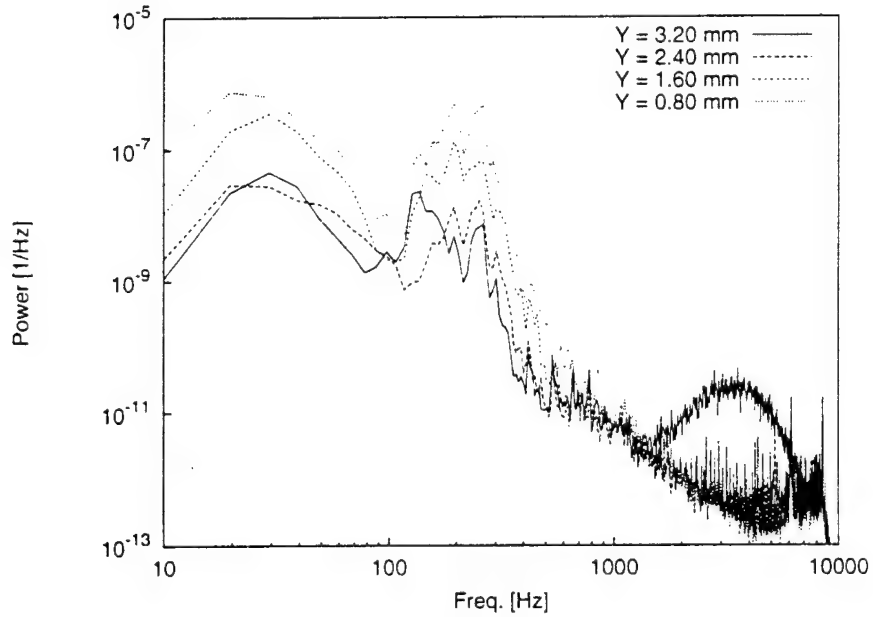
Figure 47: Fluctuating-velocity spectra, $Re_c = 2.4 \times 10^6$, [18|12] roughness, $x/c = 0.41$, $z = 93$ mm.
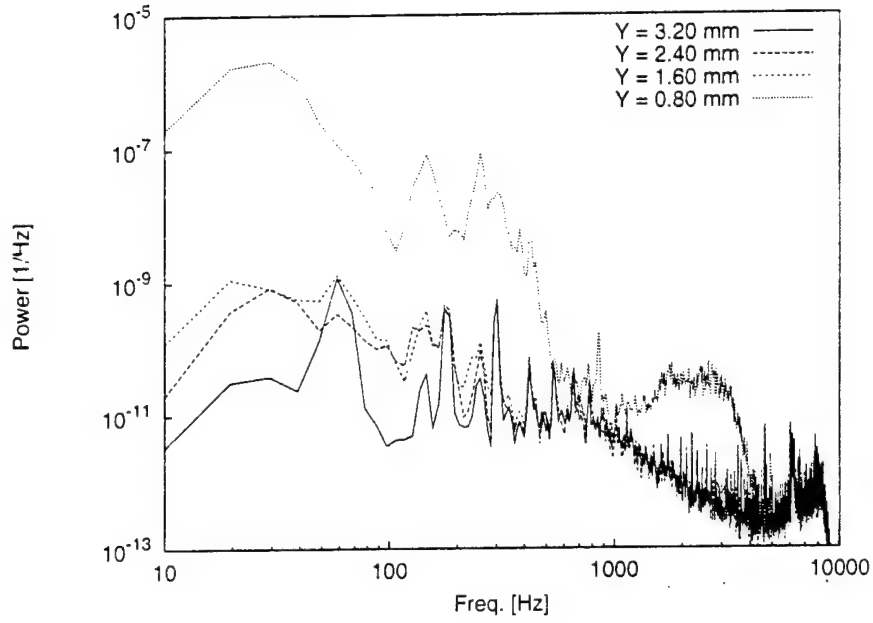
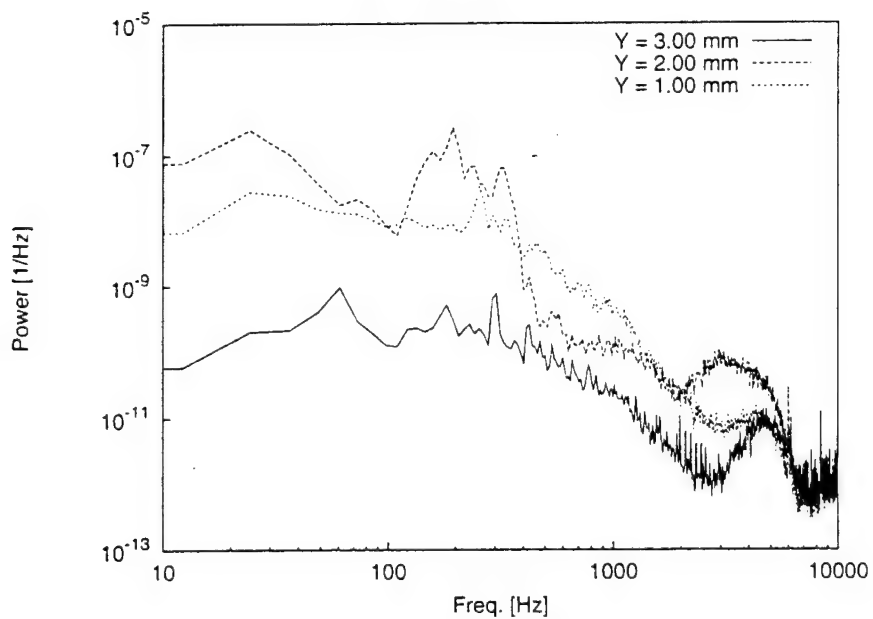Figure 50: Fluctuating-velocity spectra, $Re_c = 2.4 \times 10^6$, [18|12] roughness, $x/c = 0.42$, $z = 84$ mm.
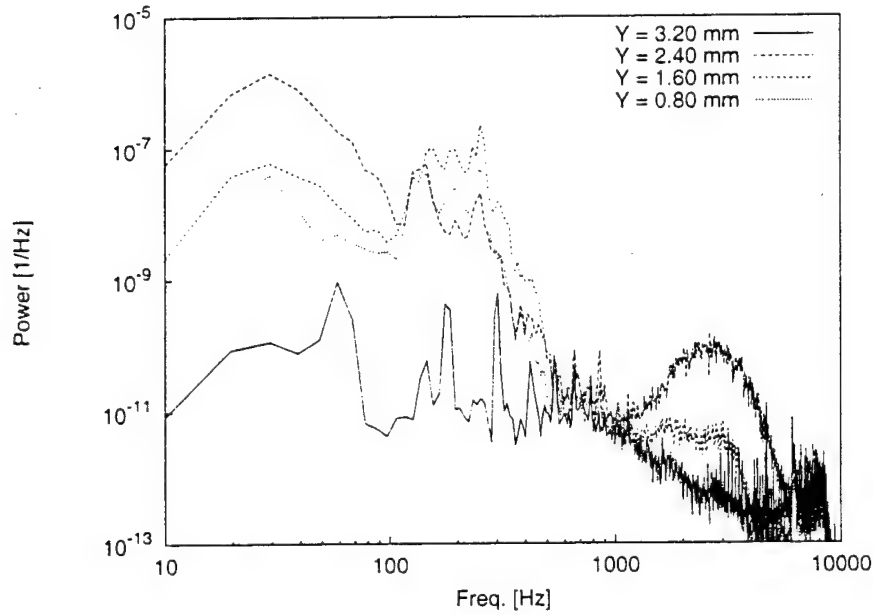
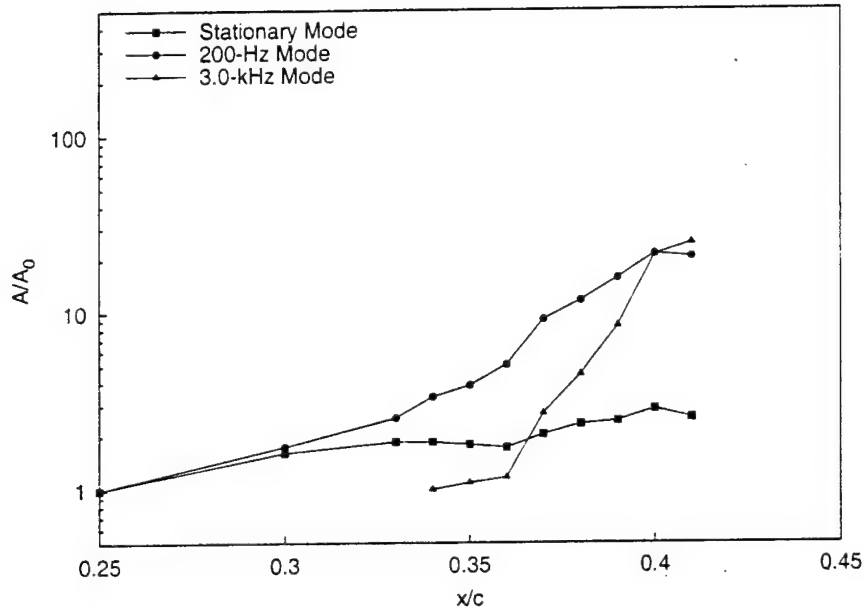Figure 51: Fluctuating-velocity spectra, $Re_c = 2.4 \times 10^6$, [18|12] roughness, $x/c = 0.42$, $z = 87$ mm.

94
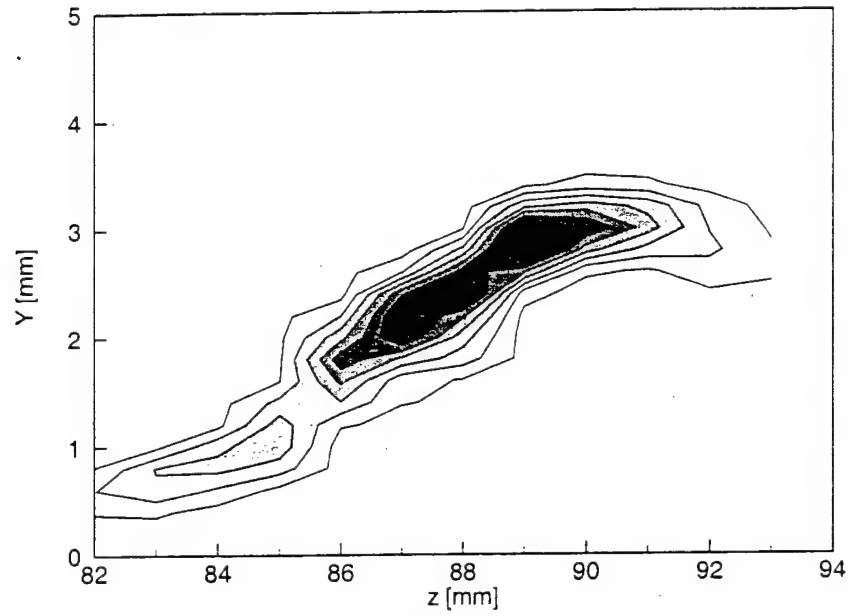
Figure 54: 3.0-kHz velocity-fluctuation rms distribution, $Re_c = 2.4 \times 10^6$, [18|12] roughness, $x/c = 0.42$, 2.9–3.1-kHz bandpass. Lines are 10% contours of the maximum in this band.
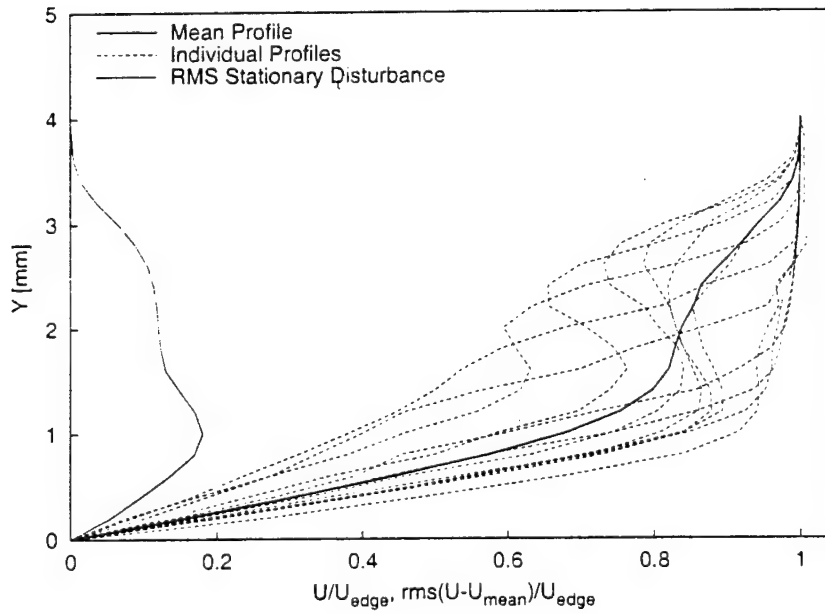
Figure 55: Mean-flow velocity profiles. $Re_c = 2.4 \times 10^6$, [18|12] roughness, $x/c = 0.43$. $z = 79$–90 mm.
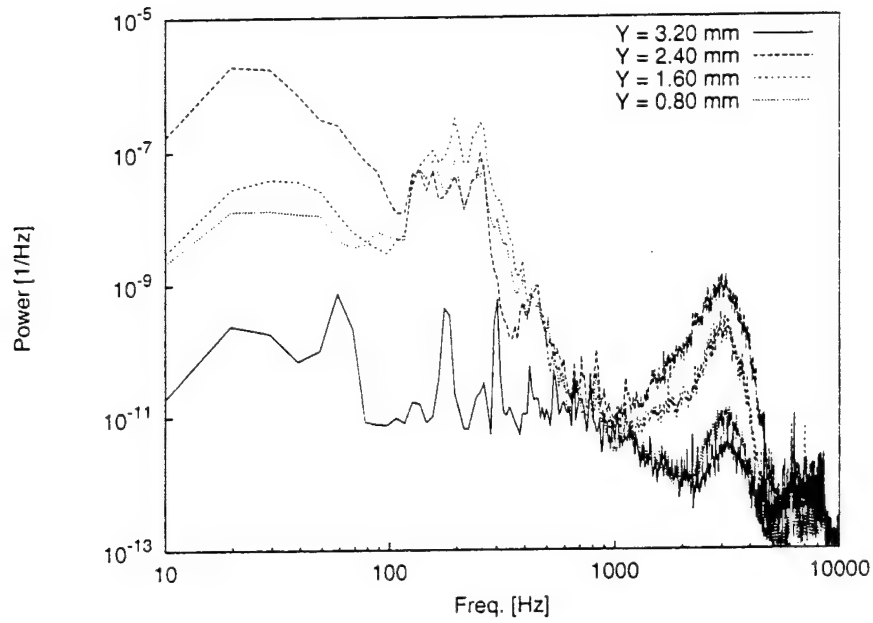
Figure 58: Fluctuating-velocity spectra, $Re_c = 2.4 \times 10^6$, [18|12] roughness, $x/c = 0.43$, $z = 84$ mm.
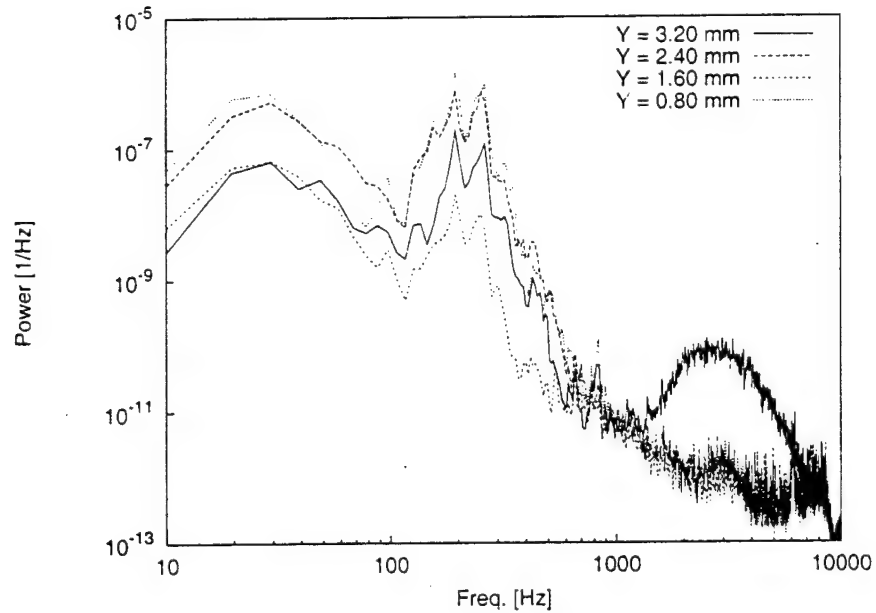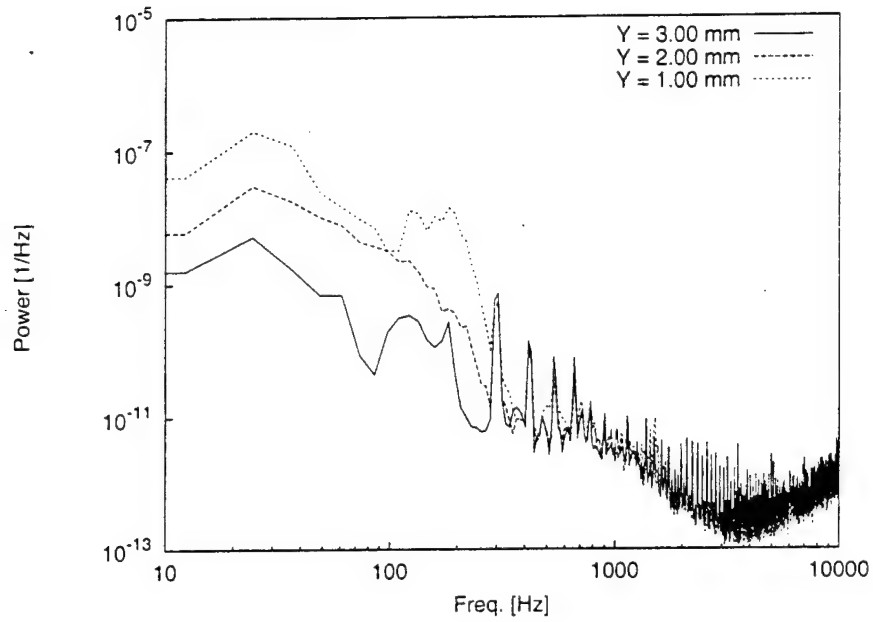

Figure 59: Fluctuating-velocity spectra, $Re_c = 2.4 \times 10^6$, [18|12] roughness, $x/c = 0.43$, $z = 87$ mm.
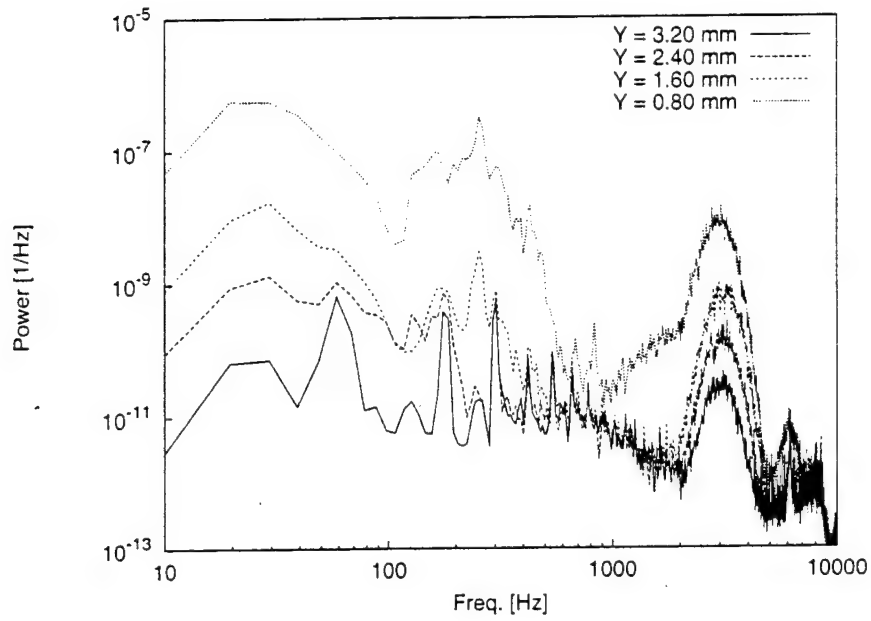
Figure 62: Fluctuating-velocity spectra, $Re_c = 2.4 \times 10^6$, [18|12] roughness, $x/c = 0.44$, $z = 78\,\text{mm}$.
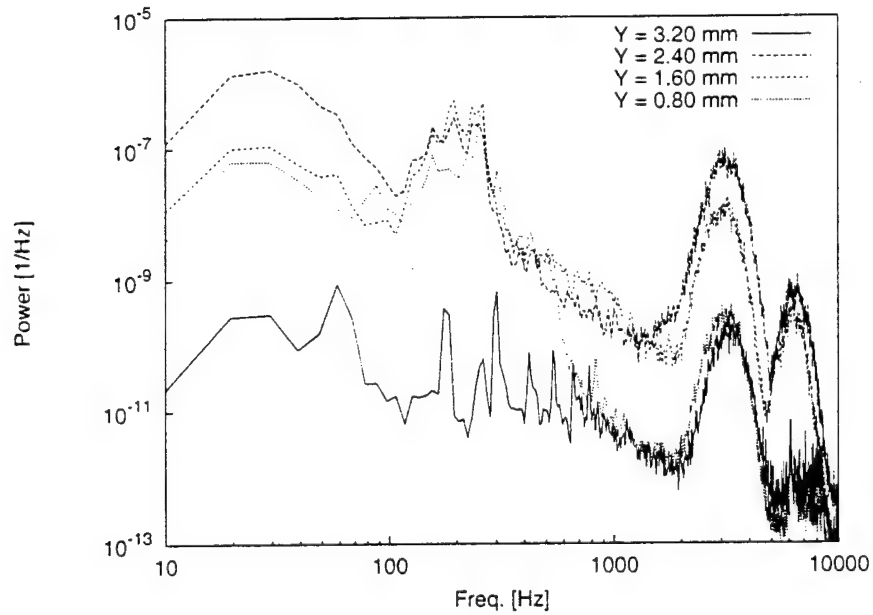
Figure 63: Fluctuating-velocity spectra, $Re_c = 2.4 \times 10^6$, [18|12] roughness, $x/c = 0.44$, $z = 81\,\text{mm}$.
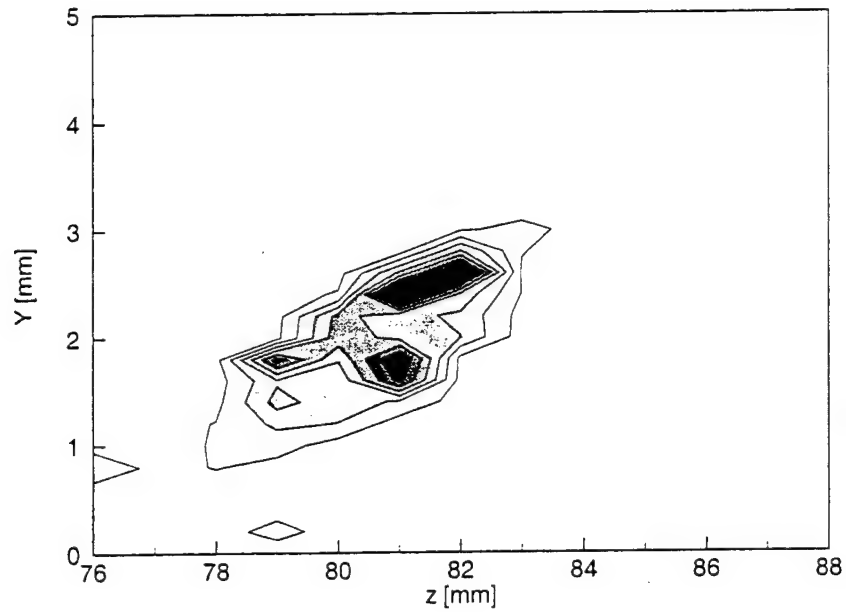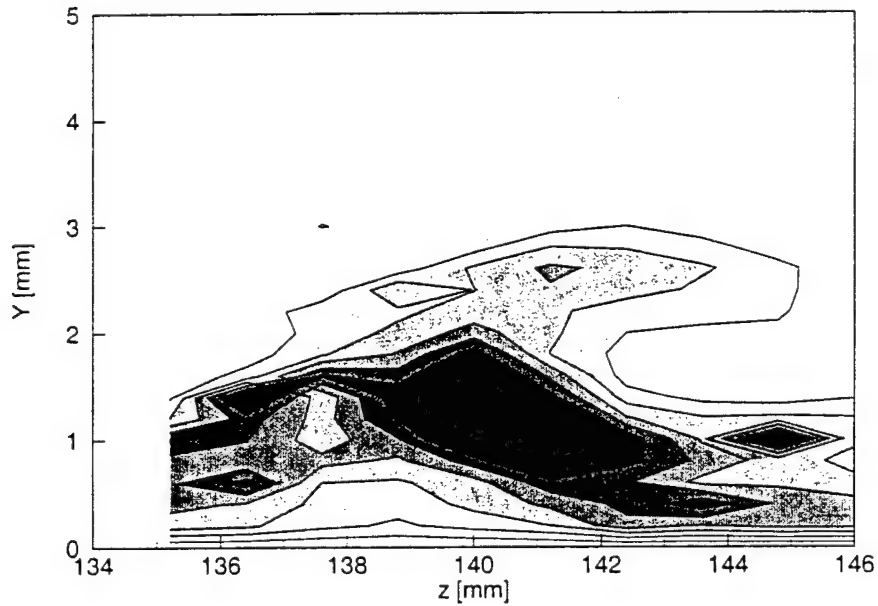
Figure 66: 6.1-kHz velocity-fluctuation rms distribution, $Re_c = 2.4 \times 10^6$, [18|12] roughness, $x/c = 0.44$, 6.0–6.2-Hz bandpass. Lines are 10% contours of the maximum in this band.
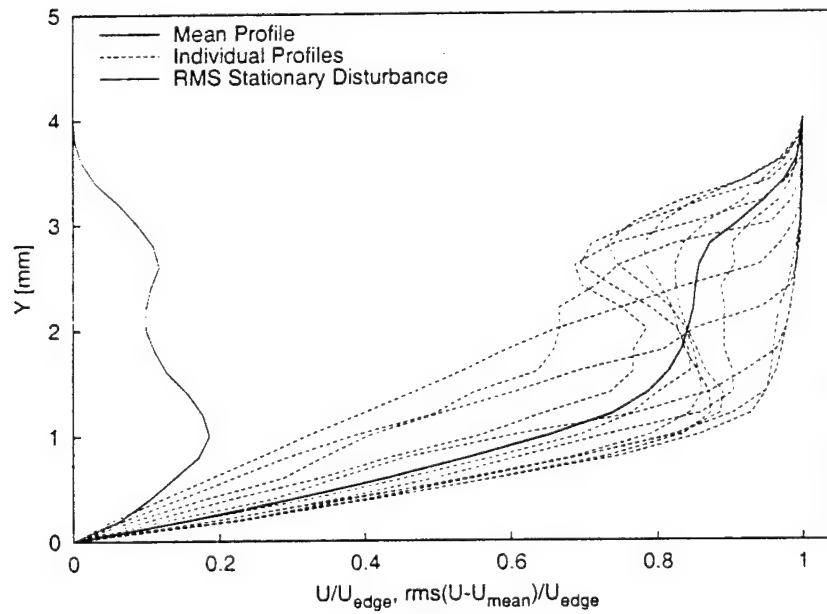

Figure 67: Mean-flow velocity profiles, $Re_c = 2.4 \times 10^6$, [18|12] roughness, $x/c = 0.45$, $z = 75$–86 mm.

102
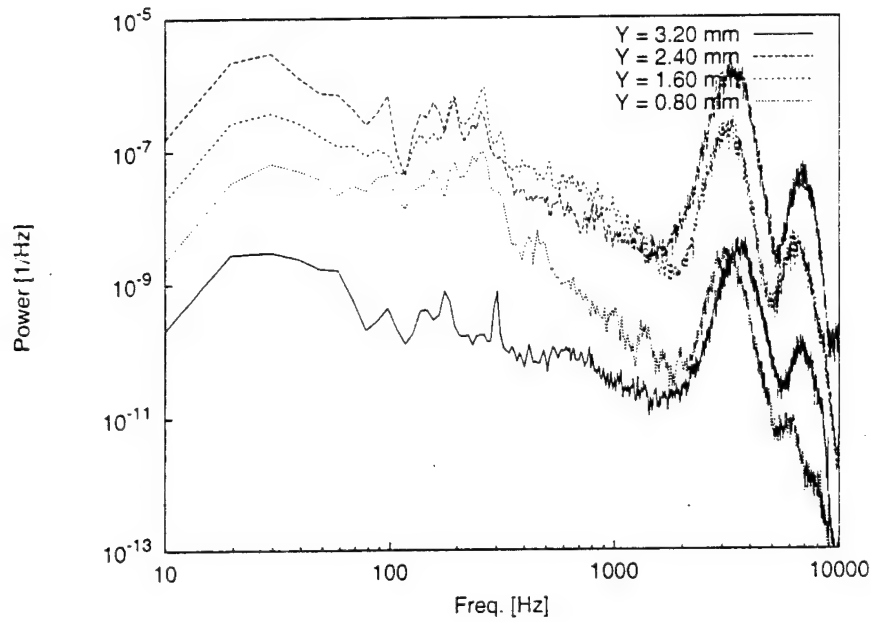
Figure 70: Fluctuating-velocity spectra. $Re_c = 2.4 \times 10^6$, [18|12] roughness, $x/c = 0.45$, $z = 79$ mm.
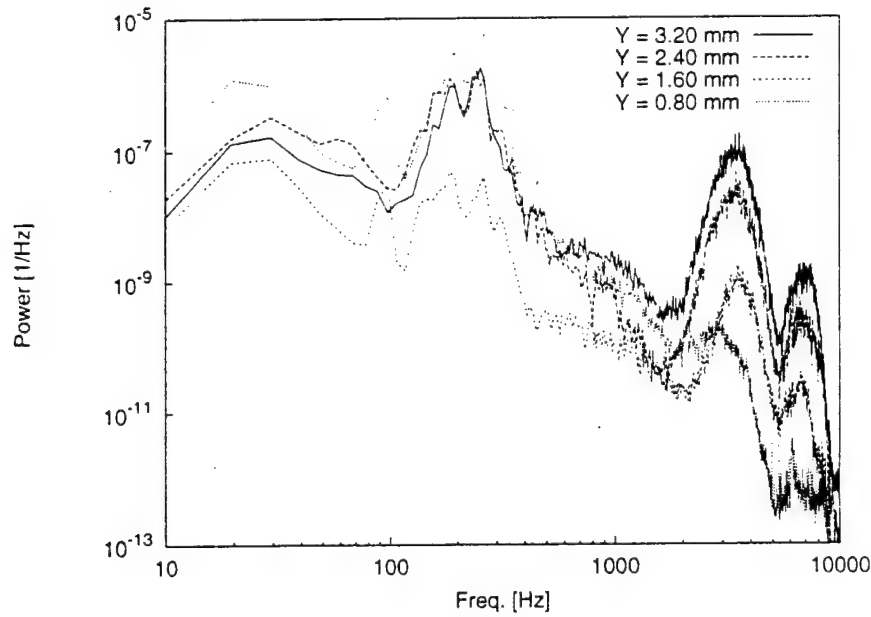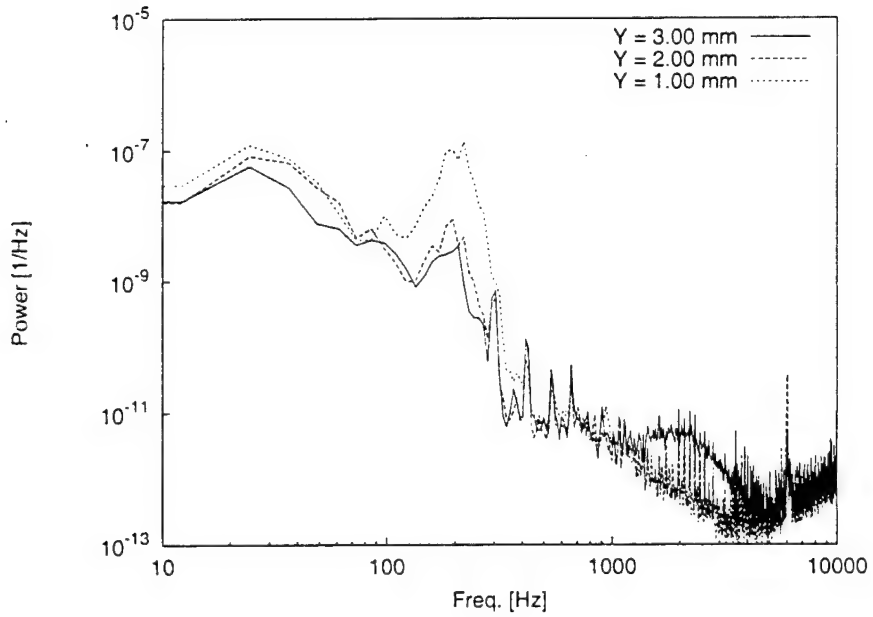

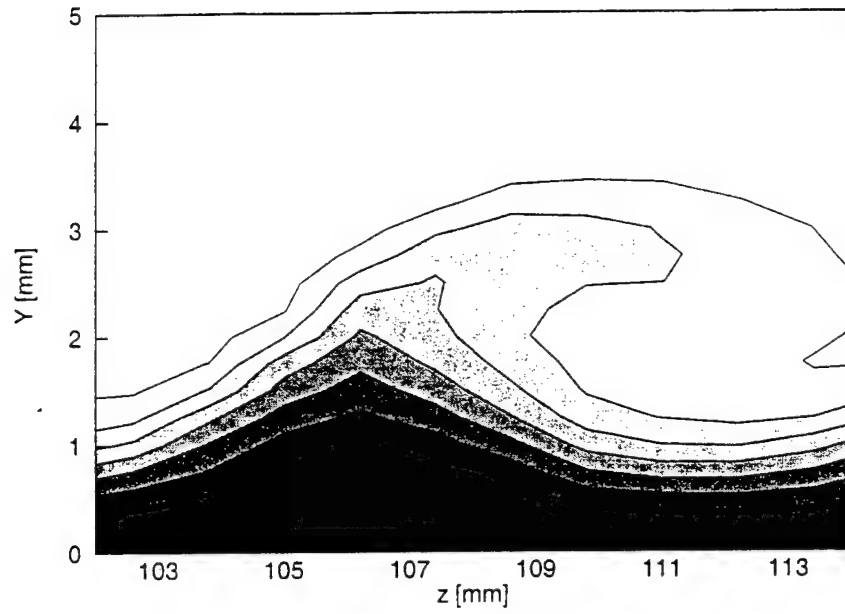Figure 71: Fluctuating-velocity spectra. $Re_c = 2.4 \times 10^6$, [18|12] roughness, $x/c = 0.45$, $z = 82$ mm.

104
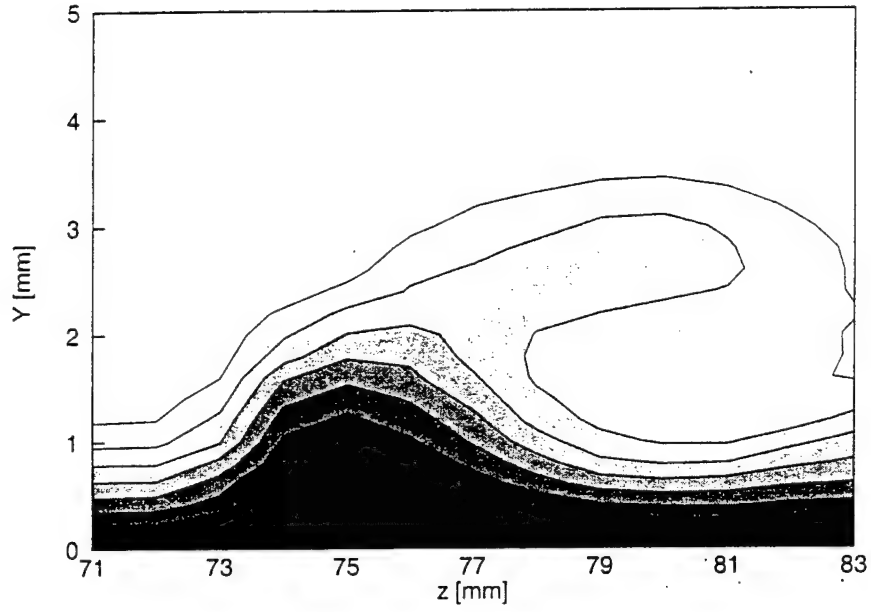
Figure 74: Mean-flow velocity contours, $Re_c = 2.4 \times 10^6$, [18|12] roughness, $x/c = 0.46$, contour lines at $U/U_{edge} = 0.10,\ 0.20,\ \ldots,\ 0.90$.
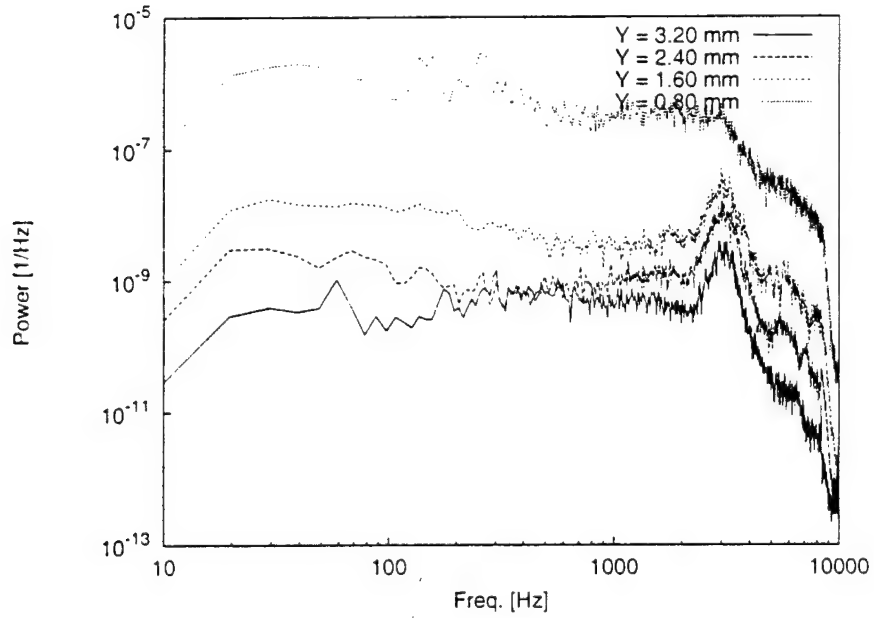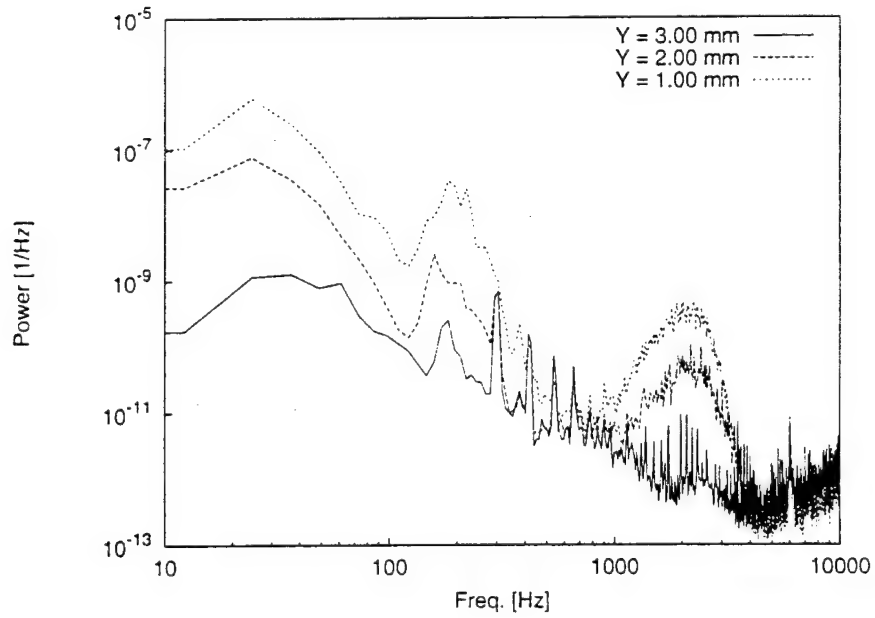

Figure 75: Fluctuating-velocity spectra, $Re_c = 2.4 \times 10^6$, [18|12] roughness, $x/c = 0.46$, $z = 72\,\mathrm{mm}$.

106
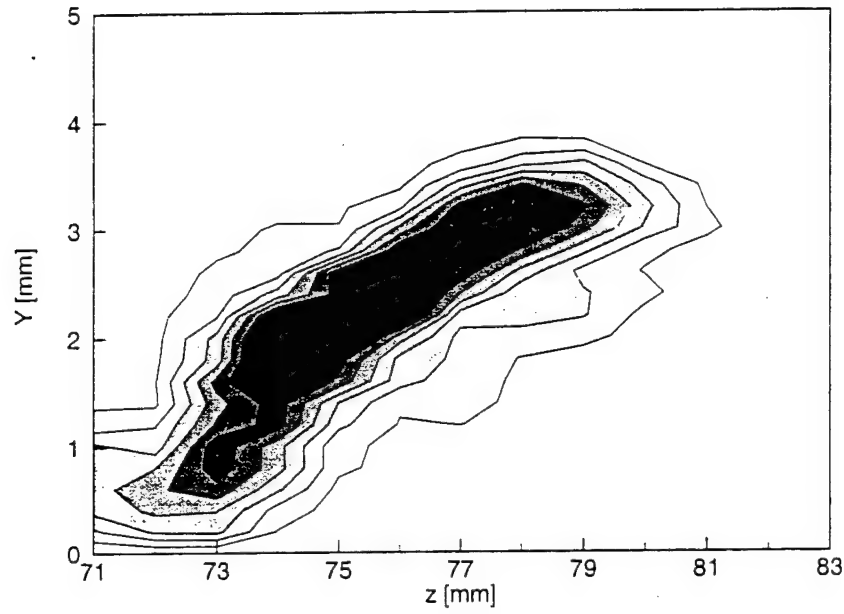
Figure 78: Total velocity-fluctuation rms distribution. $Re_c = 2.4 \times 10^6$, [18|12] roughness. $x/c = 0.46$. 20 Hz–8.0-kHz bandpass. Lines are 10% contours of the maximum rms fluctuations.
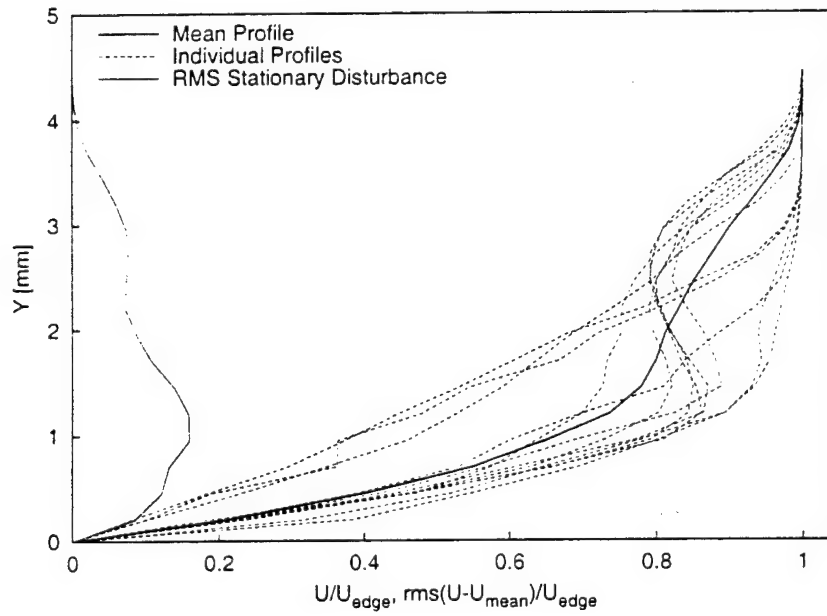
Figure 79: Mean-flow velocity profiles, $Re_c = 2.4 \times 10^6$, [18|12] roughness, $x/c = 0.47$, $z = 68$–79 mm.
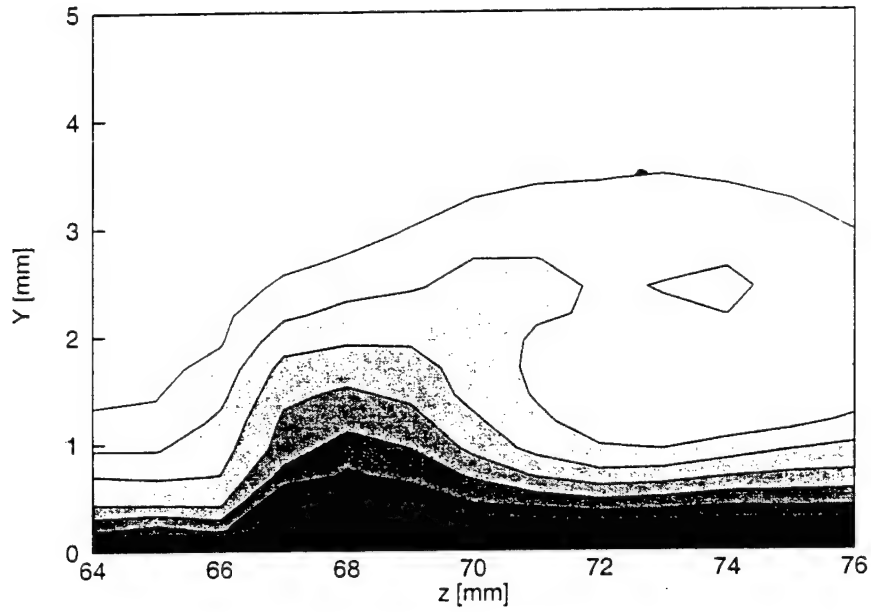
Figure 82: Mean-flow velocity contours, $Re_c = 2.4 \times 10^6$, [18|12] roughness. $x/c = 0.48$, contour lines at $U/U_{\text{edge}} = 0.10, 0.20, \ldots, 0.90$.
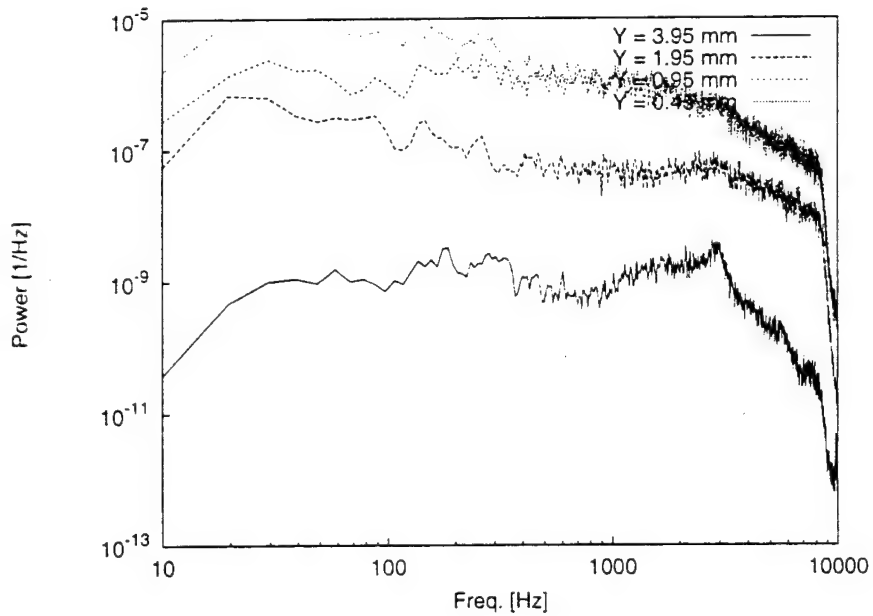
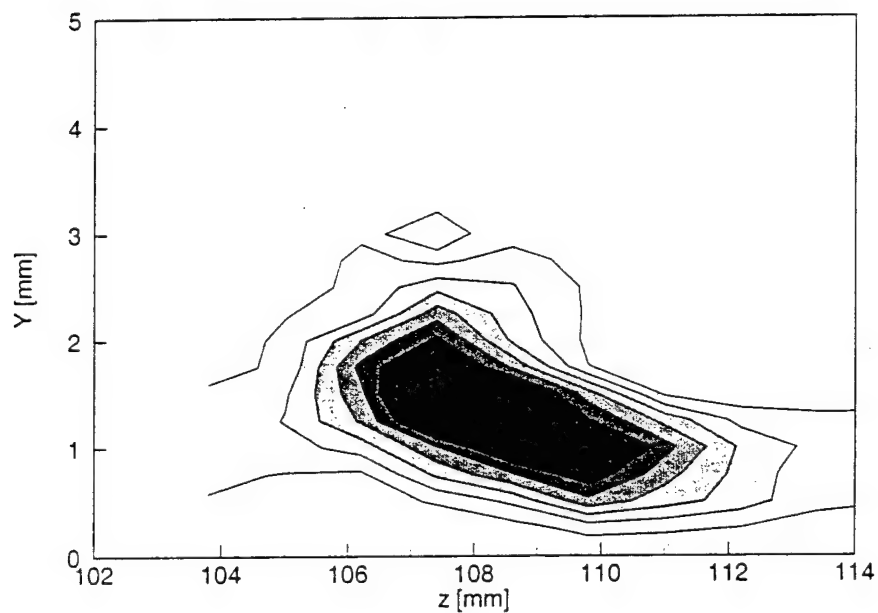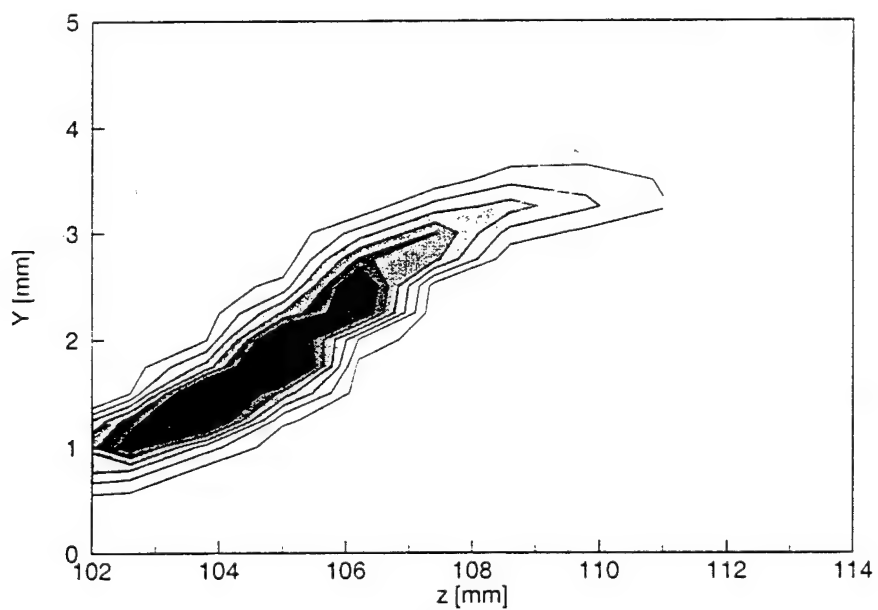Figure 83: Fluctuating-velocity spectra, $Re_c = 2.4 \times 10^6$, [18|12] roughness, $x/c = 0.48$, $z = 65$ mm.
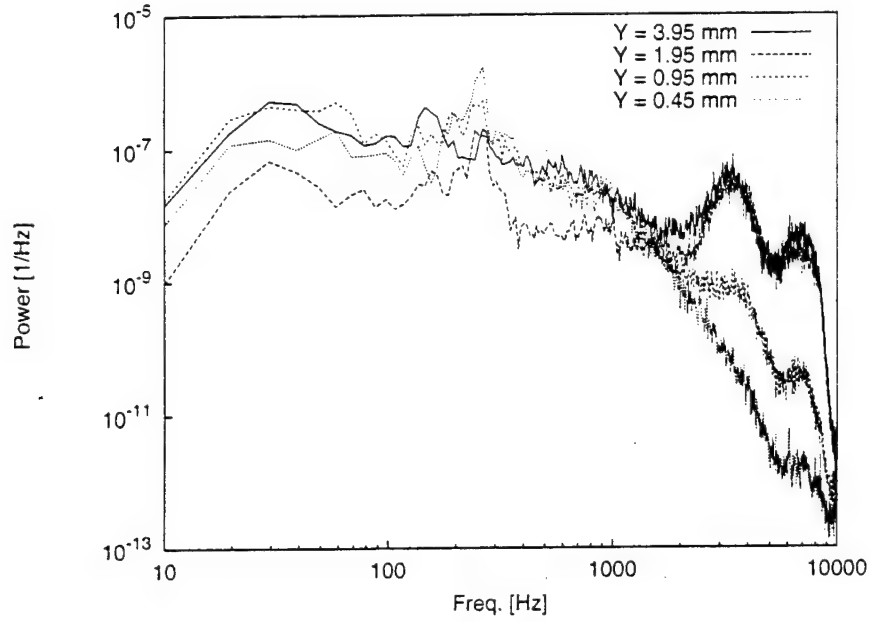
Figure 86: Fluctuating-velocity spectra, $Re_c = 2.4 \times 10^6$, [18|12] roughness, $x/c = 0.48$, $z = 74$ mm.
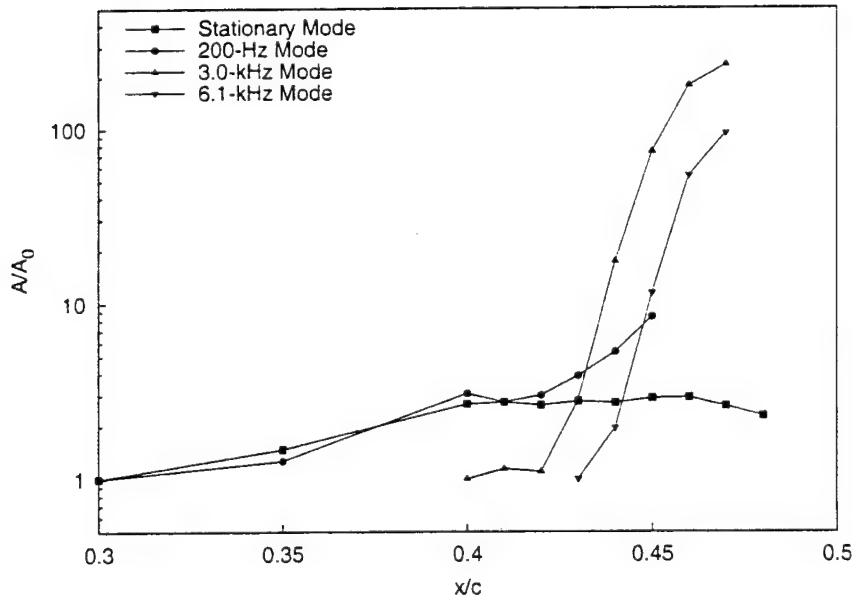
Figure 87: Velocity-fluctuation rms growth, $Re_c = 2.4 \times 10^6$, [18|12] roughness.

112
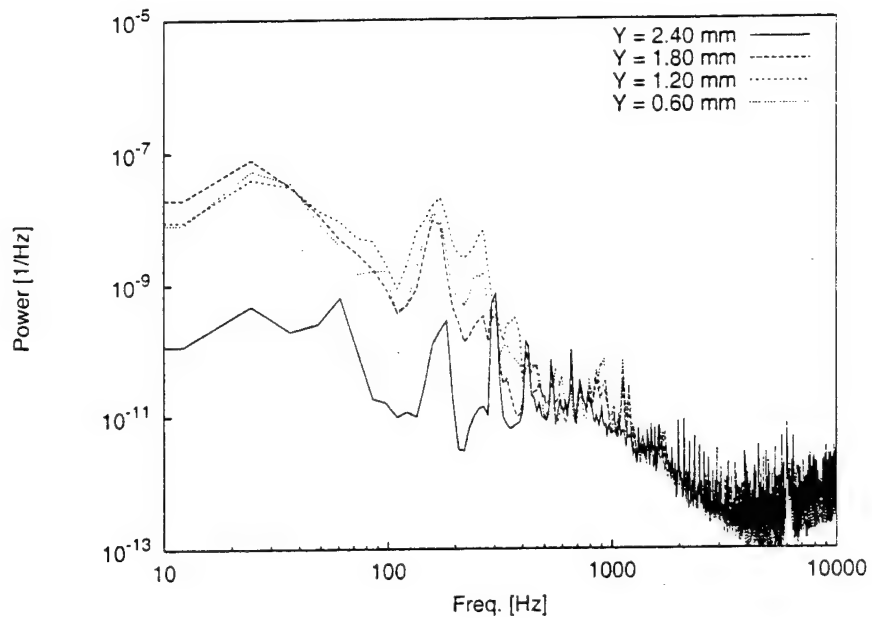
Figure 90: Fluctuating-velocity spectra, $Re_c = 2.4 \times 10^6$, [54|12] roughness. $x/c = 0.25$, $z = 122.2$ mm.
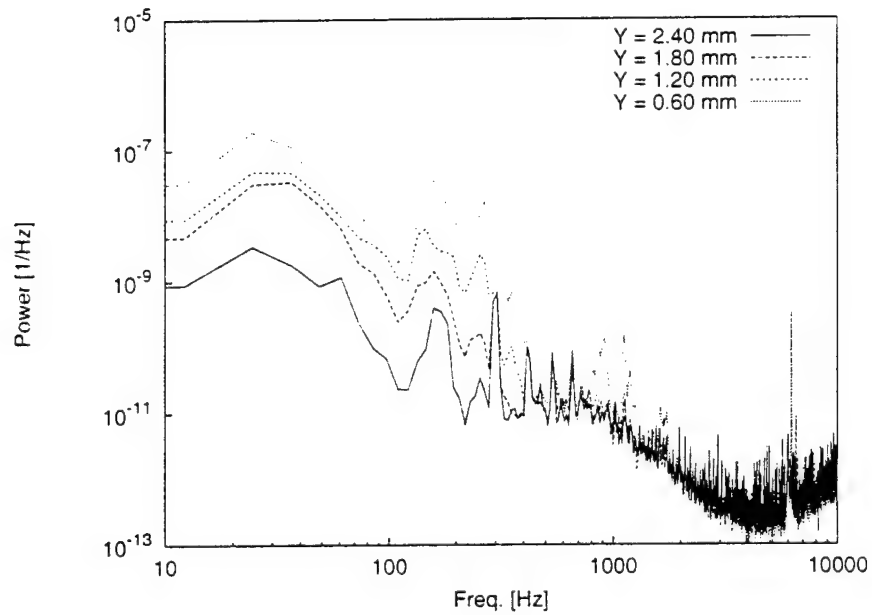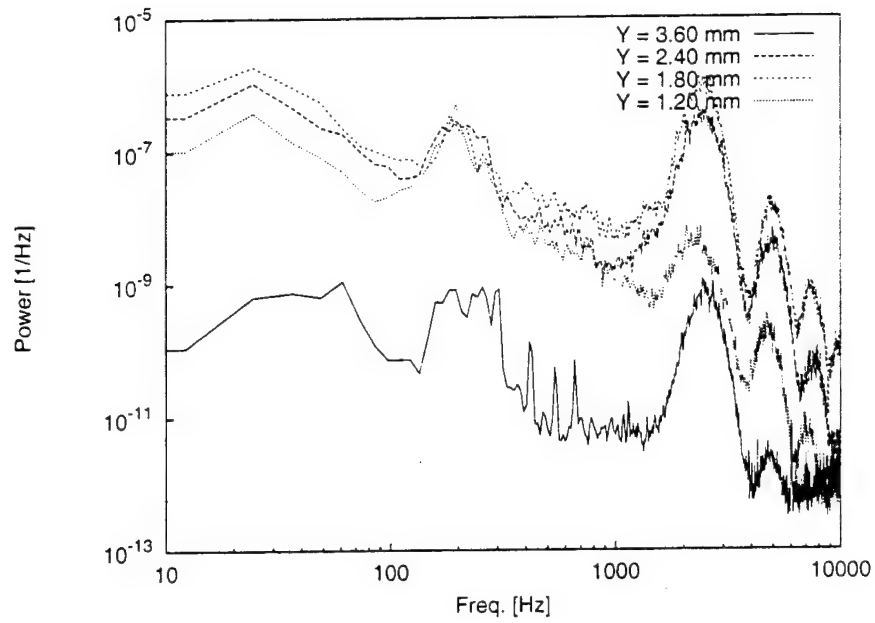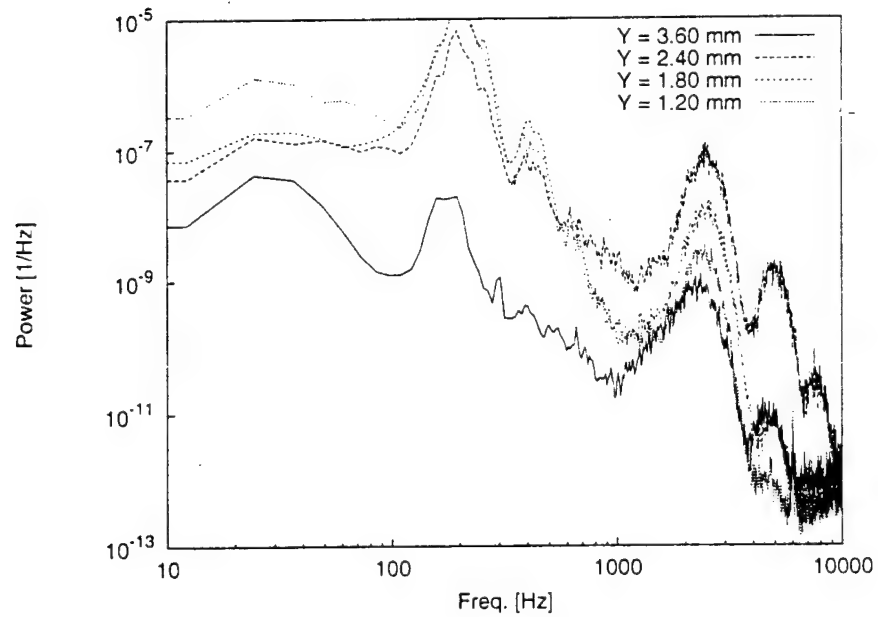

Figure 91: Fluctuating-velocity spectra, $Re_c = 2.4 \times 10^6$, [54|12] roughness, $x/c = 0.25$, $z = 125.8$ mm.
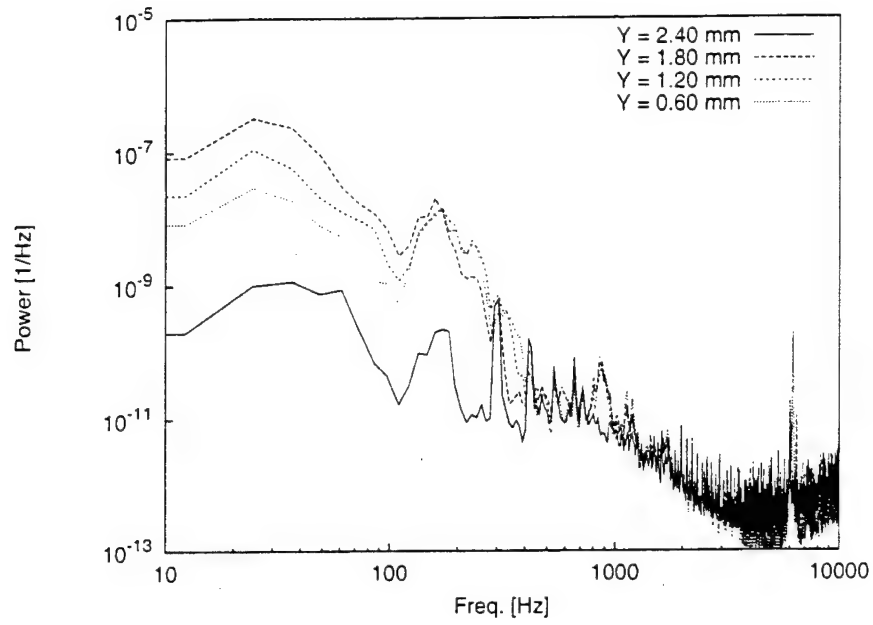
Figure 94: Fluctuating-velocity spectra. $Re_c = 2.4 \times 10^6$, [54|12] roughness, $x/c = 0.30$, $z = 110\,\text{mm}$.
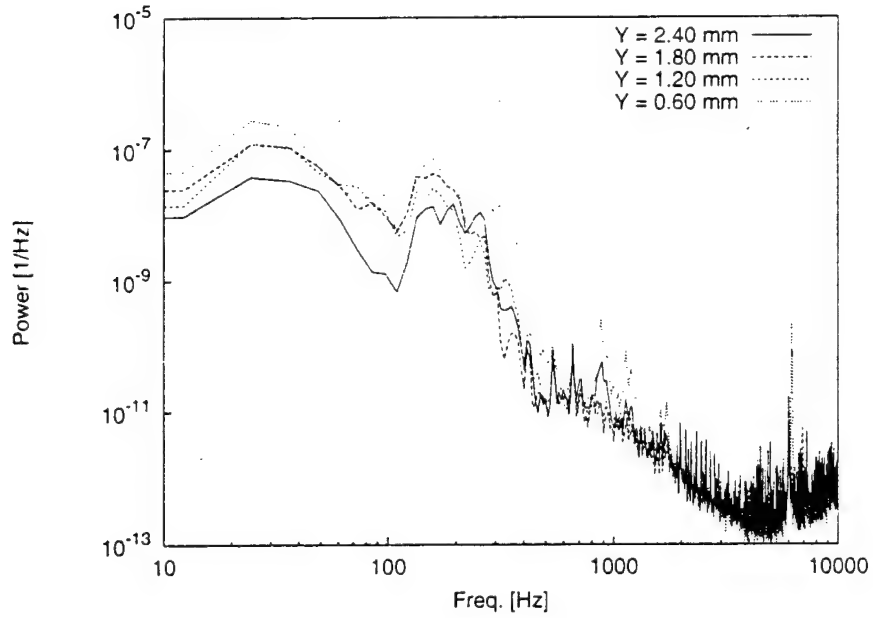
Figure 95: Fluctuating-velocity spectra. $Re_c = 2.4 \times 10^6$, [54|12] roughness, $x/c = 0.30$, $z = 113\,\text{mm}$.
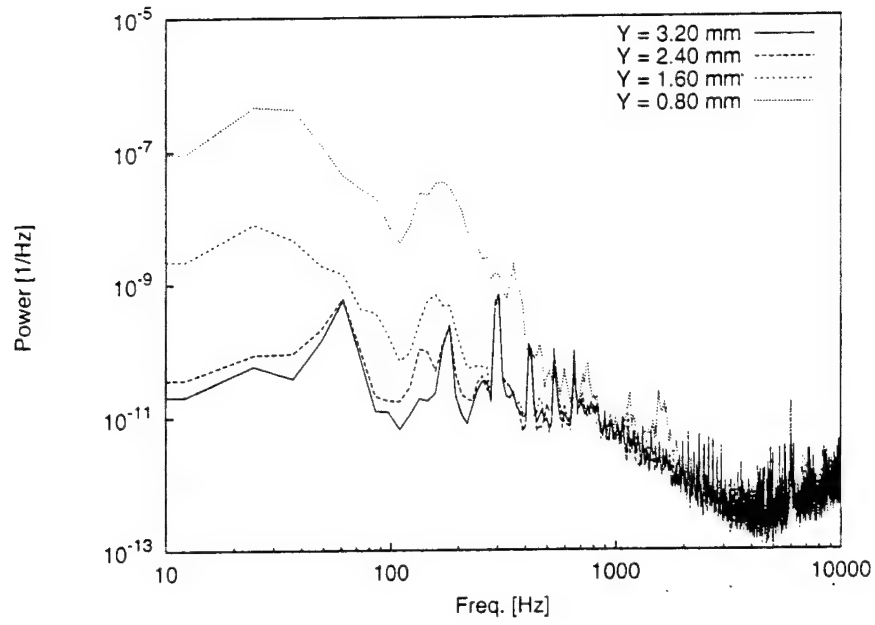
Figure 98: Fluctuating-velocity spectra, $Re_c = 2.4 \times 10^6$, [54|12] roughness, $x/c = 0.34$, $z = 101\,\mathrm{mm}$.
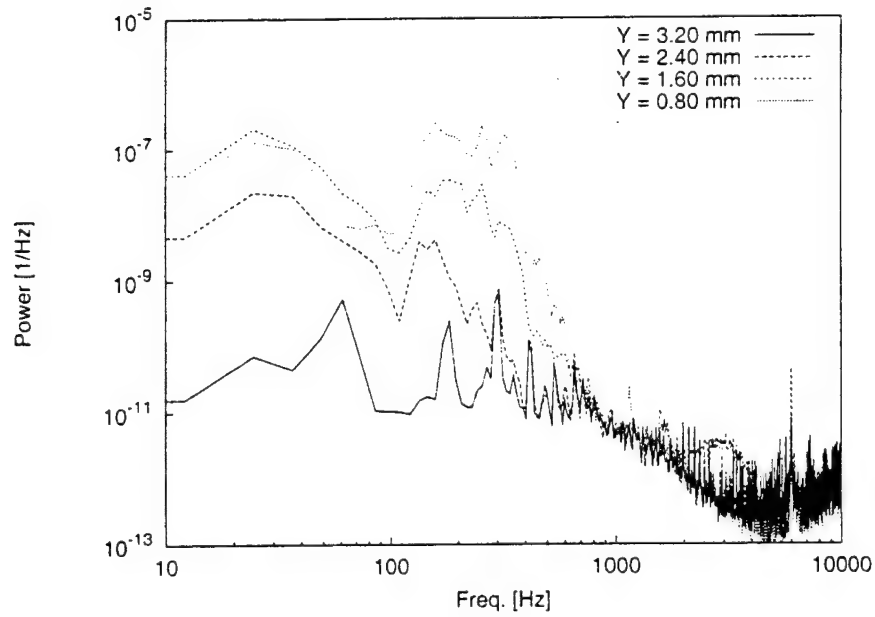
Figure 99: Fluctuating-velocity spectra. $Re_c = 2.4 \times 10^6$, [54|12] roughness, $x/c = 0.34$, $z = 104\,\mathrm{mm}$.
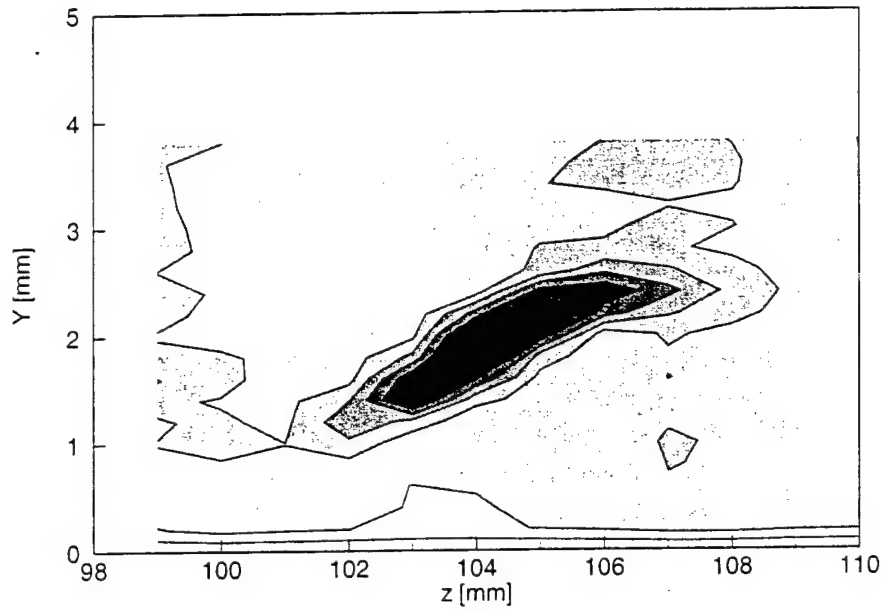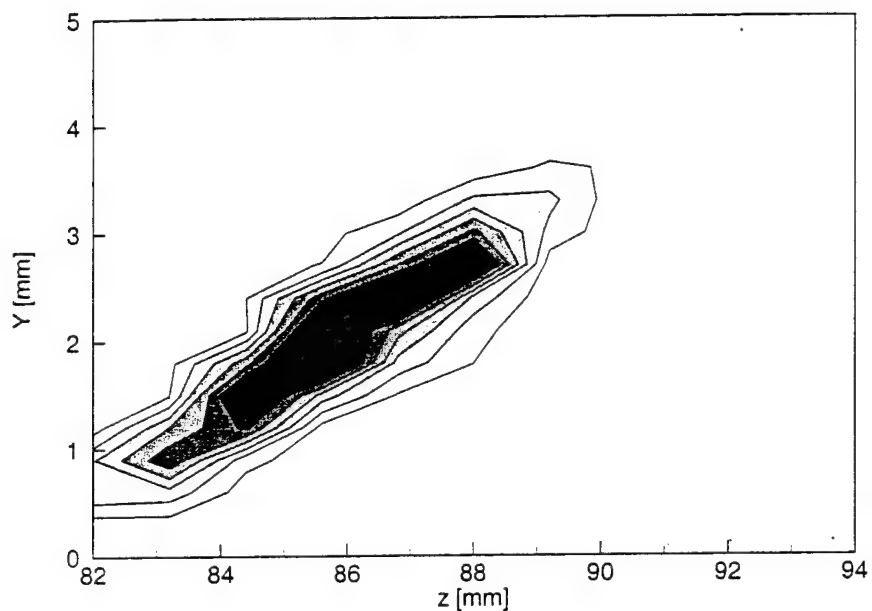
Figure 102: 3.0-kHz velocity-fluctuation rms distribution, $Re_c = 2.4 \times 10^6$, [54|12] roughness, $x/c = 0.34$. 2.9–3.1-kHz bandpass. Lines are 10% contours of the maximum in this band.
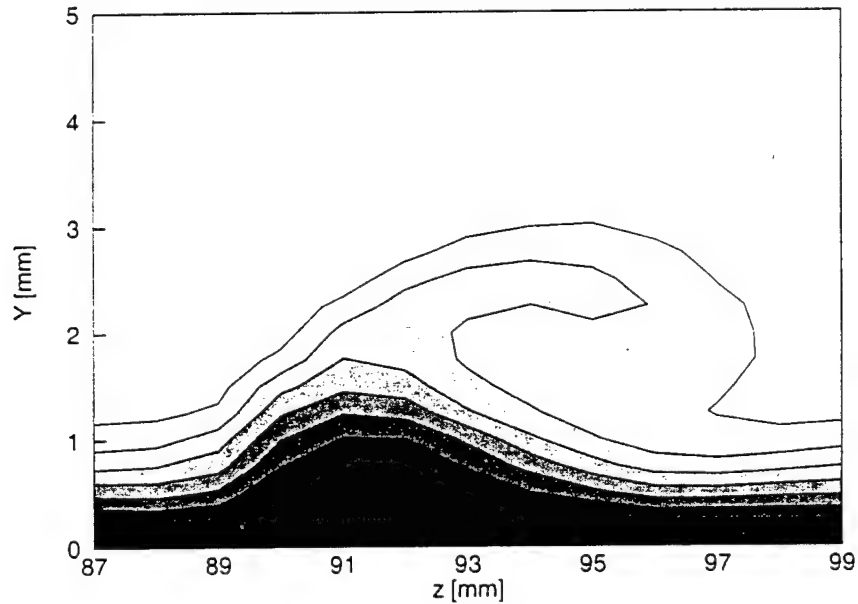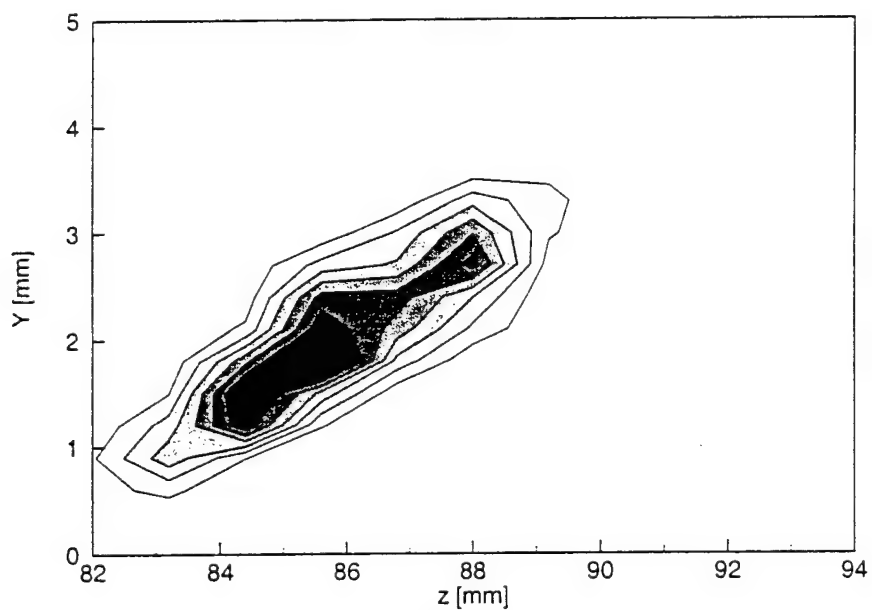

Figure 103: Mean-flow velocity contours, $Re_c = 2.4 \times 10^6$, [54|12] roughness, $x/c = 0.38$, contour lines at $U/U_{\text{edge}} = 0.10$, 0.20, ..., 0.90.
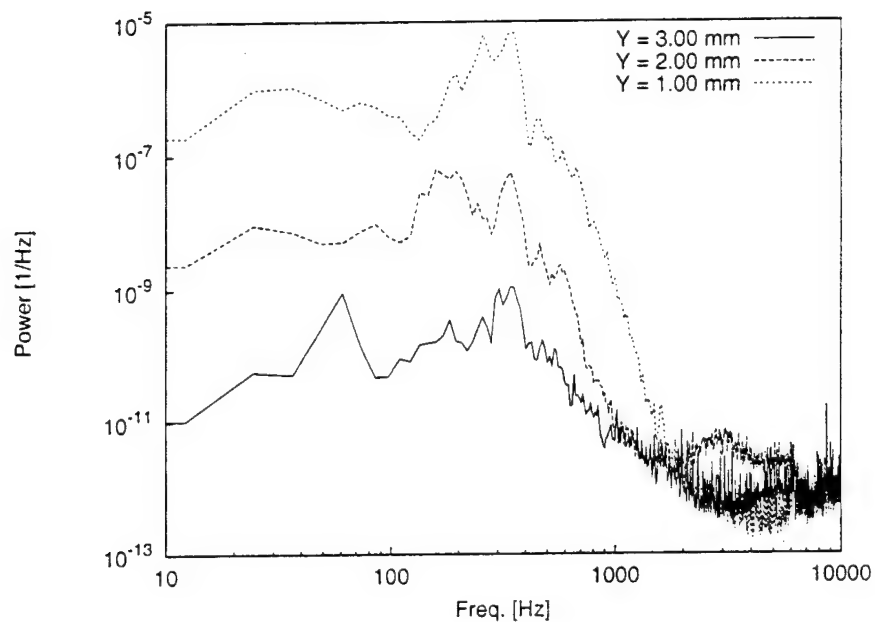
Figure 106: Fluctuating-velocity spectra. $Re_c = 2.4 \times 10^6$, [54|12] roughness, $x/c = 0.38$, $z = 94$ mm.
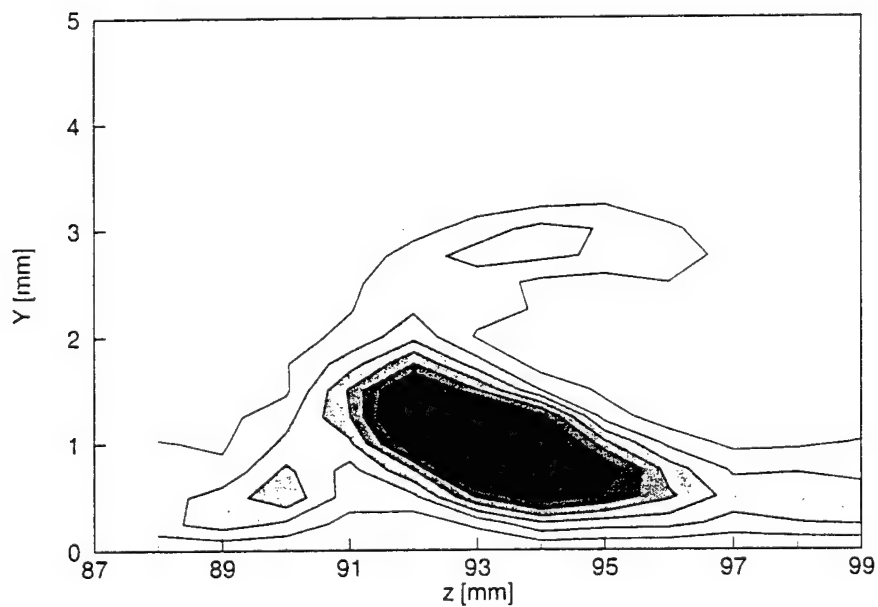
Figure 107: 200-Hz velocity-fluctuation rms distribution, $Re_c = 2.4 \times 10^6$, [54|12] roughness, $x/c = 0.38$, 100–300-Hz bandpass. Lines are 10% contours of the maximum in this band.
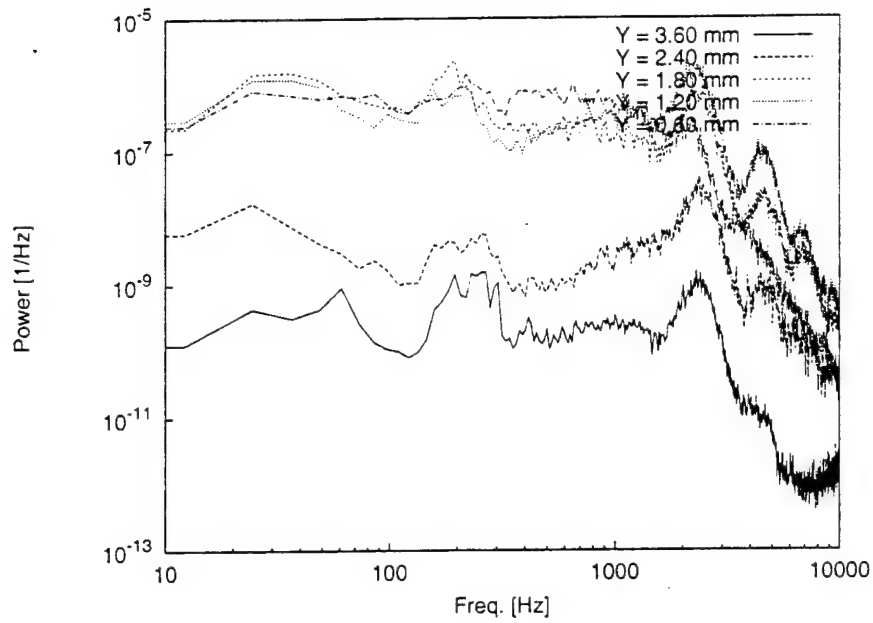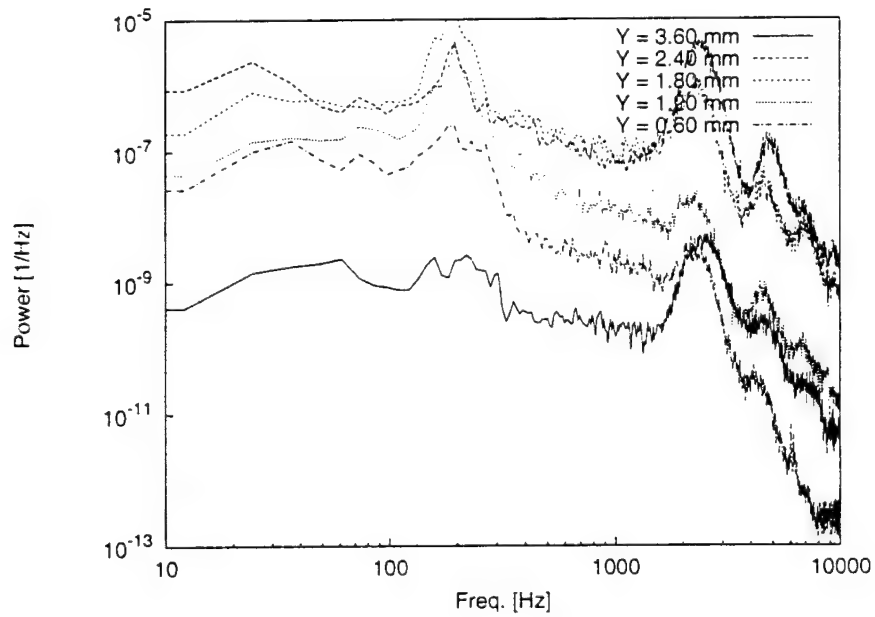
Figure 110: Mean-flow velocity contours, $Re_c = 2.4 \times 10^6$, [54|12] roughness, $x/c = 0.39$, contour lines at $U/U_{\text{edge}} = 0.10, \; 0.20, \; \ldots, \; 0.90$.

Figure 111: Fluctuating-velocity spectra, $Re_c = 2.4 \times 10^6$, [54|12] roughness, $x/c = 0.39$, $z = 86 \, \text{mm}$.

Figure 114: 200-Hz velocity-fluctuation rms distribution, $Re_c = 2.4 \times 10^6$, [54|12] roughness, $x/c = 0.39$, 100–300-Hz bandpass. Lines are 10% contours of the maximum in this band.

Figure 115: 3.0-kHz velocity-fluctuation rms distribution, $Re_c = 2.4 \times 10^6$, [54|12] roughness, $x/c = 0.39$, 2.9–3.1-kHz bandpass. Lines are 10% contours of the maximum in this band.
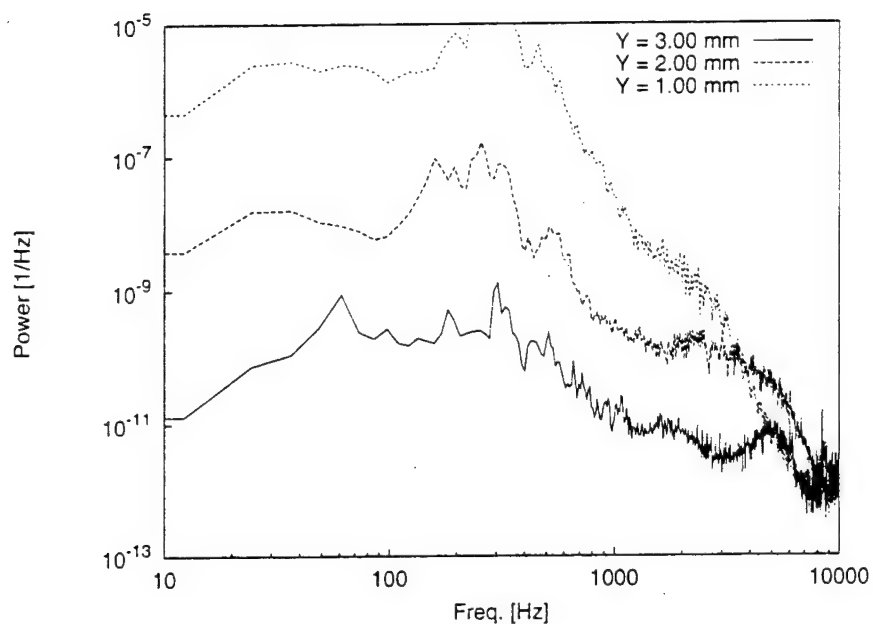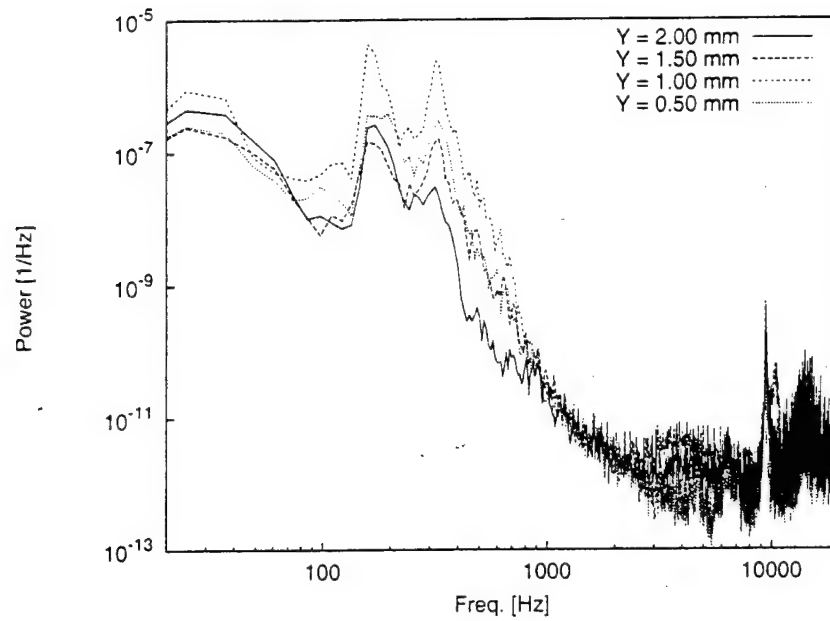
Figure 118: Fluctuating-velocity spectra, $Re_c = 2.4 \times 10^6$, [54|12] roughness, $x/c = 0.40$, $z = 82$ mm.

Figure 119: Fluctuating-velocity spectra, $Re_c = 2.4 \times 10^6$, [54|12] roughness, $x/c = 0.40$, $z = 85$ mm.

128

Figure 122: Velocity-fluctuation rms growth, $Re_c = 2.4 \times 10^6$, [54|12] roughness.
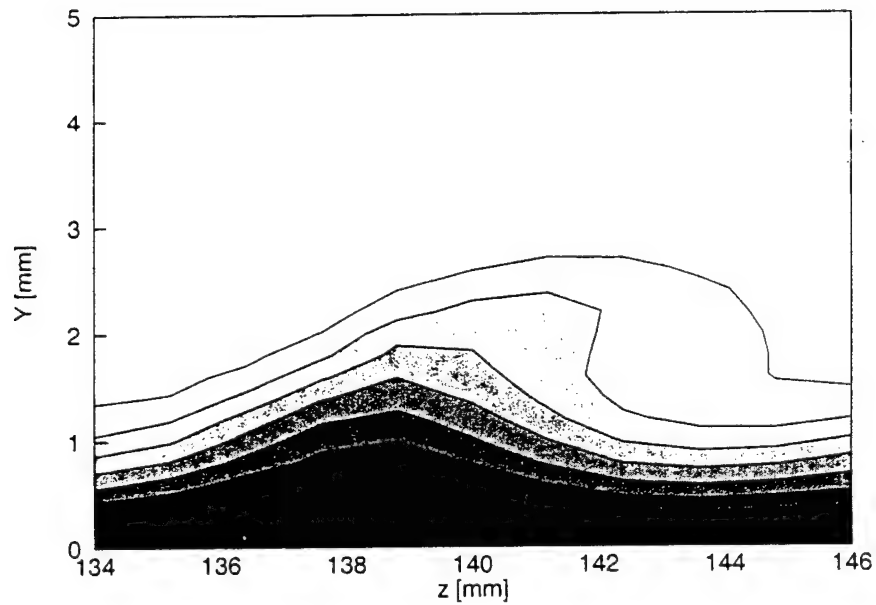
Figure 123: Mean-flow velocity contours, $Re_c = 2.0 \times 10^6$, [54|12] roughness, $x/c = 0.40$, contour lines at $U/U_{\text{edge}} = 0.10, 0.20, \ldots, 0.90$.

Figure 126: Fluctuating-velocity spectra, $Re_c = 2.0 \times 10^6$, [54|12] roughness, $x/c = 0.40$, $z = 141.2$ mm.
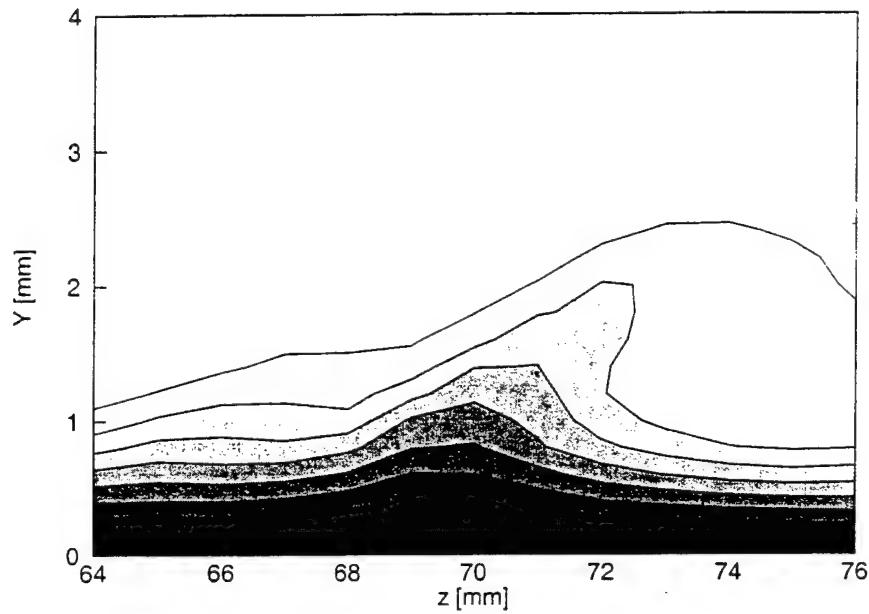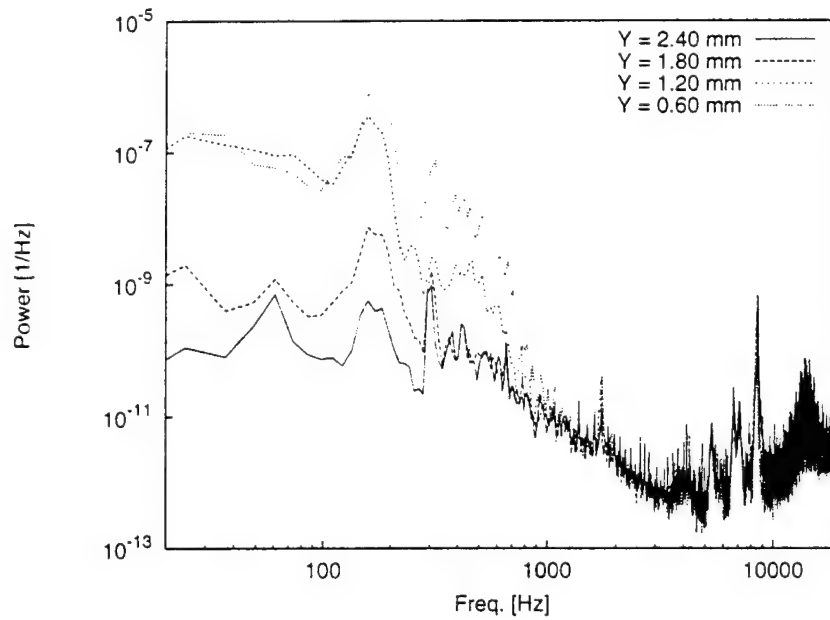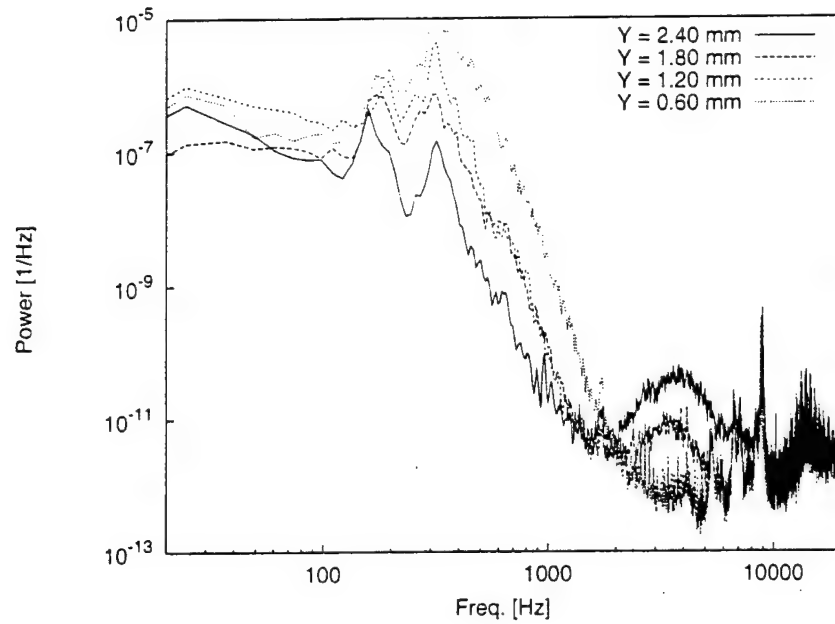

Figure 127: 200-Hz velocity-fluctuation rms distribution, $Re_c = 2.0 \times 10^6$, [54|12] roughness, $x/c = 0.40$, 100–300-Hz bandpass. Lines are 10% contours of the maximum in this band.
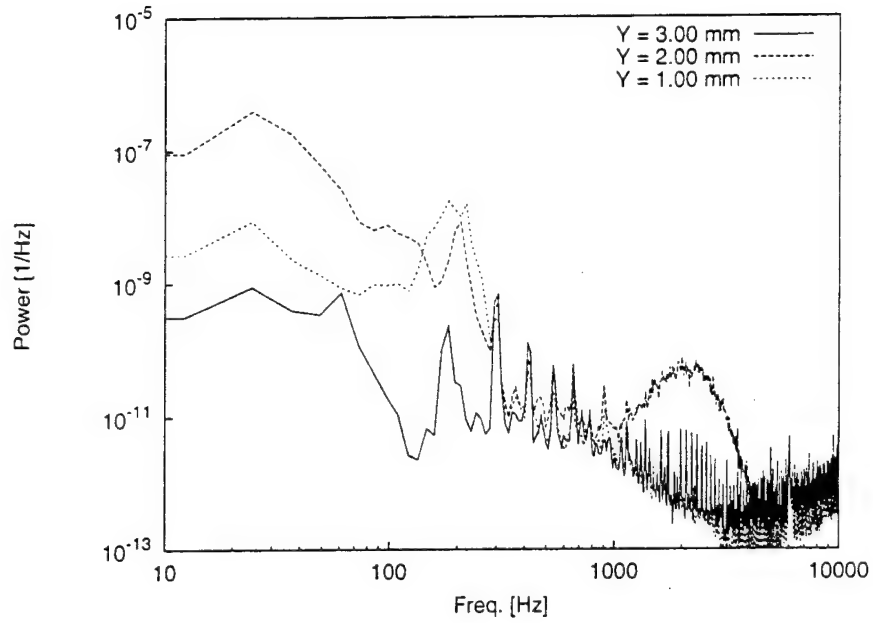
Figure 130: Fluctuating-velocity spectra, $Re_c = 2.0 \times 10^6$, [54|12] roughness, $x/c = 0.46$, $z = 118.8\,\text{mm}$.

Figure 131: Fluctuating-velocity spectra, $Re_c = 2.0 \times 10^6$, [54|12] roughness. $x/c = 0.46$, $z = 121.2\,\text{mm}$.

Figure 134: Mean-flow velocity contours, $Re_c = 2.0 \times 10^6$, [54|12] roughness, $x/c = 0.50$, contour lines at $U/U_{\text{edge}} = 0.10, 0.20, \ldots, 0.90$.

Figure 135: Fluctuating-velocity spectra, $Re_c = 2.0 \times 10^6$, [54|12] roughness, $x/c = 0.50$, $z = 103.8\,\text{mm}$.
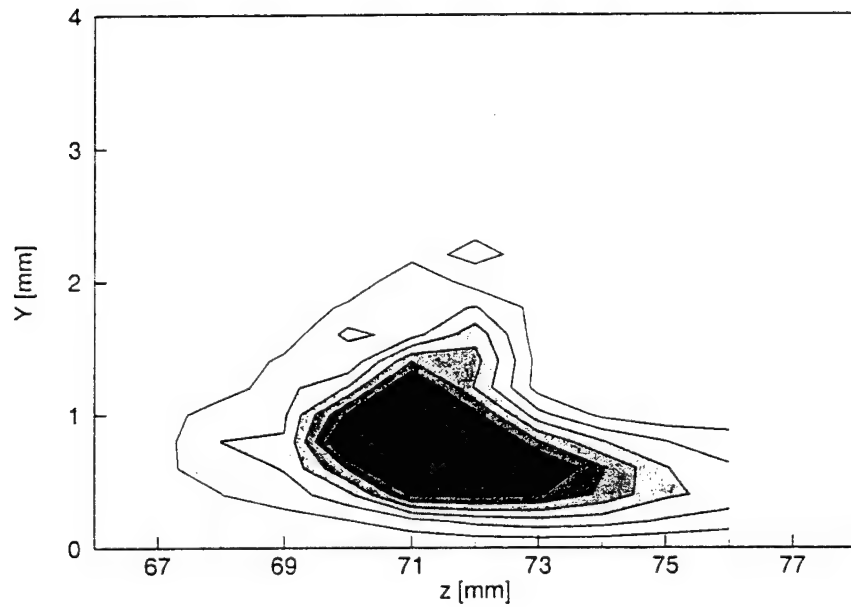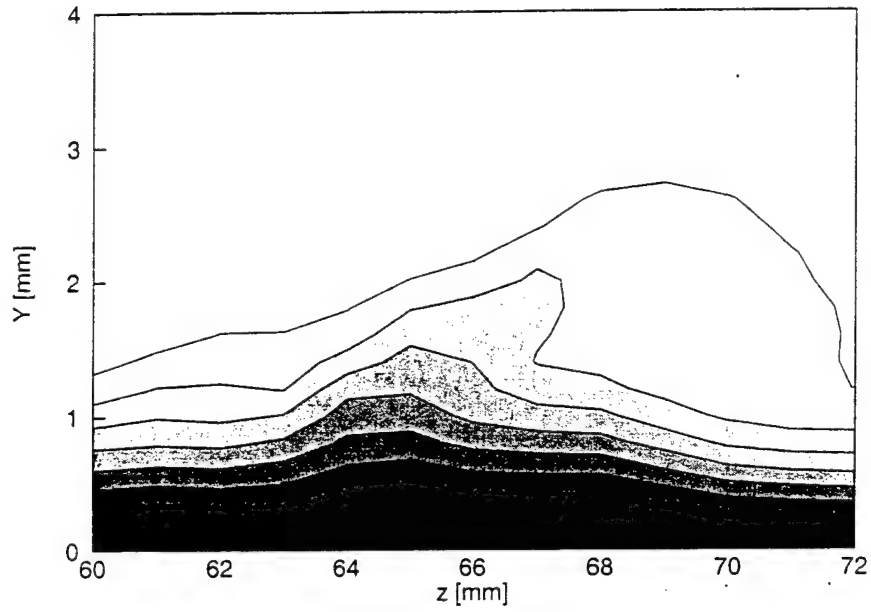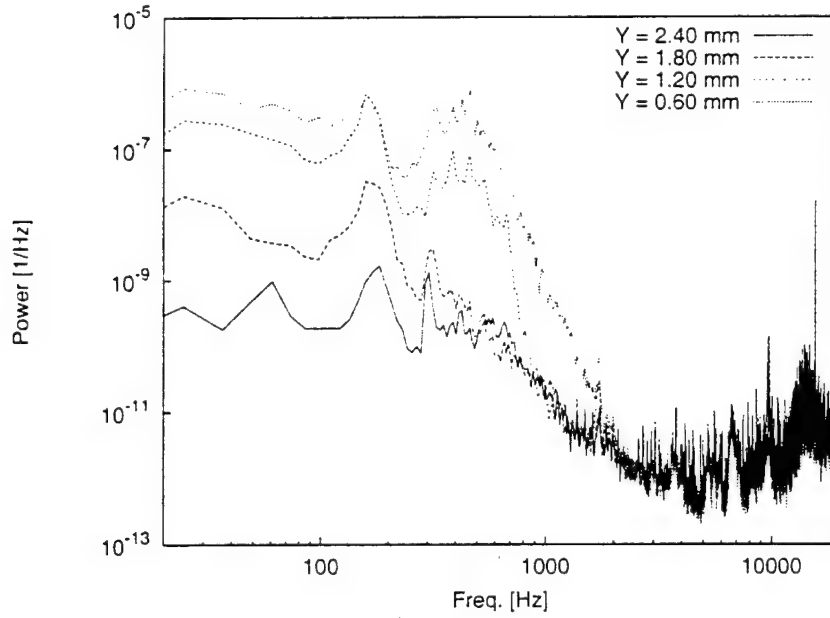
Figure 138: 200-Hz velocity-fluctuation rms distribution, $Re_c = 2.0 \times 10^6$, [54|12] roughness, $x/c = 0.50$. 100–300-Hz bandpass. Lines are 10% contours of the maximum in this band.

Figure 139: 2.4-kHz velocity-fluctuation rms distribution, $Re_c = 2.0 \times 10^6$, [54|12] roughness, $x/c = 0.50$. 2.3–2.5-kHz bandpass. Lines are 10% contours of the maximum in this band.

Figure 142: Fluctuating-velocity spectra. $Re_c = 2.0 \times 10^6$, [54|12] roughness, $x/c = 0.55$, $z = 85.6$ mm.
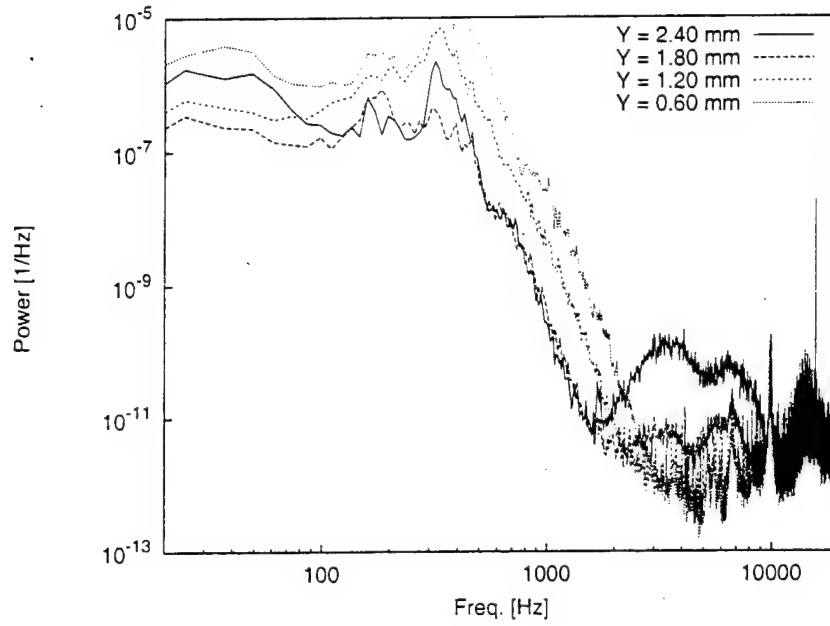

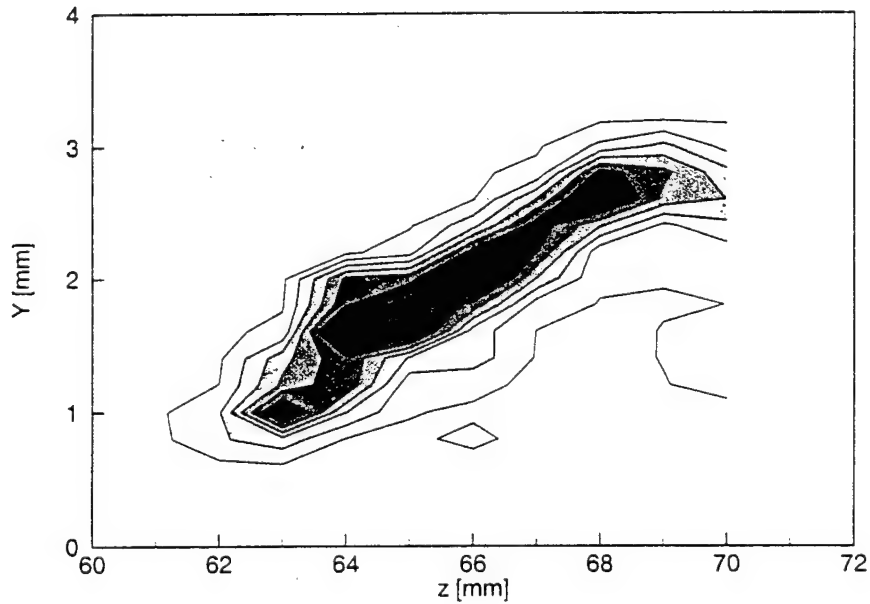Figure 143: Fluctuating-velocity spectra, $Re_c = 2.0 \times 10^6$, [54|12] roughness, $x/c = 0.55$, $z = 88.0$ mm.

Figure 146: 2.4-kHz velocity-fluctuation rms distribution, $Re_c = 2.0 \times 10^6$, [54|12] roughness, $x/c = 0.55$, 2.3–2.5-kHz bandpass. Lines are 10% contours of the maximum in this band.

Figure 147: 4.9-kHz velocity-fluctuation rms distribution, $Re_c = 2.0 \times 10^6$, [54|12] roughness, $x/c = 0.55$, 4.8–5.0-kHz bandpass. Lines are 10% contours of the maximum in this band.
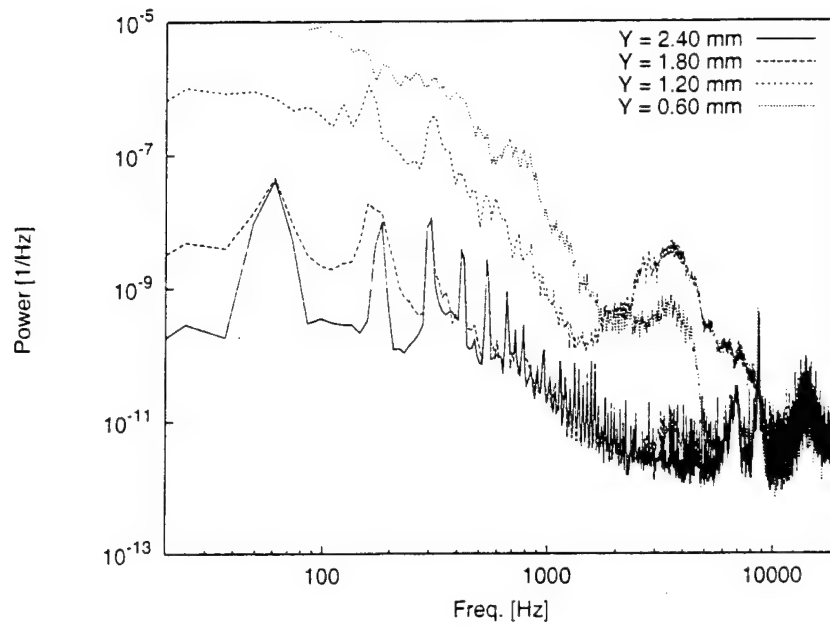
Figure 150: Fluctuating-velocity spectra, $Re_c = 2.0 \times 10^6$, [54|12] roughness, $x/c = 0.57$, $z = 77.8$ mm.
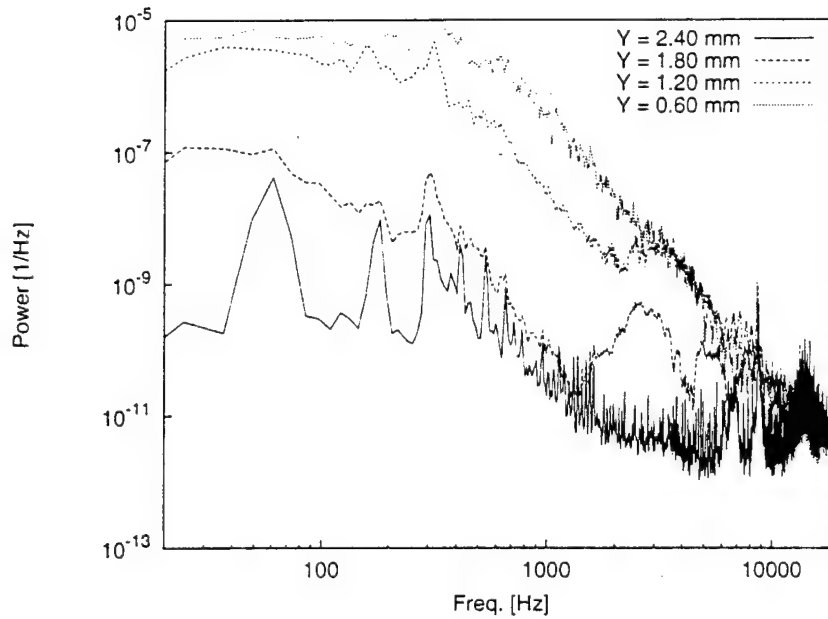

Figure 151: Fluctuating-velocity spectra, $Re_c = 2.0 \times 10^6$, [54|12] roughness, $x/c = 0.57$, $z = 80.2$ mm.
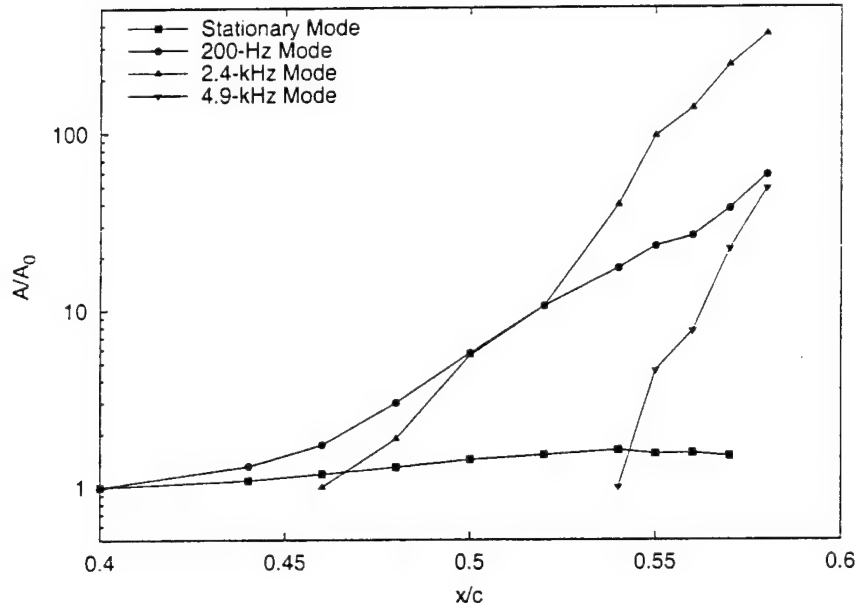
Figure 154: Velocity-fluctuation rms growth, $Re_c = 2.0 \times 10^6$, [54|12] roughness.
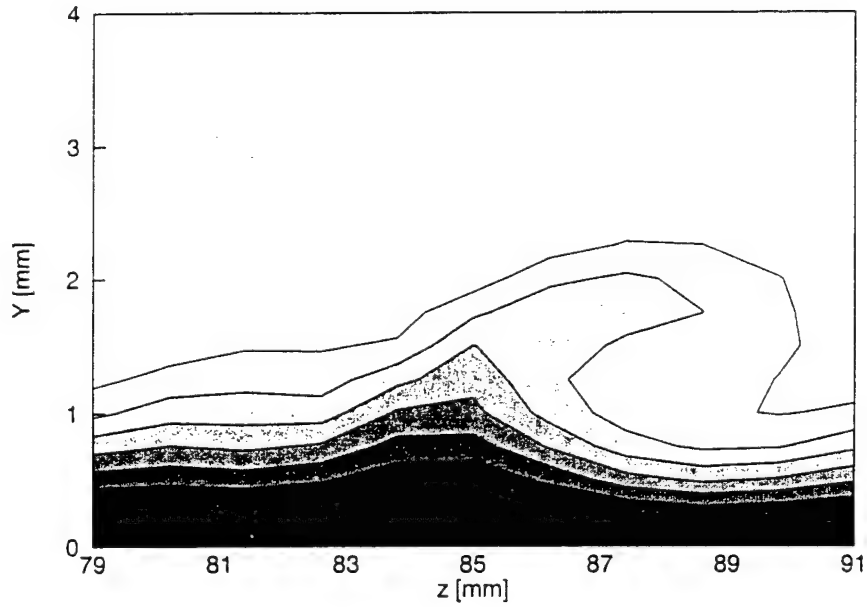
Figure 155: Mean-flow velocity contours, $Re_c = 2.8 \times 10^6$, [54|12] roughness, $x/c = 0.30$, contour lines at $U/U_{\text{edge}} = 0.10,\ 0.20,\ \ldots,\ 0.90$.

Figure 158: Fluctuating-velocity spectra, $Re_c = 2.8 \times 10^6$, [54|12] roughness, $x/c = 0.30$, $z = 85.0$ mm.
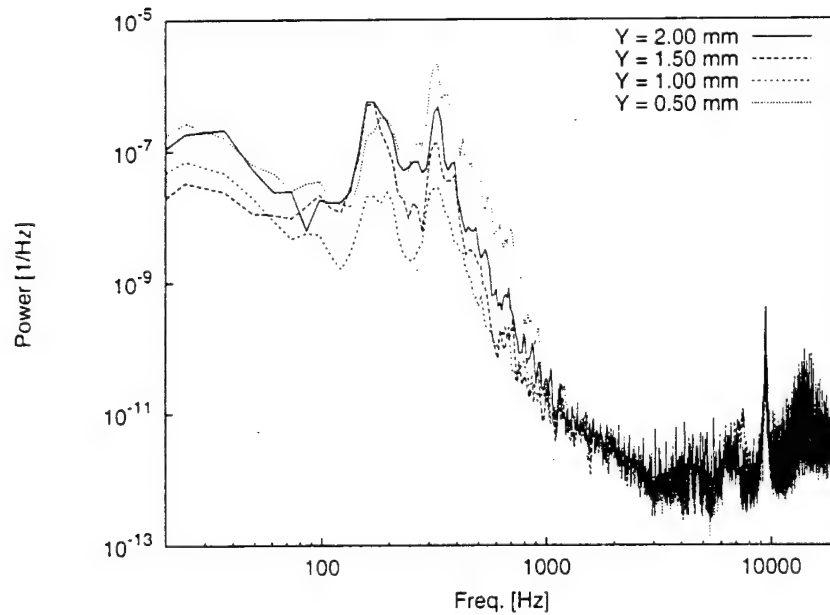
Figure 159: Fluctuating-velocity spectra, $Re_c = 2.8 \times 10^6$, [54|12] roughness, $x/c = 0.30$, $z = 87.4$ mm.

Figure 162: Mean-flow velocity contours, $Re_c = 2.8 \times 10^6$, [54|12] roughness, $x/c = 0.35$, contour lines at $U/U_{\text{edge}} = 0.10, 0.20, \ldots, 0.90$.

Figure 163: Fluctuating-velocity spectra, $Re_c = 2.8 \times 10^6$, [54|12] roughness, $x/c = 0.35$, $z = 66\,\text{mm}$.

150

Figure 166: Fluctuating-velocity spectra. $Re_c = 2.8 \times 10^6$, [54|12] roughness, $x/c = 0.35$, $z = 72$ mm.

Figure 167: 300-Hz velocity-fluctuation rms distribution, $Re_c = 2.8 \times 10^6$, [54|12] roughness, $x/c = 0.35$, 200–400-Hz bandpass. Lines are 10% contours of the maximum in this band.

Figure 170: Mean-flow velocity contours, $Re_c = 2.8 \times 10^6$, [54|12] roughness, $x/c = 0.37$, contour lines at $U/U_{\mathrm{edge}} = 0.10,\ 0.20,\ \ldots,\ 0.90$.

Figure 171: Fluctuating-velocity spectra. $Re_c = 2.8 \times 10^6$, [54|12] roughness, $x/c = 0.37$, $z = 61\,\mathrm{mm}$.

154

Figure 174: Fluctuating-velocity spectra, $Re_c = 2.8 \times 10^6$, [54|12] roughness, $x/c = 0.37$, $z = 67$ mm.

Figure 175: 3.6-kHz velocity-fluctuation rms distribution, $Re_c = 2.8 \times 10^6$, [54|12] roughness, $x/c = 0.37$, 3.5 kHz–3.7-kHz bandpass. Lines are 10% contours of the maximum in this band.

Figure 178: Fluctuating-velocity spectra, $Re_c = 2.8 \times 10^6$, [54|12] roughness, $x/c = 0.385$, $z = 58\,\text{mm}$.

Figure 179: Fluctuating-velocity spectra, $Re_c = 2.8 \times 10^6$, [54|12] roughness, $x/c = 0.385$, $z = 60\,\text{mm}$.
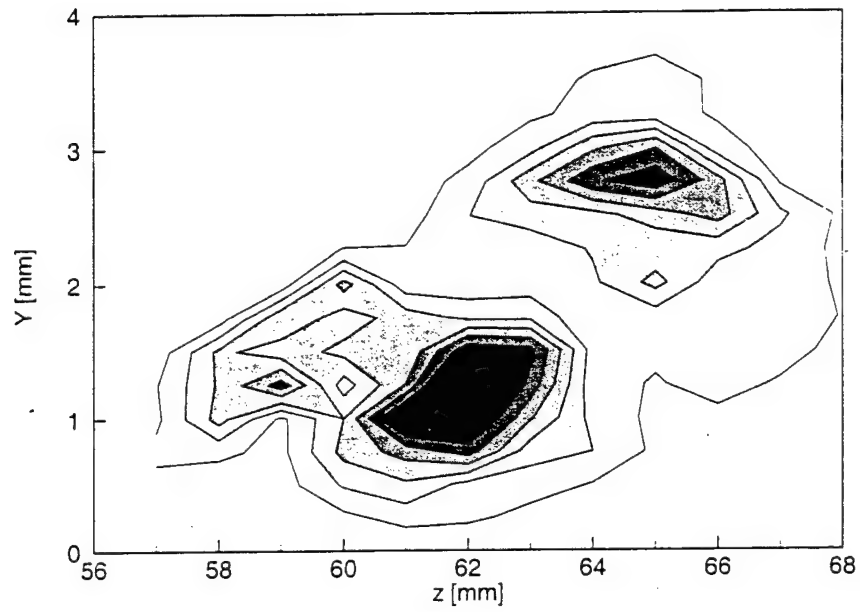
Figure 182: Total velocity-fluctuation rms distribution, $Re_c = 2.8 \times 10^6$, [54|12] roughness, $x/c = 0.385$. 20-Hz-12.0-kHz bandpass. Lines are 10% contours of the maximum rms fluctuations.
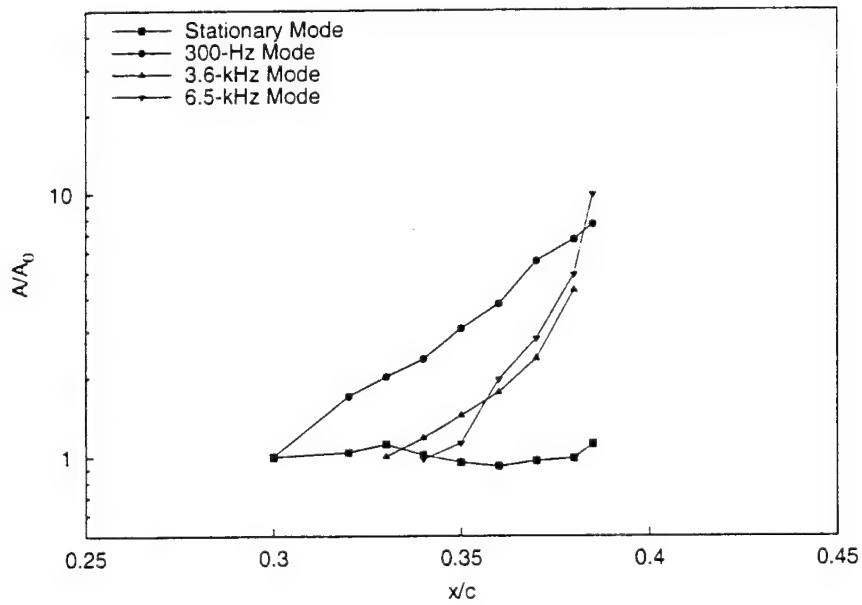
Figure 183: Velocity-fluctuation rms growth, $Re_c = 2.8 \times 10^6$, [54|12] roughness.
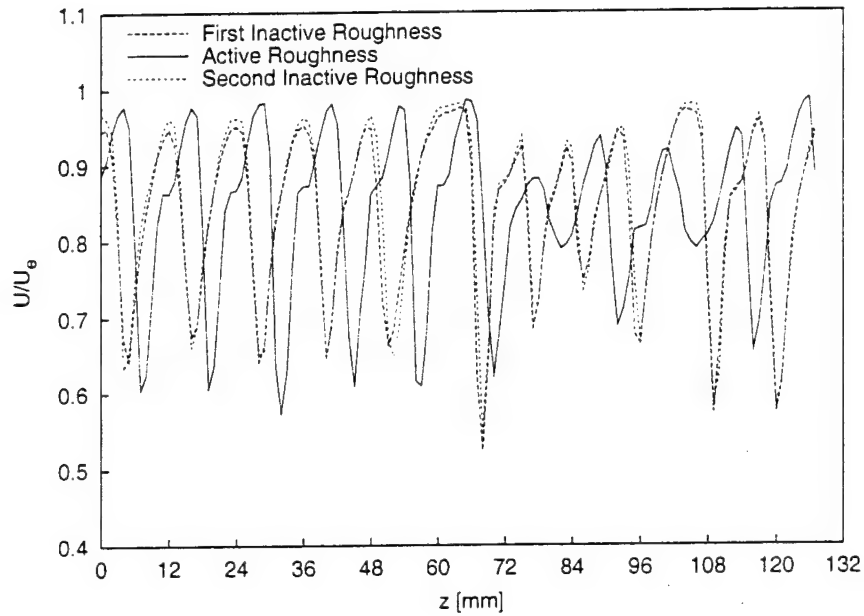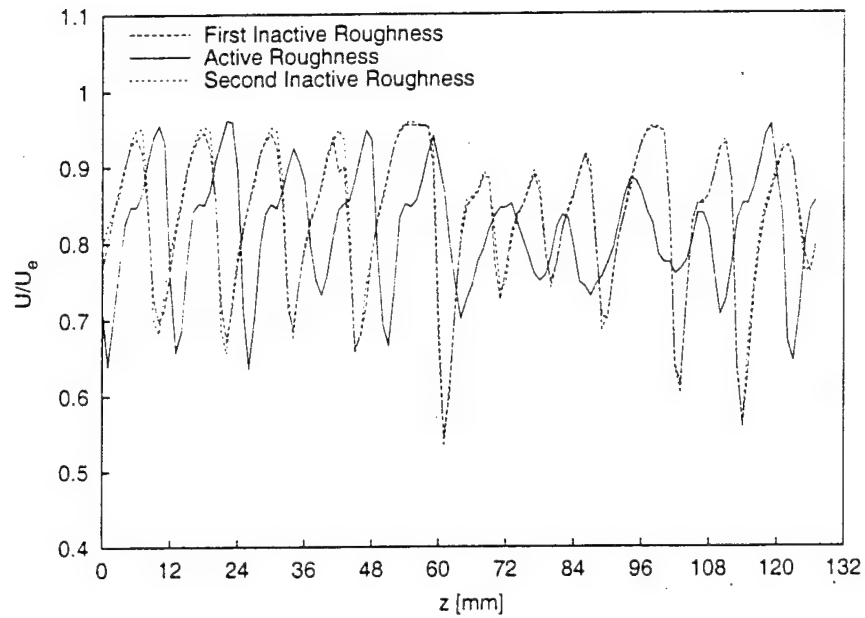
Figure 186: Spanwise mean-flow hotwire scan with and without activated 12-mm-spaced artificial roughness, $Re_c = 2.4 \times 10^6$, $x/c = 0.43$, $Y = 2.0$ mm.
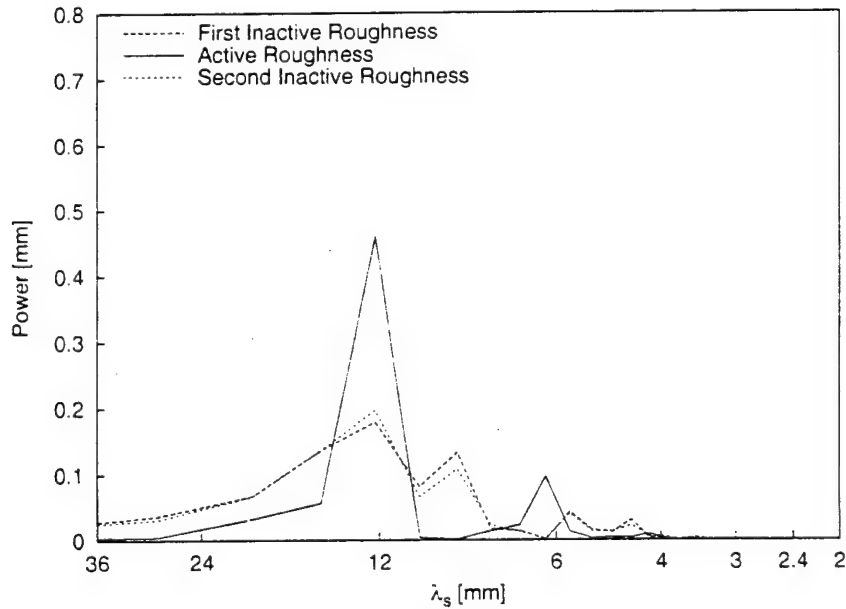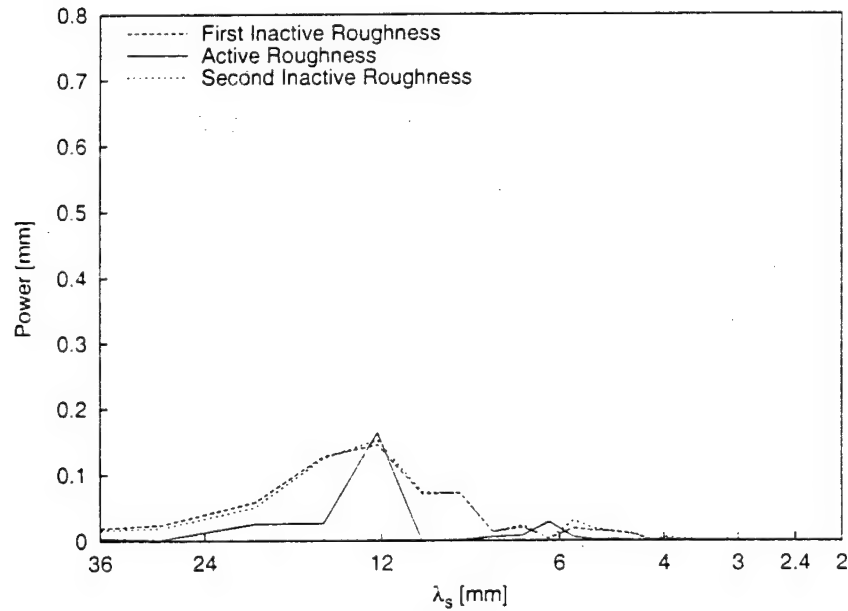

Figure 187: Power spectral density of the spanwise mean-flow hotwire scan with and without activated 12-mm-spaced artificial roughness. $Re_c = 2.4 \times 10^6$, $x/c = 0.43$, $Y = 2.0$ mm.
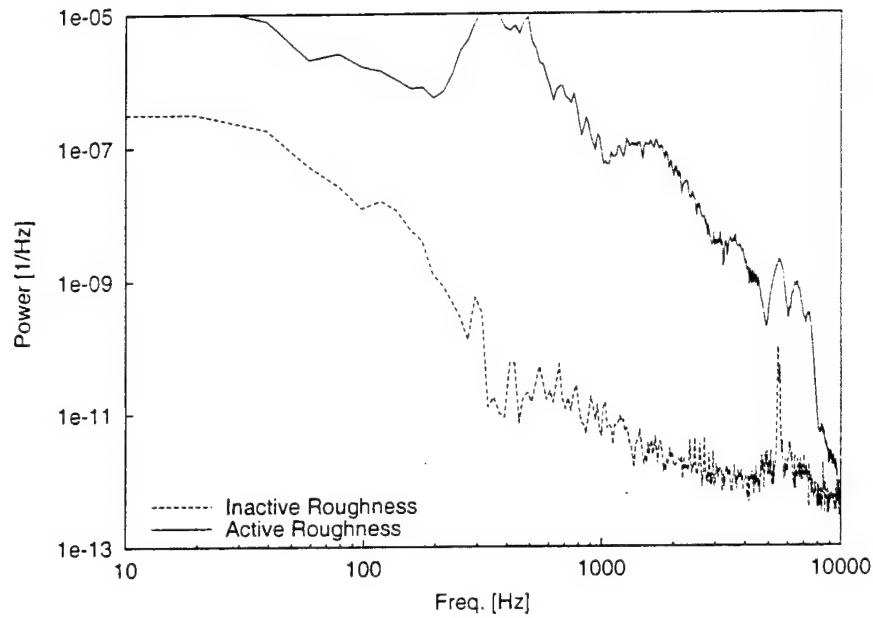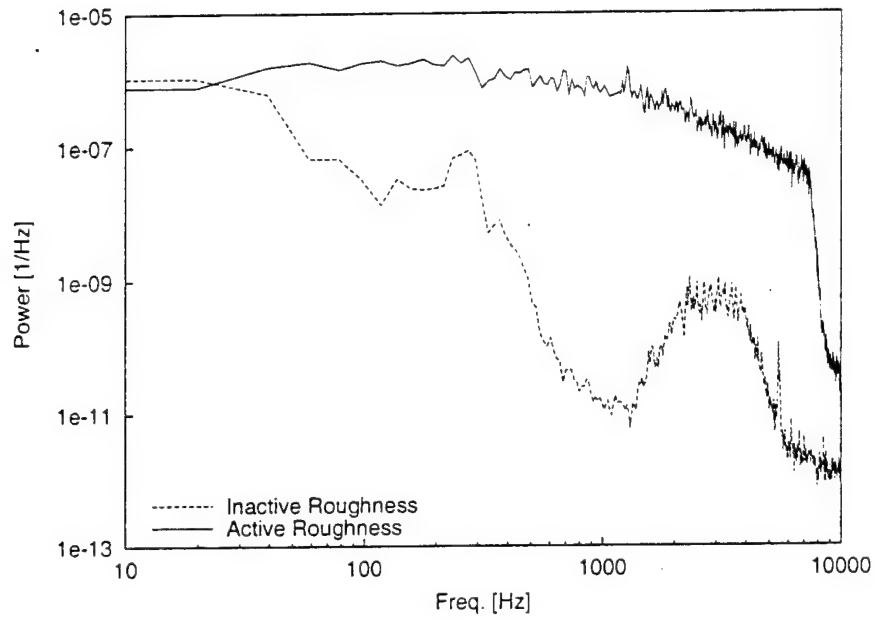
Figure 190: Fluctuating-velocity spectral density with and without activated 12-mm-spaced artificial roughness, $Re_c = 2.4 \times 10^6$, $x/c = 0.43$, $Y = 2.0$ mm, $z = 31$ mm.
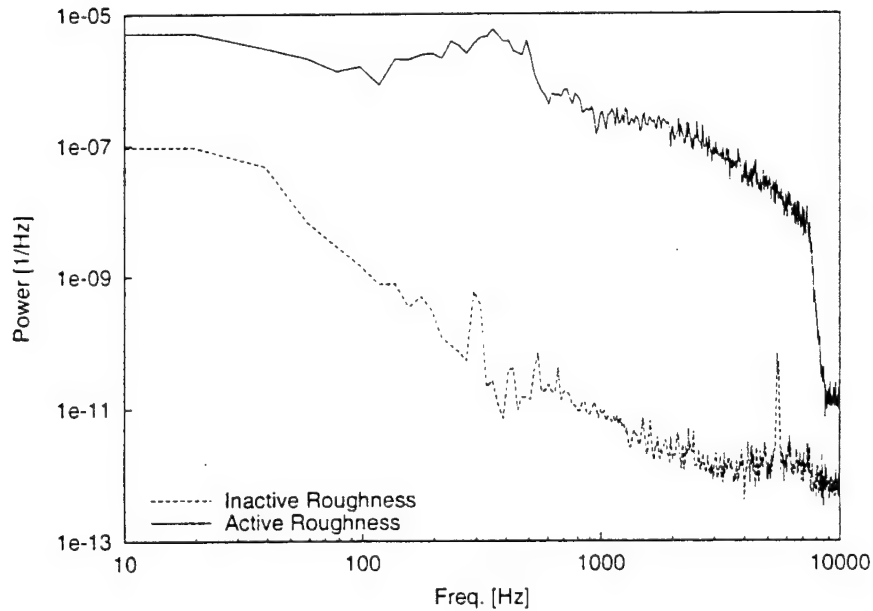
Figure 191: Fluctuating-velocity spectral density with and without activated 12-mm-spaced artificial roughness, $Re_c = 2.4 \times 10^6$, $x/c = 0.43$, $Y = 2.0$ mm, $z = 46$ mm.
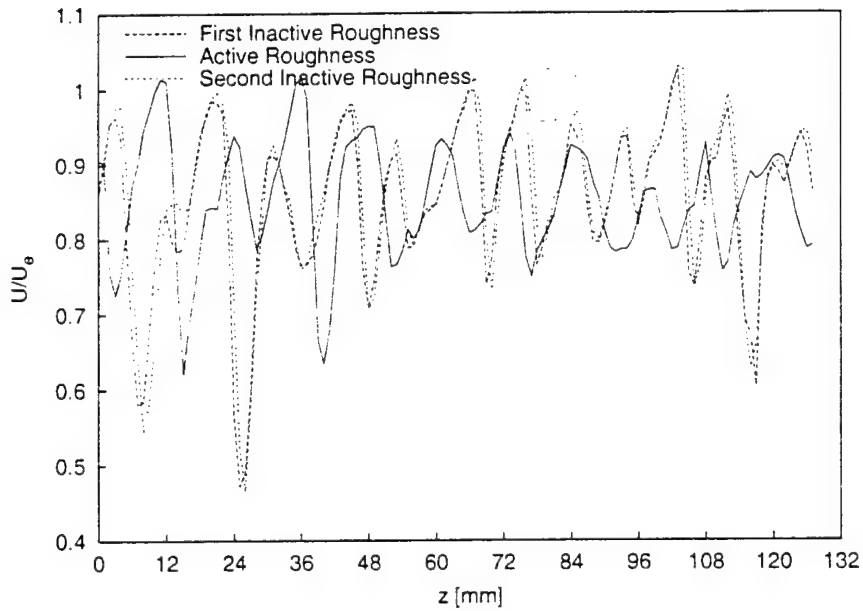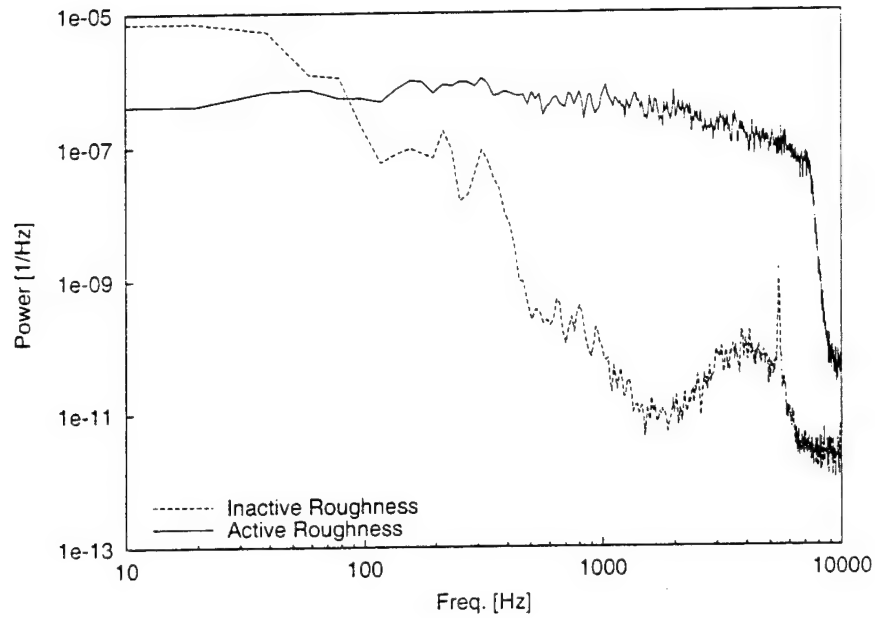
Figure 194: Spanwise mean-flow hotwire scan with and without activated 12-mm-spaced artificial roughness. $Re_c = 2.4 \times 10^6$, $x/c = 0.45$, $Y = 2.0$ mm.

Figure 195: Power spectral density of the spanwise mean-flow hotwire scan with and without activated 12-mm-spaced artificial roughness. $Re_c = 2.4 \times 10^6$, $x/c = 0.45$, $Y = 2.0$ mm.
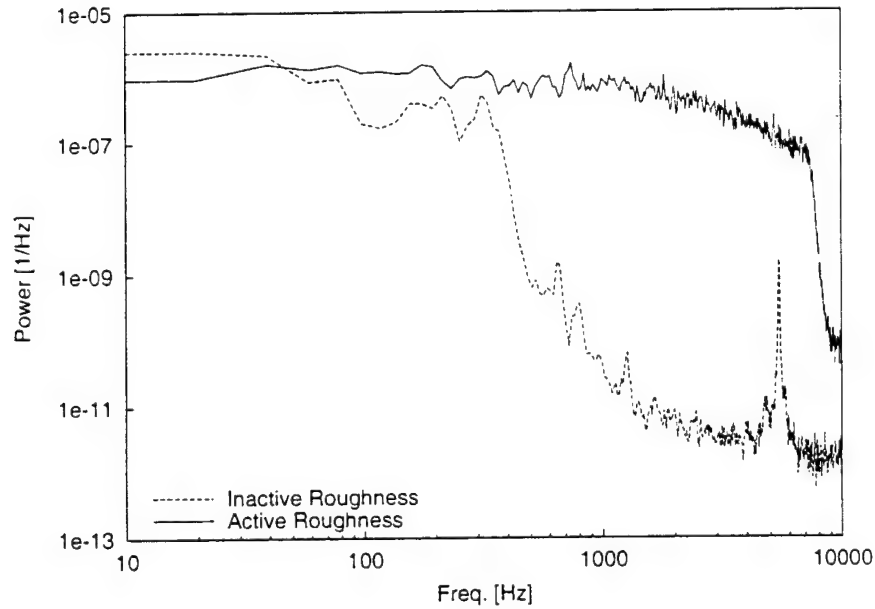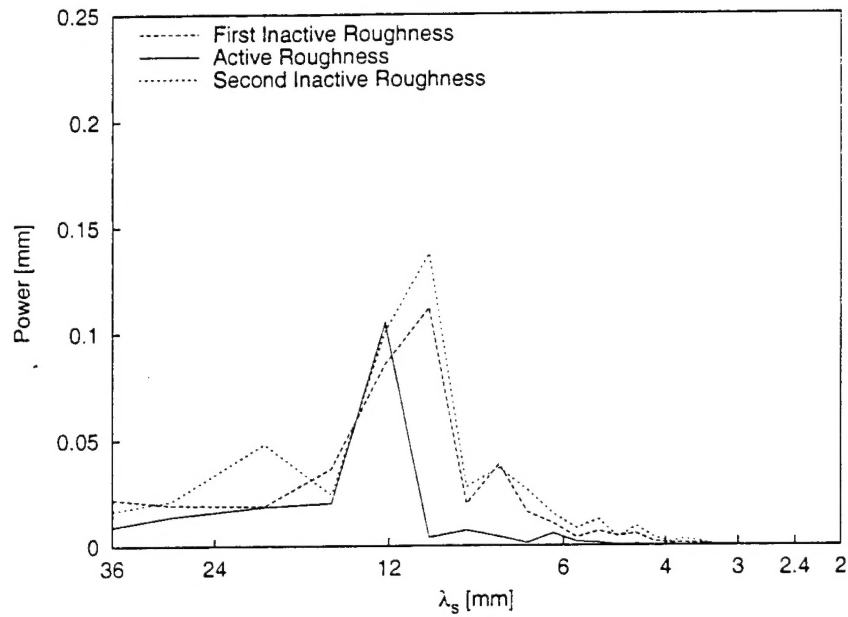
Figure 198: Fluctuating-velocity spectral density with and without activated 12-mm-spaced artificial roughness, $Re_c = 2.4 \times 10^6$, $x/c = 0.45$, $Y = 2.0$ mm, $z = 60$ mm.

Figure 199: Spanwise mean-flow hotwire scan with and without activated 12-mm-spaced artificial roughness. $Re_c = 2.8 \times 10^6$, $x/c = 0.38$, $Y = 1.2$ mm.
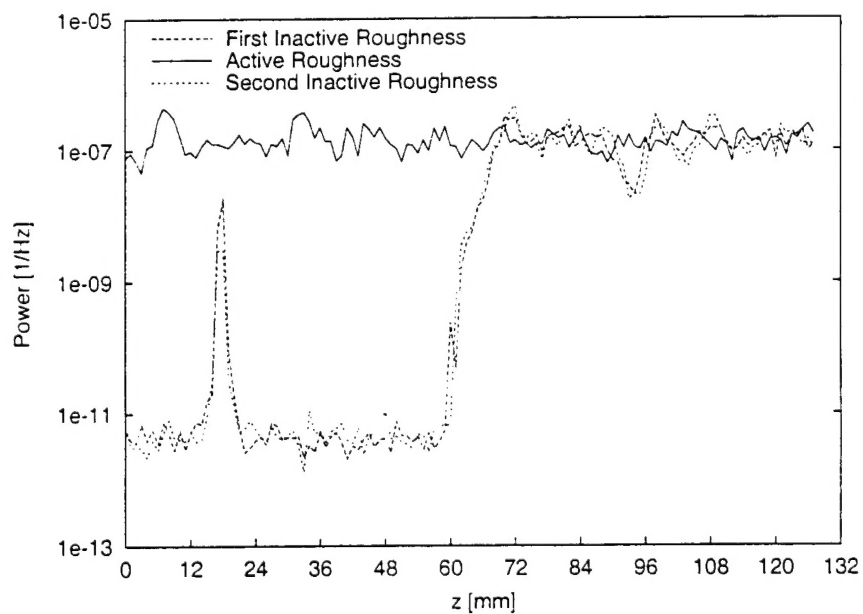
Figure 202: Fluctuating-velocity spectral density with and without activated 12-mm-spaced . artificial roughness. $Re_c = 2.8 \times 10^6$, $x/c = 0.38$, $Y = 1.2$ mm, $z = 23$ mm.

Figure 203: Fluctuating-velocity spectral density with and without activated 12-mm-spaced artificial roughness. $Re_c = 2.8 \times 10^6$, $x/c = 0.38$, $Y = 1.2$ mm, $z = 26$ mm.

Figure 206: Power spectral density of the spanwise mean-flow hotwire scan with and without activated 12-mm-spaced artificial roughness, $Re_c = 2.8 \times 10^6$, $x/c = 0.40$, $Y = 1.2$ mm.

Figure 207: Spanwise distribution of velocity-fluctuation power spectral density at 4.0 kHz with and without activated 12-mm-spaced artificial roughness, $Re_c = 2.8 \times 10^6$, $x/c = 0.40$, $Y = 1.2$ mm.
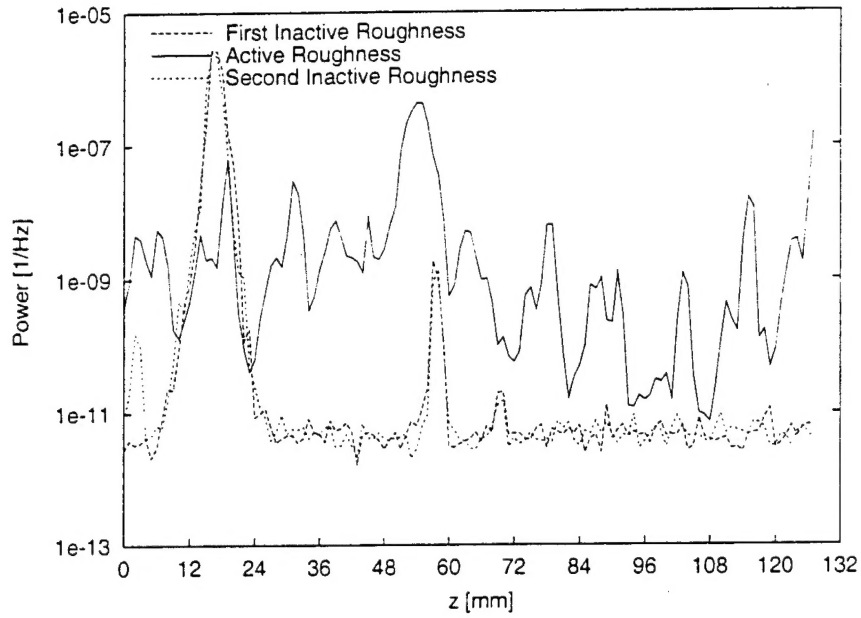
Figure 210: Spanwise distribution of velocity-fluctuation power spectral density at 2.0 kHz with and without activated 12-mm-spaced artificial roughness, $Re_c = 2.0 \times 10^6$, $x/c = 0.58$, $Y = 2.0$ mm.
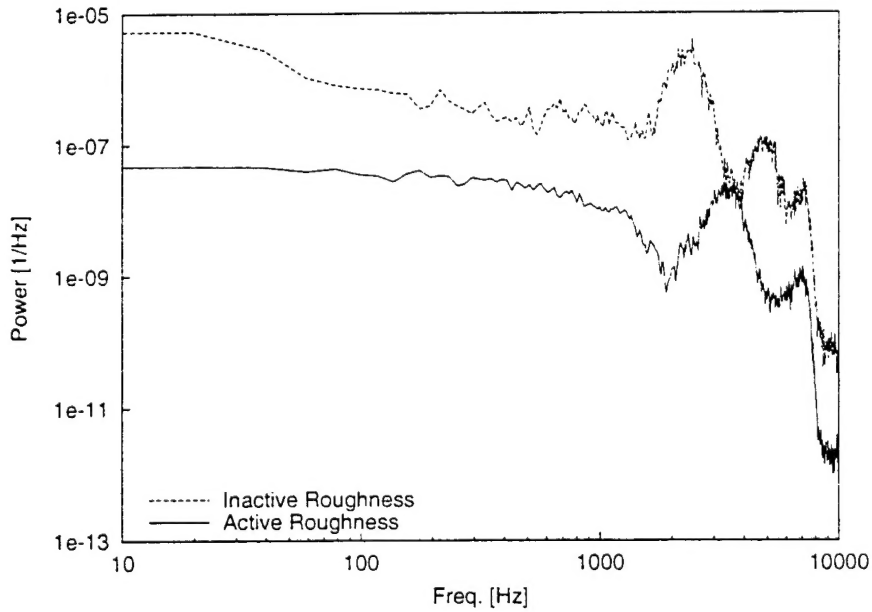

Figure 211: Fluctuating-velocity spectral density with and without activated 12-mm-spaced artificial roughness, $Re_c = 2.0 \times 10^6$, $x/c = 0.58$, $Y = 2.0$ mm, $z = 16$ mm.
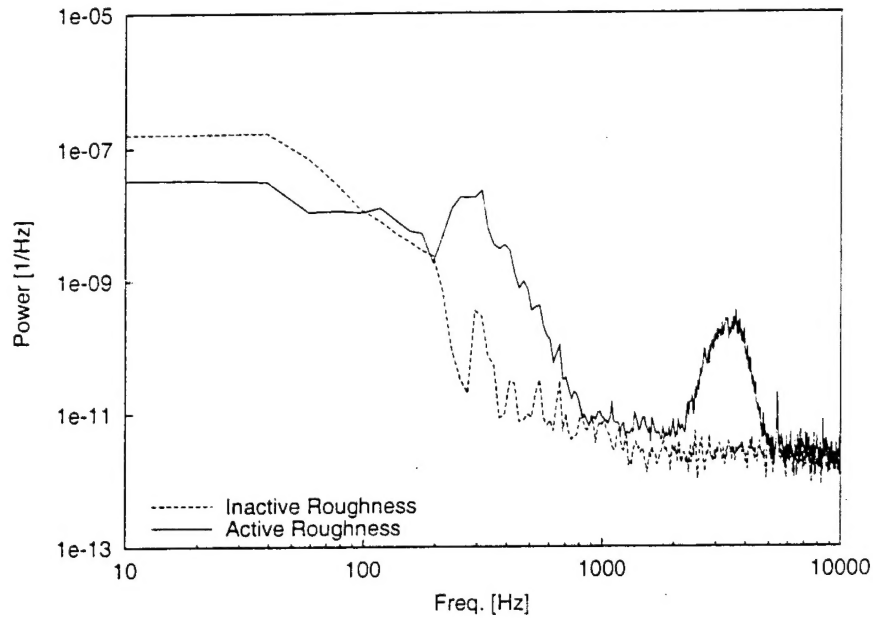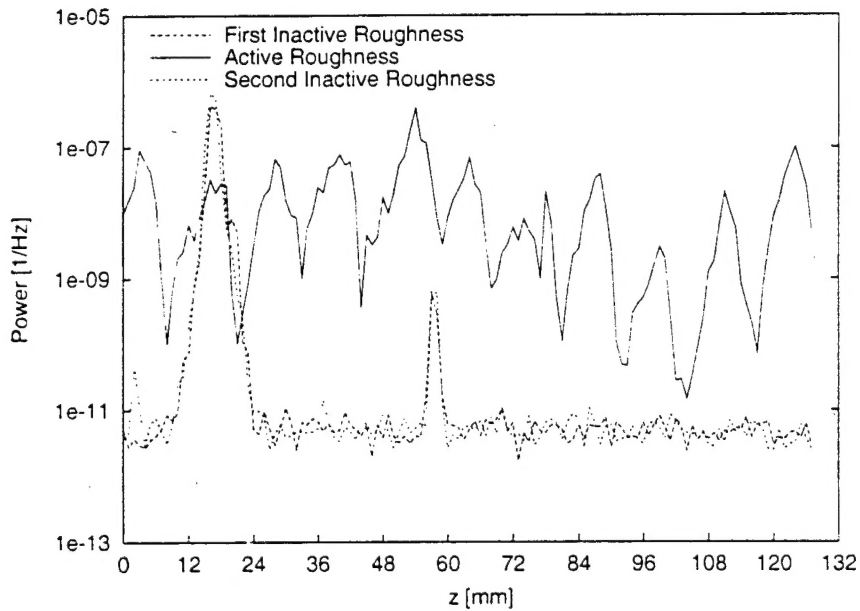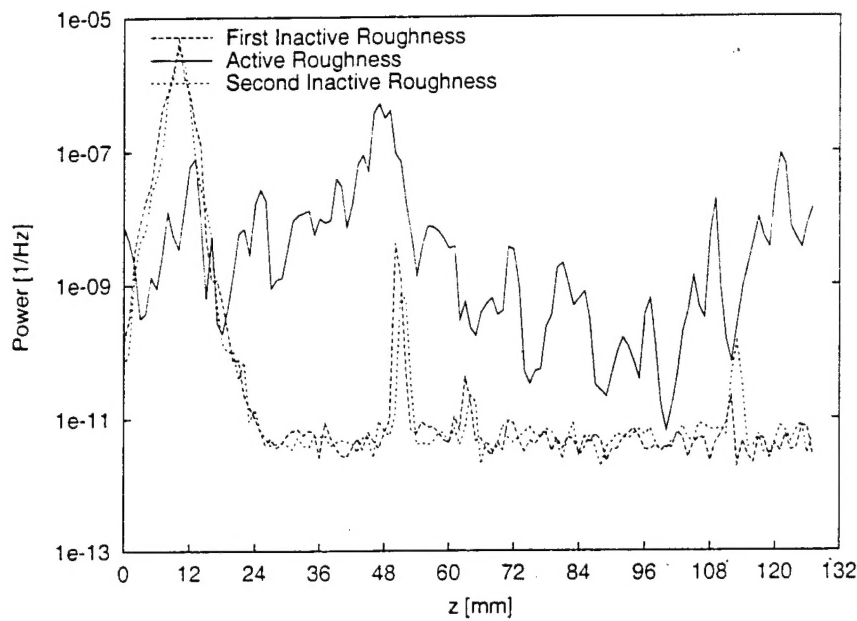
Figure 214: Fluctuating-velocity spectral density with and without activated 12-mm-spaced artificial roughness. $Re_c = 2.0 \times 10^6$, $x/c = 0.58$, $Y = 2.0\,\text{mm}$, $z = 107\,\text{mm}$.

Figure 215: Spanwise distribution of velocity-fluctuation power spectral density at $3.0\,\text{kHz}$ with and without activated 12-mm-spaced artificial roughness, $Re_c = 2.0 \times 10^6$, $x/c = 0.58$, $Y = 2.0\,\text{mm}$.

Figure 218: Spanwise distribution of velocity-fluctuation power spectral density at $2.0\,\text{kHz}$ with and without activated 12-mm-spaced artificial roughness, $Re_c = 2.0 \times 10^6$, $x/c = 0.60$, $Y = 2.0\,\text{mm}$.
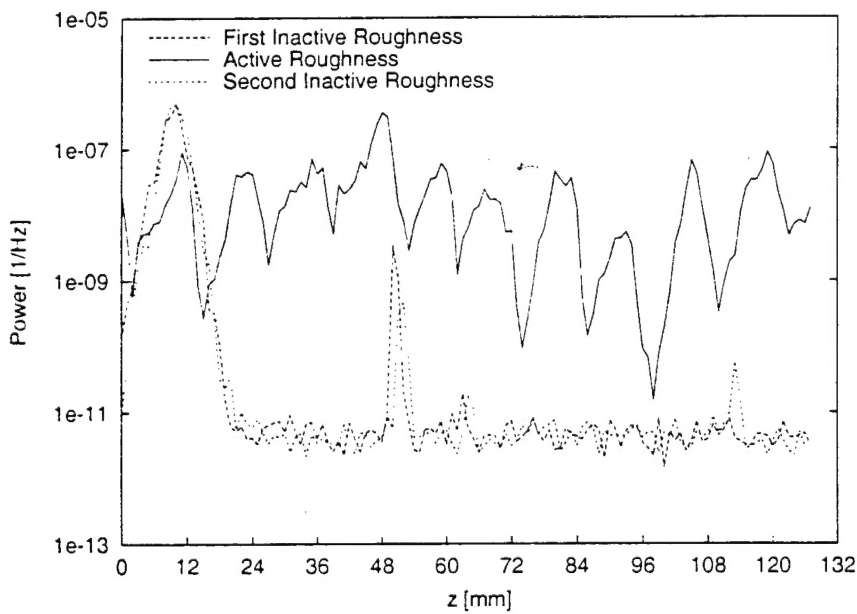

Figure 219: Spanwise distribution of velocity-fluctuation power spectral density at $3.0\,\text{kHz}$ with and without activated 12-mm-spaced artificial roughness, $Re_c = 2.0 \times 10^6$, $x/c = 0.60$, $Y = 2.0\,\text{mm}$.